Study of Muon-Induced Background in Direct Dark Matter and Other Rare Event Searches

Dissertation
der Mathematisch-Naturwissenschaftlichen Fakultät
der Eberhard Karls Universität Tübingen
zur Erlangung des Grades eines
Doktors der Naturwissenschaften
(Dr. rer. nat.)

vorgelegt von
Dipl.-Phys. Michael Bauer
aus Beirut

Tübingen
2012

Tag der mündlichen Qualifikation: 08.02.2013
Dekan: Prof. Dr. Wolfgang Rosenstiel
1. Berichterstatter: Prof. Dr. Josef Jochum
2. Berichterstatter: Prof. Dr. Heinz Clement

Contents

Abstract 6

Zusammenfassung 7

1. Dark Matter 8
- 1.1. Introduction 8
- 1.2. History of the Universe 8
- 1.3. Evidence for Dark Matter 9
  - 1.3.1. M/L Ratio of Galaxies and Galaxy Clusters 9
  - 1.3.2. Galaxy Rotation Curves 11
  - 1.3.3. Gravitational Lensing 11
  - 1.3.4. Cosmic Microwave Background 13
  - 1.3.5. Big Bang Nucleosynthesis (BBN) 16
  - 1.3.6. Bullet Cluster 18
  - 1.3.7. Structure Formation 20
  - 1.3.8. Supernovae Type Ia 21
- 1.4. Dark Matter Candidates 22
  - 1.4.1. Baryonic Dark Matter 22
  - 1.4.2. Neutrinos 23
  - 1.4.3. WIMPs 23
  - 1.4.4. Axions 24
  - 1.4.5. Other Candidates 25
  - 1.4.6. Alternative Explanations 25
- 1.5. Detection of Dark Matter 26
  - 1.5.1. Interactions of Dark Matter 26
  - 1.5.2. Indirect Detection of WIMP Annihilations 26
  - 1.5.3. Direct Detection of WIMP Elastic Scattering 26

2. Normal Matter 32
- 2.1. Cosmic Rays 32
- 2.2. Interactions of Muons 34
  - 2.2.1. Ionization 35
  - 2.2.2. Bremsstrahlung 35
  - 2.2.3. Pair Production 36
  - 2.2.4. Nuclear Interaction 36
- 2.3. Muons Underground 37

2.4. Neutron Background 38

3. Monte Carlo Simulations 40
3.1. Introduction 40
3.2. A Simulation Run—Step By Step 40
3.3. Geant4 Overview 42

4. Customizing Geant4 45
4.1. Physics Lists 45
  4.1.1. A Physics List for Dark Matter Searches 45
  4.1.2. Physics Content of the Models 46
    4.1.2.1. Quark-Gluon String Model 46
    4.1.2.2. Chiral Invariant Phase Space Model 47
    4.1.2.3. Precompound Model 47
    4.1.2.4. Bertini Cascade Model 48
    4.1.2.5. Binary Cascade Model 49
    4.1.2.6. Parameterized Cascade Model 49
    4.1.2.7. Photo-Nuclear Interaction 50
    4.1.2.8. Muon-Nuclear Interaction 51
    4.1.2.9. Low Energy Neutron Interactions 52
  4.1.3. Test of the Physics List 52
4.2. Generators 56
  4.2.1. Monoenergetic (Mean Muon Energy) Generator 56
  4.2.2. Gran Sasso Generator 56
  4.2.3. Frejus Generator 59
  4.2.4. Conversion of Simulation Results to Experimental Live Time . . . 61

5. Results 64
5.1. Generic Shielding Design Studies 64
  5.1.1. Overview of Shielding Designs 64
    5.1.1.1. Conventional Shielding Design 64
    5.1.1.2. Shielding Designs Avoiding the Use of High-Z Materials . 65
    5.1.1.3. Shielding Design Deliberately Using High-Z Materials . . 66
  5.1.2. Simulation Results 66
  5.1.3. Determination of Optimum Thicknesses of Materials 71
  5.1.4. “Toy Geometry” vs “Real Geometry” 80
  5.1.5. Gran Sasso Generator vs Frejus Generator 82
5.2. Shielding Design Studies for EURECA 83
  5.2.1. Overview 83
  5.2.2. Submarine 95
  5.2.3. Pool 97
  5.2.4. Standard Hall 97
  5.2.5. Comparison 99

6. Summary and Outlook 103

A. A Geant4 Physics List for Dark Matter Searches 104

Bibliography 108

Acknowledgements 120

Abstract

Most of the matter in the Universe is dark and is assumed to consist of up to now undetected massive particles which rarely interact with normal matter. The most likely candidates for these particles are the WIMPs (Weakly Interacting Massive Particles). To find these particles huge detectors with masses of about one tonne are needed, and still only a few Dark Matter induced events per year can be expected to be seen. The interactions of cosmic rays and local radioactivity are of course much more copious than that. A type of detector commonly used in Dark Matter search experiments is the cryogenic detector with simultaneous multichannel readout (e.g., scintillation and phonon signals) to discriminate nuclear recoils from other events. It can distinguish WIMPs from charged matter but not so easily from neutrons. Therefore it is important to shield the detectors from neutrons as well as possible and to know the number of neutrons still passing through the shielding as precisely as possible. These detectors are therefore placed deep underground and surrounded by specific shieldings. As the future Dark Matter search experiment EURECA (European Underground Rare Event Calorimeter Array) will be located in a newly built underground laboratory it is possible to integrate the shielding directly into the laboratory hall. The aim of the present work is to determine the optimum shielding strategy against muon-induced neutrons with respect to the selection and thickness of the shielding materials as well as the design of the laboratory. Monte Carlo simulations based on the GEANT4 toolkit are used for this purpose. It is found that a pool design in which the cryostat is directly submerged in water is favoured over a submarine design in which the entire hall is placed in water as the additional background from the steel walls of the "submarine" nullifies the shielding effects of the water. With a pool design the necessary low background of 1 count/(tonne · year) can be reached.

Zusammenfassung

Der größte Teil der Materie im Universum ist dunkel und besteht vermutlich aus bisher unbeobachteten massebehafteten Teilchen, die nur selten mit normaler Materie wechselwirken. Die wahrscheinlichsten Kandidaten hierfür sind die WIMPs (Weakly Interacting Massive Particles, schwach wechselwirkende massebehaftete Teilchen). Um diese Teilchen nachzuweisen, werden riesige Detektoren mit Massen von ungefähr einer Tonne benötigt, und trotzdem kann man nur ein paar wenige von Dunkler Materie hervorgerufene Ereignisse pro Jahr erwarten. Wechselwirkungen von kosmischer Strahlung und Umgebungsradioaktivität sind natürlich sehr viel häufiger. In Experimenten zur Suche nach Dunkler Materie werden oft kryogene Detektoren verwendet, die gleichzeitig mehrere Kanäle auslesen (z.B. Szintillation und Phononensignale), um Kernrückstöße von anderen Ereignissen zu diskriminieren. Diese Detektoren können WIMPs zwar von geladener Materie unterscheiden, jedoch nicht so leicht von Neutronen. Deshalb ist es wichtig, die Detektoren so gut wie möglich gegen Neutronen abzuschirmen und die Zahl der Neutronen, die doch noch durch die Abschirmung hindurchkommen, so genau wie möglich zu kennen. Sie werden tief unter der Erde aufgestellt und mit speziellen Abschirmungen umgeben. Da das zukünftige Experiment zur Suche nach Dunkler Materie EURECA (European Underground Rare Event Calorimeter Array, Europäische unterirdische Anordnung von Kalorimetern für seltene Ereignisse) in einem neu gebauten Untergrundlabor angesiedelt sein wird, ist es möglich, die Abschirmung direkt in die Laborhalle zu integrieren. Das Ziel dieser Arbeit ist es, die optimale Abschirmstrategie gegen myoninduzierte Neutronen im Hinblick auf die Auswahl und Dicke der Abschirmmaterialien und auf das Design des Labors zu bestimmen. Hierfür werden Monte Carlo Simulationen unter Verwendung des GEANT4-Toolkits durchgeführt. Es stellt sich heraus, dass ein Design mit einem Becken, in dem der Kryostat direkt in Wasser getaucht ist, vorteilhaft gegenüber einem U-Boot-Design ist, in dem die gesamte Halle im Wasser platziert ist, da der zusätzliche Untergrund von den Stahlwänden des “U-Boots” die Abschirmeffekte des Wassers wieder zunichte macht. Mit einem Beckendesign lässt sich der benötigte niedrige Untergrund von 1 Ereignis pro Tonne Detektormaterial und Jahr erreichen.

1. Dark Matter

1.1. Introduction

"What is the Universe made of?" One of the oldest questions of mankind, yet still the answer is not known. In the last two decades science has made truly remarkable progress in determining the numbers which describe the composition of the Universe. Today we know that the Universe has a flat geometry and consists of $4.56 \pm 0.16\,\%$ normal (baryonic) matter, $22.7 \pm 1.4\,\%$ Dark Matter and $72.8^{+1.5}_{-1.6}\,\%$ Dark Energy [Jar11]. However, it is still unknown what this Dark Matter and Dark Energy really is. There are lots of theoretical speculations and several plausible candidates, the properties of which can still span large parameter ranges, and now it is the experimentalists's job to actually detect this Dark Matter (and of course also the Dark Energy, but this is even a lot more speculative and outside the scope of this work). Since Dark Matter interacts only weakly with normal matter, this is not an easy task: huge detectors have to be operated for a long time in a deep underground location, well shielded against radioactivity and cosmic radiation. The shielding against cosmic muons will be the main topic of this work, but first let's have a closer look at Dark Matter.

1.2. History of the Universe

The Universe is thought to originate in the Big Bang, the singularity in which space and time came into existence. It was very hot and dense in the beginning and is cooling and expanding since then. The expansion is described by the Hubble law [Hub29]

$$v = H \cdot d$$

v is the velocity with which galaxies at distance d recess from us due to the expansion; H is called the Hubble constant. Its current best value is $H_0 = 70.4^{+1.3}_{-1.4}\,\mathrm{km/(s \cdot Mpc)}$ [Jar11]; it has also become customary to express its value by introducing the Hubble parameter $h = H_0/(100\,\mathrm{km/(s \cdot Mpc)})$.

The geometrical properties of the Universe are determined by the total energy density of its constituents, i. e. matter, radiation and cosmological constant (Dark Energy). Densities are commonly expressed as fractions $\Omega = \rho/\rho_c$ of the critical density [Pea01]

$$\rho_c = \frac{3H^2}{8\pi G}$$

with G the gravitational constant. If the total density is larger than the critical density, i. e. $\Omega_{\mathrm{tot}} = \Omega_{\mathrm{m}} + \Omega_{\mathrm{r}} + \Omega_{\Lambda} > 1$ (with Ω_{m} the matter density, Ω_{r} the radiation density and Ω_{Λ} the Dark Energy density), the Universe is closed due to its positive curvature $k = 1$. If $\Omega_{\mathrm{tot}} < 1$, $k = -1$ and the Universe is open. If the total density equals the critical density, $\Omega_{\mathrm{tot}} = 1$, $k = 0$ and the Universe is flat. If there is no Dark Energy ($\Omega_{\Lambda} = 0$), a closed Universe recollapses eventually, an open Universe expands forever and a flat Universe also expands forever but its expansion is slowing down. If there is Dark Energy, this situation gets more complicated, see Fig. 1.1 and [Pea01]. Current data indicate that we live in a Universe in which Dark Energy leads to an accelerated expansion (see also section 1.3.8).

The history of the Universe is governed by the following milestones [Ber99, Ber05, Bör03, Fri08, Jar11, Pov99]:

- $t \sim 10^{-35}\,\mathrm{s}$ / $T \sim 10^{16}\,\mathrm{GeV}$:[1] Breakdown of the Grand Unification of all forces. The quark-photon ratio is fixed to about 10^{-9}. Inflation begins: the Universe expands by a factor of 10^{29} in size during 10^{-32} seconds.
- $t \sim 10^{-11}\,\mathrm{s}$ / $T \sim 10^{2}\,\mathrm{GeV}$: Breakdown of the electroweak symmetry: electromagnetic and weak forces decouple
- $t \sim 10^{-6}\,\mathrm{s}$ / $T \sim 0.3\,\mathrm{GeV}$: Quarks and gluons are confined into hadrons (QCD phase transition)
- $t \sim 1\,\mathrm{s}$ / $T \sim 1\,\mathrm{MeV}$: Neutrons freeze out
- $t \sim 3\,\mathrm{min}$ / $T \sim 100\,\mathrm{keV}$: Primordial nucleosynthesis of protons and neutrons into light elements
- $t \sim 10000\,\mathrm{yr}$ / $T \sim 1\,\mathrm{eV}$: Matter energy density overtakes radiation energy density, structure formation begins
- $t \sim 380000\,\mathrm{yr}$ / $T \sim 0.4\,\mathrm{eV}$: Photons decouple from matter: origin of the cosmic microwave background radiation
- $t \sim 10\,\mathrm{Gyr}$: Dark Energy density overtakes matter energy density, leading to the accelerated expansion of the Universe
- $t = 13.75\,\mathrm{Gyr}$ / $T \sim 10^{-4}\,\mathrm{eV}$ ($T = 2.725\,\mathrm{K}$): today

1.3. Evidence for Dark Matter

1.3.1. M/L Ratio of Galaxies and Galaxy Clusters

The first evidence for the existence of Dark Matter has been discovered by Fritz Zwicky already in the 1930s by the observation of the velocity of galaxies in the Coma galaxy cluster [Zwi33, Zwi37].

---

[1] Temperatures of the early Universe are commonly expressed in units of energy by setting the Boltzmann constant $k_B = 1$.

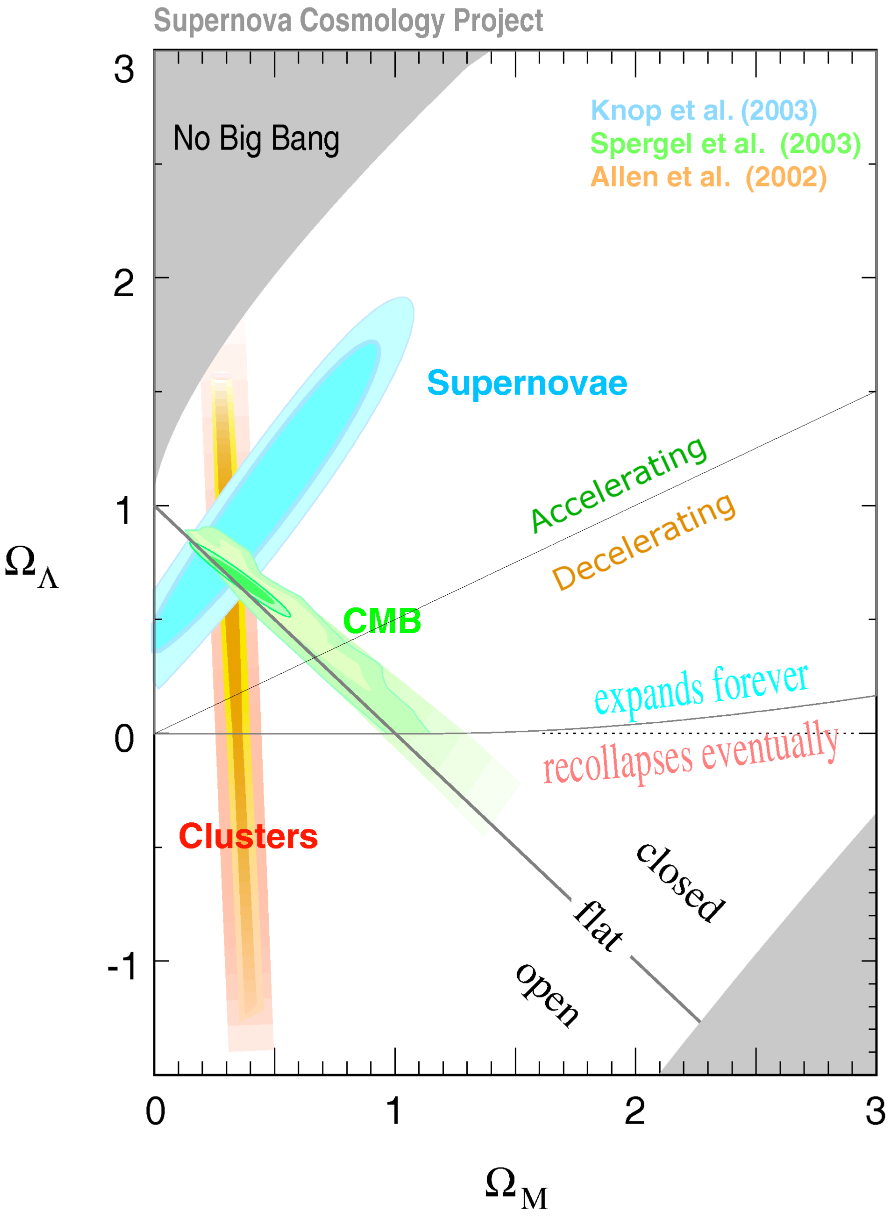

Figure 1.1.: Properties of the Universe: Depending on the values of the matter density Ω_M and the Dark Energy density Ω_Λ, its geometry can either be open, flat or closed; it can either recollapse eventually or expand forever; and if it expands forever, the expansion can slow down or speed up. All current measurements indicate that the Universe is flat, expands forever, and the expansion is even speeding up at the moment [Kno03].

By measuring the mass M and the luminosity L of a galaxy or a galaxy cluster, the ratio M/L can be calculated and compared to the ratio $M_\odot/L_\odot$ of the Sun. Typical values are on the order of $10\,M_\odot/L_\odot$ for galaxies and $100\,M_\odot/L_\odot$ for galaxy clusters [Bör03]. This means that there has to be a lot of invisible matter in galaxies and in galaxy clusters.

The mass of a galaxy cluster can be determined, e. g., by application of the virial theorem on the measured radial velocities of the galaxies in the cluster [Zwi37], by gravitational lensing [For94] or by observing the X-ray emission of the hot gas in the clusters [Sch95]. The high temperature of this gas ($10^7 - 10^8\,\mathrm{K}$) is also a hint to the existence of Dark Matter as the velocity of the gas is higher than the escape velocity deduced from the visually observed matter alone; but the gas is gravitationally bound, pointing to the existence of additional, Dark Matter, which constitutes at least 80% of the mass of the galaxy cluster [Lew03, Per03].

1.3.2. Galaxy Rotation Curves

Observation of the rotation curves of stars in spiral galaxies provides one of the best pieces of evidence for the existence of Dark Matter [Rub80]. The visible part of spiral galaxies consists of a central spherical bulge and a thin disk. The tangential velocity $v(r)$ of a star with mass m revolving in a galaxy with mass $M(r)$ at a distance r from the galactic centre can be determined by equating the gravitational and centrifugal forces [Per03]

$$\frac{mv^2(r)}{r} = \frac{GmM(r)}{r^2}$$

to be

$$v(r) = \sqrt{\frac{GM(r)}{r}}$$

As $M(r) \equiv 4\pi \int \rho(r) r^2 \mathrm{d}r$, with $\rho(r)$ the mass density profile of the galaxy, $M(r) \propto r^3$ inside the visible bulge of the galaxy and $M(r) = \text{const.}$ outside. Therefore, the velocity $v(r)$ should increase proportional to r inside the visible bulge and decrease proportional to $1/\sqrt{r}$ outside. However, determination of $v(r)$, e. g. by observation of the redshift of the 21 cm hydrogen line, shows that the velocity remains constant up to large radii, implying that $M(r) \propto r$. This can be explained if the visible part of the galaxy is embedded in a large halo consisting of Dark Matter which contains 80–90 % of the total mass of the galaxy [Per03]. An example of a rotation curve is shown in Fig. 1.2.

1.3.3. Gravitational Lensing

If a photon passes by an object with mass M at a minimum distance b, its flight path will be deflected by an angle [Chw24, Ein36, Per03]

$$\alpha = \frac{4GM}{bc^2}$$

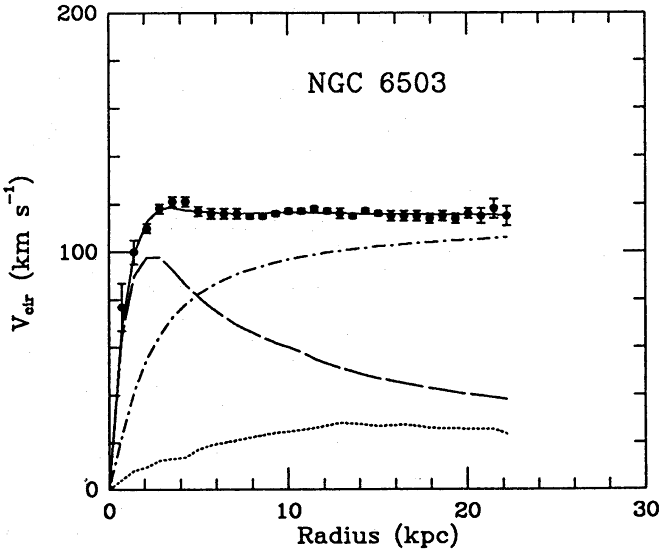

Figure 1.2.: Galaxy rotation curve of NGC 6503. The solid line is a fit to the data using a Dark Matter halo model. The other curves show the contribution of the visible components (dashed), the gas (dotted) and the Dark Matter halo (dash-dotted) [Beg91].

(G: gravitational constant, c: speed of light). The object acts as a gravitational lens, its mass can be determined from the above formula by measuring the angle of deflection. If the object is massive enough, e. g. a galaxy, a galaxy cluster or a black hole, multiple images of the source of the photon will appear, or in the ideal case (in which the source, the gravitational lens and the observer are collinear) an Einstein ring. This is called *strong* gravitational lensing. An example is shown in Fig. 1.3. If the lens is a star in our galaxy, the deflection is too small to be observed directly, but if the star moves past the line of sight, a transient change in the luminosity of the source can be observed; in contrast to a variable star the amplification of the light is independent of its wavelength. This is called *microlensing*. If light from distant sources passes by many lenses on its way to Earth, the distortion of the images can be studied statistically to obtain information on the large scale structure of the Universe: *weak* gravitational lensing [Wei08].

Gravitational lensing on cosmological scales has first been observed with quasars as sources [Wal79]. In the meantime, microlensing has been used to detect baryonic Dark Matter in the form of non-luminous astrophysical objects called MACHOs (Massive Astrophysical Compact Halo Objects). MACHOs can be brown dwarfs, neutron stars and possibly white dwarfs, faint red dwarfs or black holes. Their masses are between $0.001 - 1\,M_{\odot}$. From observations they could contribute anything from (almost) zero up to 20% of the Dark Matter in the galaxy [Alc00, Tis07]. Hubble Space Telescope data however give an upper limit of less than 1% of the mass of the galactic halo [Gra96], therefore MACHOs cannot be a significant contribution to Dark Matter.

Figure 1.3.: Gravitational lensing in Abell 2218 as seen by the Hubble Space Telescope [HST95]. The arcs are parts of an Einstein ring.

1.3.4. Cosmic Microwave Background

Cosmic microwave background radiation (commonly abbreviated as CMB or CMBR) has been discovered in 1964 by Penzias and Wilson when trying to understand unexpected noise in a radio antenna [Pen65]. It has an almost perfect black body spectrum with a temperature of 2.725 K today (see Fig. 1.4). It is a direct sign of a hot and dense past of our Universe: When electrons and protons combine into neutral hydrogen atoms 380000 years after the Big Bang, photons can no longer easily interact with baryons and travel freely. At this time their temperature is about 3000 K; with the expansion of the Universe they cool to their present value.

When looking into the sky in two different directions, the temperature of the CMB is almost the same, but not exactly. The deviation of the temperature in direction $\mathbf{n}$ from its mean value can be expanded in terms of spherical harmonics [Wei08]:

$$\frac{\Delta T(\mathbf{n})}{T} = \sum_{l=0}^{\infty} \sum_{m=-l}^{+l} a_{lm} Y_{lm}(\mathbf{n})$$

The correlation is measured between two directions $\mathbf{n}$ and $\mathbf{m}$ separated by an angle θ (with $\mathbf{n} \cdot \mathbf{m} = \cos\theta$). Averaging over all directions separated by this angle gives the correlation function $C(\theta)$ which is commonly expanded in Legendre polynomials $P_l(\cos\theta)$ [Per03]:

$$C(\theta) = \left\langle \left(\frac{\Delta T(\mathbf{n})}{T} \right) \left(\frac{\Delta T(\mathbf{m})}{T} \right) \right\rangle = \frac{1}{4\pi} \sum (2l+1) C_l P_l(\cos\theta)$$

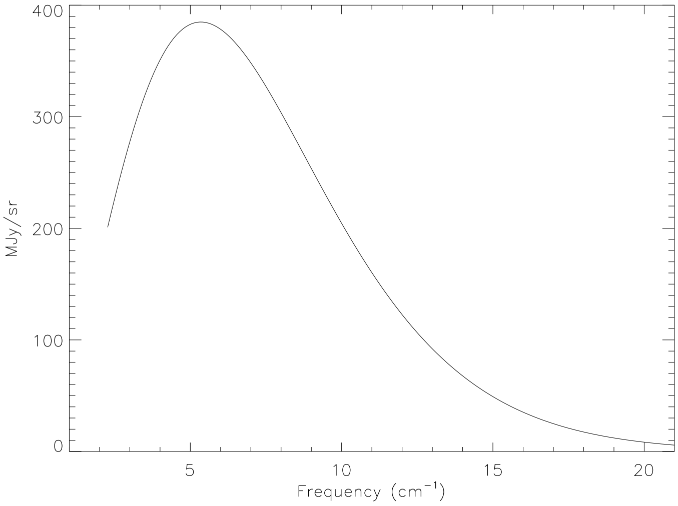

Figure 1.4.: The cosmic background radiation (as measured by COBE, the predecessor of WMAP) follows a perfect Planck spectrum; the error bars are much smaller than the line width [Fix96].

The measured spectrum is then plotted as a function of the multipole moment l (see Fig. 1.5). It can be used to determine many important properties of the Universe. The largest deviation from the black body temperature on the order of 10^{-3} K originates from the motion of the Earth relative to the rest frame of the CMB. This *dipole term* can be used for calibration of the spectrum [Hin09]. More interesting are the tiny primordial fluctuations on the order of 10^{-5} K (see Fig. 1.6). They originate from the following effects [Pea01, Per03, Wei08]:

- Intrinsic fluctuations in the temperature of the plasma at the time of last scattering. This effect is mostly important at small scales.
- Fluctuations in the velocity of the plasma at the time of last scattering, leading to a Doppler shift of the photons scattering off the plasma. At medium scales, this is the dominant effect.
- Fluctuations in the gravitational potentials at the time of last scattering, leading to the Sachs-Wolfe effect. On the one hand, denser regions are hotter; on the other hand, photons are redshifted, and therefore appear cooler, when they leave the gravitational potential. As the effect of the redshift dominates, denser regions appear cooler, less dense regions hotter. This effect and the following dominate the spectrum at large scales.
- Fluctuations in the gravitational potentials between the time of last scattering and

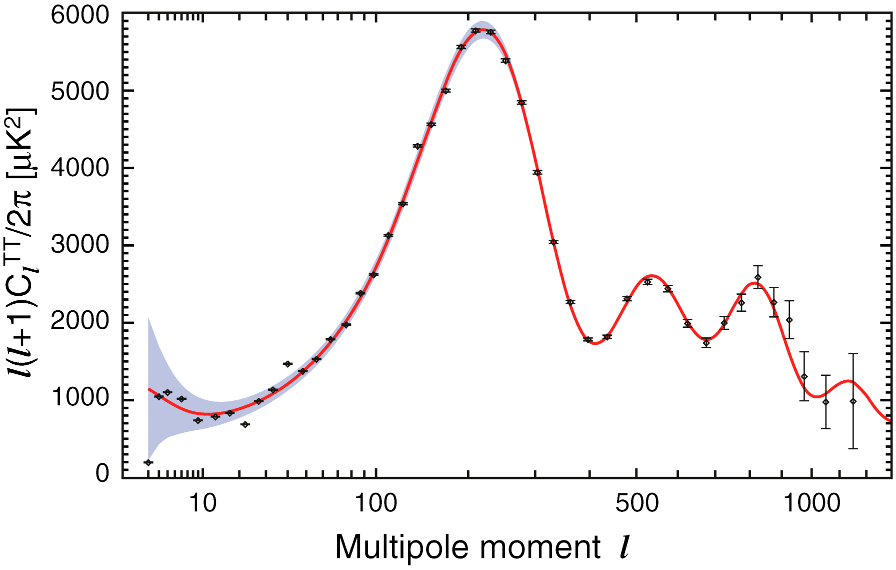

Figure 1.5.: Power spectrum of CMB fluctuations as measured by WMAP [Lar11]

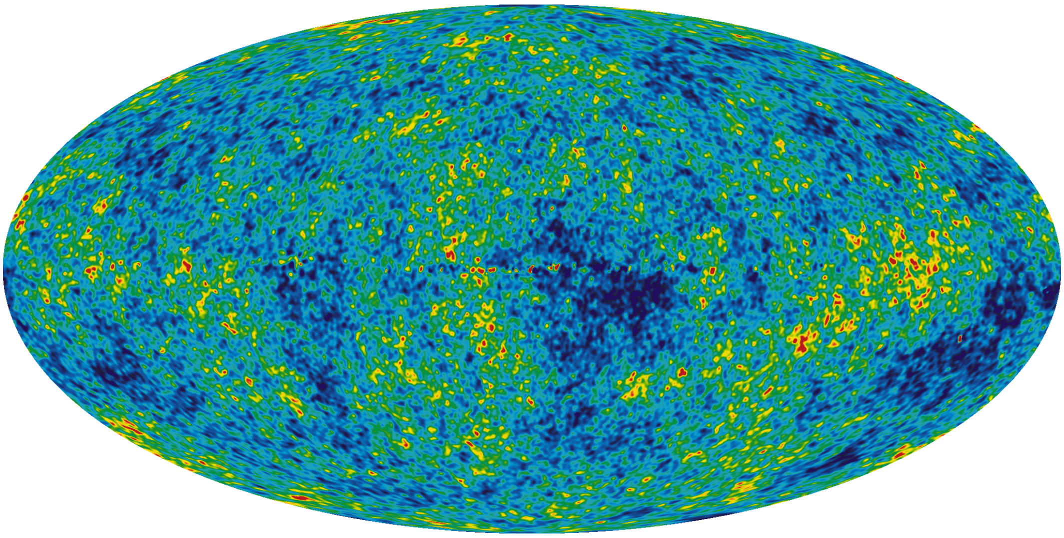

Figure 1.6.: Sky map of cosmic microwave background fluctuations as seen by WMAP [LAM08]. Bright yellow regions appear hotter, dark blue regions appear cooler at decoupling.

today, leading to the so-called *integrated* Sachs-Wolfe effect (ISW). This effect can be subdivided into the *early* ISW, which happens at the time the Universe changes from radiation to matter domination, and the *late* ISW, which happens when the cosmological constant Λ begins to dominate the energy density of the Universe.

The dominant structures are produced by acoustic oscillations: an already denser region of the baryon-photon fluid attracts additional baryons, thereby increasing the compression. This is counteracted by the radiation pressure of the photons, leading to standing acoustic waves. The wave extends as far as sound can travel, so their actual size is given by the sound horizon at the time of last scattering. The apparent size on the sky depends on the curvature of the Universe: If the Universe is closed, the region appears larger than it actually is; if the Universe is open, the region appears smaller (see Fig. 1.7). This is also visible in the position of the first peak of the power spectrum (see Fig. 1.5): if the Universe is closed, the peak is at a larger angle or smaller l, respectively; in an open Universe it is the other way around. The larger the baryonic contribution, the stronger the compression peaks in the spectrum; the value of Ω_b can be deduced from the relative peak heights. The Doppler shift brings the oscillations in the power spectrum out of phase with the temperature oscillations, thereby reducing the heights of the acoustic peaks. The higher multipoles can be used to determine many other cosmological parameters.

Some of the newest results obtained by the WMAP satellite after 7 years of observation are [Jar11]:

- Baryon density $\Omega_\mathrm{b} = 0.0456 \pm 0.0016$
- Dark Matter density $\Omega_\mathrm{dm} = 0.227 \pm 0.014$
- Dark Energy density $\Omega_\Lambda = 0.728^{+0.015}_{-0.016}$
- Hubble constant $H_0 = 70.4^{+1.3}_{-1.4}\,\mathrm{km\,s^{-1}\,Mpc^{-1}}$

The baryon density Ω_b is much smaller than the Dark Matter density Ω_dm. This means that most of the Dark Matter has to be nonbaryonic.

Another hint to the existence of nonbaryonic Dark Matter is the *smallness* of the temperature fluctuations [Per03]: Baryonic matter can start to clump only after it has decoupled from photons. If the currently visible structures should have formed during the amount of time available since then, the fluctuations at that time would have to be 2–3 orders of magnitude larger than they actually were. As nonbaryonic Dark Matter does not easily interact with photons, it can begin to form structures earlier, so they have more time to form.

1.3.5. Big Bang Nucleosynthesis (BBN)

In the beginning, the Universe is too hot for elements to form. Neutrons and protons are kept in thermal equilibrium by the weak interaction [Bör03, Kla97, Per03]:

$$\mathrm{n} + \nu_e \leftrightarrow \mathrm{p} + e^- \qquad \mathrm{n} + e^+ \leftrightarrow \mathrm{p} + \bar{\nu}_e$$

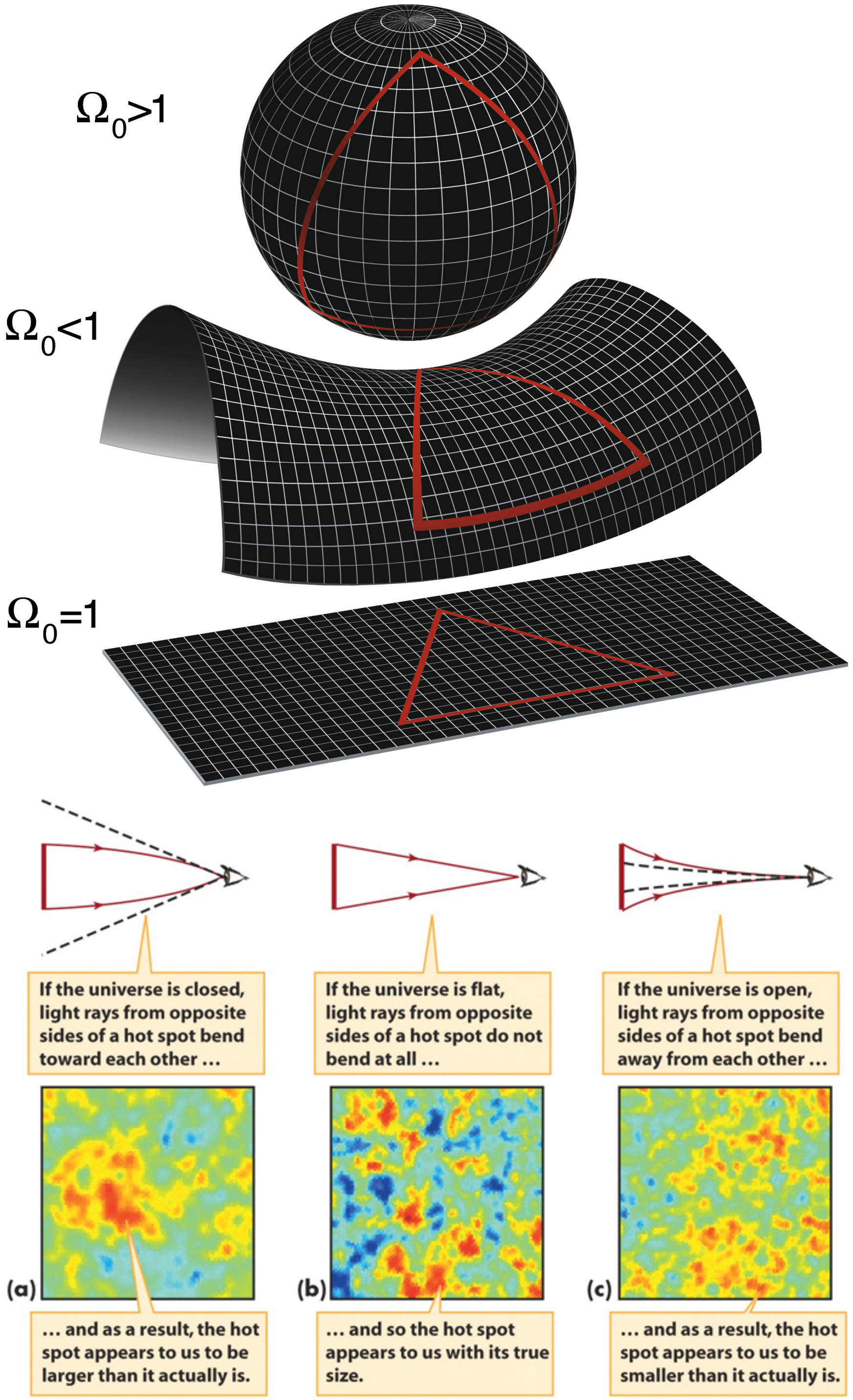

If the universe is closed, light rays from opposite sides of a hot spot bend toward each other …

If the universe is flat, light rays from opposite sides of a hot spot do not bend at all …

If the universe is open, light rays from opposite sides of a hot spot bend away from each other …

… and as a result, the hot spot appears to us to be larger than it actually is.

… and so the hot spot appears to us with its true size.

… and as a result, the hot spot appears to us to be smaller than it actually is.

Figure 1.7.: Curvature of the Universe and its influence on the apparent size of regions in the sky [WMAP10, Smo09]

Their ratio is given by the Boltzmann factor

$$\frac{N_{\mathrm{n}}}{N_{\mathrm{p}}} = \exp\left(\frac{-(m_{\mathrm{n}} - m_{\mathrm{p}})c}{kT}\right)$$

At about 0.8 MeV the above equilibrium reactions freeze out; the neutron fraction is $\frac{N_{\mathrm{n}}}{N_{\mathrm{p}}} \approx \frac{1}{5}$. Deuterons are produced via

$$\mathrm{n} + \mathrm{p} \leftrightarrow \mathrm{d} + \gamma$$

At about 0.05 MeV photodisintegration of deuterons freezes out and helium production begins, e. g.

$$\mathrm{d} + \mathrm{d} \rightarrow \mathrm{t} + \mathrm{p} \qquad \mathrm{t} + \mathrm{d} \rightarrow^{4} \mathrm{He} + \mathrm{n}$$

At this time the neutron fraction has fallen to $\sim \frac{1}{7}$ by decay

$$\mathrm{n} \rightarrow \mathrm{p} + e^{-} + \bar{\nu}_{e}$$

The mass fraction of ^{4}He is given by

$$Y = \frac{4N_{\mathrm{He}}}{4N_{\mathrm{He}} + N_{\mathrm{p}}} = 0.24$$

It is a big success of the BBN model that this prediction coincides with measurements.

As there are no stable nuclei with $A = 5$ or 8, further nucleosynthesis is limited and mostly takes place in stars and supernovae; the only other stable element produced primordially in small quantities is ^{7}Li, e. g.

$$^{4}\mathrm{He} + \mathrm{t} \rightarrow^{7} \mathrm{Li} + \gamma$$

The abundances of the light elements depend on the density of baryons in the Universe (see Fig. 1.8). By measuring these abundances, the baryon density Ω_{b} can therefore be determined. A commonly used value is $0.018 < \Omega_{\mathrm{b}}h^{2} < 0.023$ [Ber05, Oli03]. This value is in reasonable agreement with the baryon density obtained by WMAP but differs substantially from the total matter density $\Omega_{\mathrm{m}}h^{2} = 0.1334^{+0.0056}_{-0.0055}$ [Jar11]. This is an independent indication of the existence of non-baryonic Dark Matter.

1.3.6. Bullet Cluster

The up to now most convincing empirical evidence for the existence of Dark Matter has been found by observation of 1E 0657-558 (z=0.296), also known as the “bullet cluster”, a merger of two galaxy clusters which collided about 100 Myr ago (see Fig. 1.9) [Clo06]. A similar observation on the MACS J0025.4-1222 cluster (z=0.586) has now confirmed these findings [Bra08].

As the chance of two galaxies actually hitting each other in such a merger is negligible,

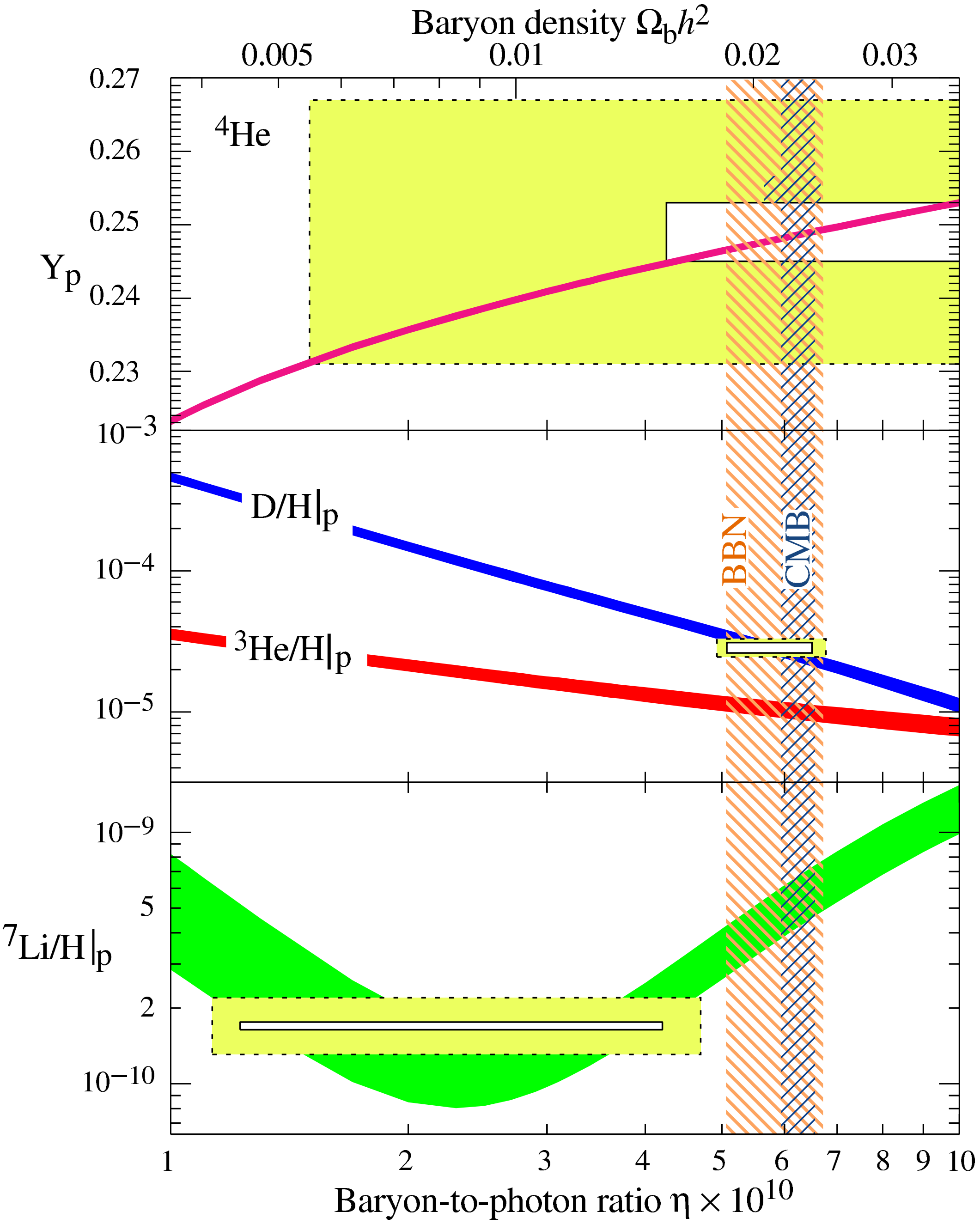

Figure 1.8.: Dependence of light element abundances on baryon density. The bands are the predictions of the Big Bang Nucleosynthesis at 95% C.L., the boxes are measurements (small boxes: including $\pm 2\sigma$ statistical errors; large boxes: including $\pm 2\sigma$ statistical and systematical errors). The shaded vertical bands are the baryon density obtained from cosmic microwave background measurements and the BBN concordance range (both at 95% C.L.) [PDG10]

Figure 1.9.: The *bullet cluster* is a recent merger of two galaxy clusters, in which the galaxies (white and orange) and the intergalactic gas (pink) are still separated. The mass distribution (blue) as obtained by gravitational lensing follows the galaxies, although the gas is more massive. This is currently the best evidence for the existence of Dark Matter [CHA06].

they behave like collisionless particles, while the hot X-ray-emitting inter-galaxy gas acts as a fluid which experiences pressure and is therefore slowed down during the collision. In most theoretical models Dark Matter is also expected to be collisionless. Since it takes some time until the galaxies and the gas are virialized again, their distributions are still spatially separated in the Bullet cluster. The distribution of the gravitational potential has been measured by weak gravitational lensing. Without Dark Matter one would expect that the gravitational potential follows the inter-galaxy gas, which accounts for about five times the mass of the stars in the galaxies [All02, Whi93]. However, it has been found that the gravitational potential follows the distribution of the galaxies, which is a strong indication of collisionless Dark Matter and refutes most alternative gravitational theories such as MOND (see section 1.4.6).

1.3.7. Structure Formation

Although the Universe is homogeneous and isotropic at the largest scales, there exists ample structure at smaller scales: stars, galaxies, galaxy clusters, superclusters, filaments and voids. In principle, there are two ways such a hierarchy of structures could have formed: starting with the largest structures which later subdivide into smaller ones (top-down), or by assembling larger structures from initially smaller building blocks (bottom-up). Which way is it in nature?

Classically, a cloud of gas starts to collapse if the gravitational energy dominates over the kinetic energy of the gas, which is the case if the size of the cloud exceeds a critical size called Jeans length [Per03]

$$\lambda_{\mathrm{J}} = v_{\mathrm{s}} \left(\frac{\pi}{G\rho} \right)^{1/2}$$

(with v_{s} being the velocity of sound in the cloud and ρ its density) and therefore its mass exceeds a critical mass, the Jeans mass

$$M_{\mathrm{J}} = \frac{\pi \rho \lambda_{\mathrm{J}}^3}{6}$$

In an expanding Universe the expansion of course has to be taken into account but does not change these results in a fundamental way [Wei08]. Important is however the influence of the Dark Matter. A relativistic particle can travel freely from denser to less dense regions, thereby smearing out these fluctuations. The distance it travels until it becomes nonrelativistic is called free-streaming length λ_{fs} [Pea01]. As all structures smaller than λ_{fs} are smeared out, structures can only form if their sizes are larger than the free-streaming length of the dominant Dark Matter particles. Dark Matter particles can be classified as either Hot Dark Matter (HDM) or Cold Dark Matter (CDM) [Bör03]. Hot Dark Matter is Dark Matter which decouples from normal matter when it is still relativistic; it is light and has a large free-streaming length. Cold Dark Matter decouples when it is already non-relativistic; it is heavy and has a much smaller free-streaming length. In a Hot Dark Matter scenario therefore only top-down structure formation is possible. As there is observational evidence for smaller structures at the relevant times this indicates that structure formation happens bottom-up and the dominant Dark Matter is cold.

1.3.8. Supernovae Type Ia

According to the Hubble law the expansion rate of the Universe is supposed to be linear with distance [Hub29]:

$$v = H \cdot d$$

v is the velocity at which an astronomical object at distance d moves away from us due to the expansion, and H is the Hubble constant. The velocity of the object can be determined by the redshift of its spectral lines, but its distance is in general more difficult to obtain, especially at larger distances. Good candidates for the verification of this law are therefore the *standard candles*: objects of which the absolute luminosity is fixed or can be easily determined. Therefore their distance can be calculated from their apparent luminosity. One especially useful class of standard candles are supernovae of type Ia: because of their high brightness they can be seen even at very large distances. Recent observations have shown that these objects are dimmer—and therefore farther away—than expected (see Fig. 1.10) [Per99, Rie98]. This indicates an accelerated expansion

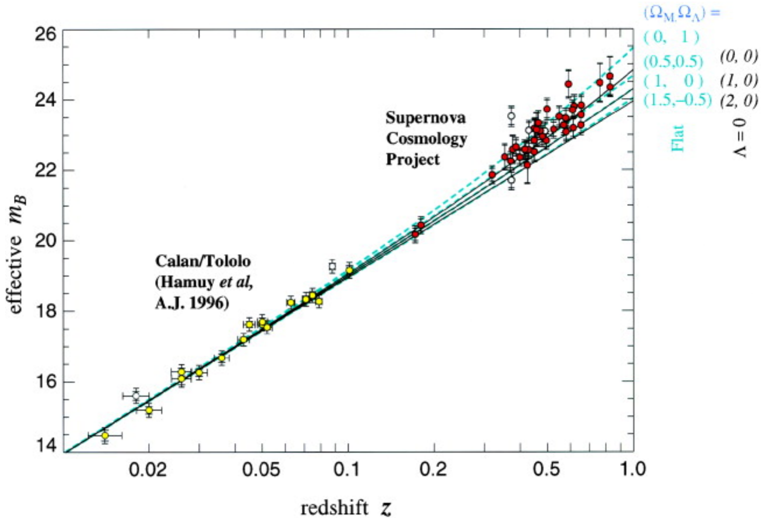

Figure 1.10.: The Hubble plot shows the apparent magnitude m_B of supernovae of type Ia (as a measure of distance) as a function of redshift z (as a measure of recessional velocity). At high z values the distances of the supernovae are larger than expected in a Universe without a cosmological constant ($\Lambda = 0$). This is an indication of the existence of Dark Energy and an accelerated expansion of the Universe [Per99].

of the Universe. The origin of this acceleration is labeled Dark Energy. According to CMB measurements by WMAP it constitutes $72.8^{+1.5}_{-1.6}$ % of the total energy density of the Universe [Jar11]. It acts like a negative pressure driving the Universe apart, but its exact nature is at present not yet known and beyond the scope of this work.

1.4. Dark Matter Candidates

1.4.1. Baryonic Dark Matter

The density of baryons in the Universe determined from the cosmic microwave background (see section 1.3.4) and Big Bang nucleosynthesis (see section 1.3.5) is about 4.5 % of the critical density. As this is larger than the visible baryon density of about 0.3 % [Per92], some of the Dark Matter must be baryonic. Possible candidates are MACHOs as observed by gravitational lensing (see section 1.3.3). However, the total density of the Dark Matter is 22.7% of the critical density [Jar11], which is again much larger than the total density of baryons. Therefore most of the Dark Matter has to be non-baryonic. This will be the subject of the following sections.

Family	1	2	3
Quarks	$\begin{pmatrix} u \\ d \end{pmatrix}$	$\begin{pmatrix} c \\ s \end{pmatrix}$	$\begin{pmatrix} t \\ b \end{pmatrix}$
Leptons	$\begin{pmatrix} \nu_e \\ e^- \end{pmatrix}$	$\begin{pmatrix} \nu_\mu \\ \mu^- \end{pmatrix}$	$\begin{pmatrix} \nu_\tau \\ \tau^- \end{pmatrix}$
Gauge bosons	B^0, W^0, $W^\pm$, 8 g		
Higgs	H^0		

Table 1.1.: Standard Model particles. The physical γ and Z^0 particles are orthogonal linear combinations of the fundamental B^0 and W^0 bosons.

1.4.2. Neutrinos

Neutrinos have one big advantage compared to other nonbaryonic Dark Matter candidates: as clearly observed Standard Model particles they are already known to exist. Similar to the cosmic microwave background there is a cosmic neutrino background providing 339 neutrinos and antineutrinos per cm^3 [Per03]. Unfortunately neutrinos also have one big disadvantage: their masses are very small, making neutrinos Hot Dark Matter, a large amount of which is excluded by structure formation (see section 1.3.7). Direct mass measurements limit their masses to 2 eV [Kra03, Lob02, PDG10], and further experiments with a sensitivity to neutrino masses on the order of 0.2 eV are ongoing [Abt04, Ang05]. The current neutrino mass limit corresponds to an energy density of $\Omega_\nu h^2 \lesssim 0.07$ [Ber05], to be compared with a total Dark Matter density of $\Omega_{\mathrm{dm}} h^2 = 0.1123 \pm 0.0035$ [Jar11]. Observations of cosmic microwave radiation, baryon acoustic oscillations and supernovae limit the neutrino density even to $\Omega_\nu h^2 < 0.0062$ [Jar11]. Clearly, other Dark Matter candidates are necessary. As there are no other particles with the required properties available in the Standard Model—that is, to be neutral, massive, nonbaryonic and stable—, candidates beyond the Standard Model have to be found.

1.4.3. WIMPs

Good candidates for Weakly Interacting Massive Particles (WIMPs) are hypothetical particles predicted by supersymmetry (SUSY). Supersymmetry is an—up to now also hypothetical—extension of the Standard Model of particle physics invented to solve some of its problems such as the hierarchy problem, the question of gauge coupling unification and possibly the inclusion of gravity into the theory [Ber05, Mar97, Ste09]. In the Standard Model, all elementary matter particles (quarks and leptons) are fermions and all interactions between them are mediated by exchange particles, which are bosons. There are three families of fermions, four types of exchange bosons and the Higgs particle (see Table 1.1). In order to establish a symmetry between matter and interactions, supersymmetry assigns a fermionic partner to each boson and vice versa (see Table 1.2). This

Family	1	2	3
Squarks	$\begin{pmatrix}\tilde{u}\\ \tilde{d}\end{pmatrix}$	$\begin{pmatrix}\tilde{c}\\ \tilde{s}\end{pmatrix}$	$\begin{pmatrix}\tilde{t}\\ \tilde{b}\end{pmatrix}$
Sleptons	$\begin{pmatrix}\tilde{\nu}_e\\ \tilde{e}^-\end{pmatrix}$	$\begin{pmatrix}\tilde{\nu}_\mu\\ \tilde{\mu}^-\end{pmatrix}$	$\begin{pmatrix}\tilde{\nu}_\tau\\ \tilde{\tau}^-\end{pmatrix}$
Gauginos	$\tilde{B}^0$, $\tilde{W}^0$, $\tilde{W}^\pm$, 8 $\tilde{g}$		
Higgsinos	$\tilde{H}^0_1$, $\tilde{H}^0_2$		

Table 1.2.: Superpartners of the Standard Model particles. The $\tilde{\gamma}$ and $\tilde{Z}^0$ particles are orthogonal linear combinations of the $\tilde{B}^0$ and $\tilde{W}^0$ bosons.

superpartner should have the same quantum numbers, including mass but not spin, as the original particle, but particles with these properties are not observed in nature. Therefore supersymmetry has to be broken, allowing the superpartners to be much heavier than the corresponding Standard Model particles.

The bino $\tilde{B}^0$, wino $\tilde{W}^0$ and the two neutral Higgsinos $\tilde{H}^0_1$ and $\tilde{H}^0_2$ mix to form the neutralinos $\tilde{\chi}^0_1$, $\tilde{\chi}^0_2$, $\tilde{\chi}^0_3$ and $\tilde{\chi}^0_4$; the lightest of them, $\tilde{\chi}^0_1$, is stable due to conservation of R parity. R parity is a multiplicative symmetry introduced to explain the stability of the proton by conserving the following combination of lepton number L and baryon number B:

$$R = (-1)^{3B+L+2S}$$

(S is the spin of the particle). It has a value of $+1$ for Standard Model particles and -1 for supersymmetric particles; therefore, supersymmetric particles can only be produced and destroyed in pairs. The lightest neutralino is a neutral fermion with a mass between 100 GeV and 1 TeV and interacts only weakly with normal matter. Due to its high mass it could be the WIMP which forms Cold Dark Matter.

WIMPs are produced thermally in the early Universe. As WIMPs cluster gravitationally, there should be a lot of them in the halo of our galaxy. The Earth rotates around the Sun with a velocity of 30 km/s and the Sun rotates around the galactic centre with a velocity of 220 km/s. Depending on the season, these velocities either add up or point in opposite directions, therefore the velocity of the Earth relative to the galactic halo varies during the year. This leads to an annual modulation of the expected energy spectrum of WIMP recoils by scattering in a target of about 7 %. This effect can be used as a signature in direct WIMP searches (see section 1.5.3).

1.4.4. Axions

Axions are hypothetical particles introduced to solve the *strong CP problem* [Ste09]: the Lagrangian of quantum chromodynamics contains a term according to which the strong interaction should violate CP symmetry; however, unlike in the case of the weak interaction, strong CP violation is not observed in nature. Measurements of the electric dipole moment of the neutron give upper limits of 10^{-9} for the symmetry breaking parameter Θ. To solve this problem, a new U(1) symmetry called Peccei-Quinn symmetry is introduced, which is spontaneously broken at some scale f_a. The axion is the corresponding pseudo-Nambu-Goldstone boson which counteracts the original CP violating term. The mass of the axion is inversely proportional to the symmetry breaking scale f_a. The value of f_a is not yet known but expected to be quite high (between 10^9 and 10^{12} GeV). The axion is therefore probably very light (about $m_a \simeq 10^{-5}\,\text{eV}$). Nevertheless the axion can be Cold Dark Matter as it is not produced in thermal equilibrium.

1.4.5. Other Candidates

There are many other Dark Matter candidates, the most well-known of them are the gravitino and the axino [Ste09]. The gravitino is the superpartner of the graviton, the particle expected to mediate the gravitational force. The axino is the superpartner of the axion discussed in the previous section. Each of them could be the lightest supersymmetric particle (LSP) and would then be an extremely weakly interacting particle (EWIP) which cannot be detected in direct or indirect searches if R parity is conserved. If R parity is broken their decay products can be detected; also, the next-to-lightest supersymmetric particle (NLSP) might be found at colliders, it will however be difficult to distinguish this situation from scenarios in which it is the LSP.

1.4.6. Alternative Explanations

The interpretation of the observations taken as evidence for the existence of Dark Matter (see section 1.3) is based on the assumption that the known law of gravitation is exactly valid in the entire Universe. However, this is not yet proven and not necessarily the case. For a long time a possible explanation of the observations was that the acceleration is different from its Newtonian value. Newton's second law $\mathbf{F} = m\mathbf{a}$ is replaced by

$$\mathbf{F} = m\mu(\frac{a}{a_0})\mathbf{a}$$

with $\mu(\frac{a}{a_0} \gg 1) \approx 1$, $\mu(\frac{a}{a_0} \ll 1) \approx \frac{a}{a_0}$, a_0 the acceleration constant. This idea is called Modified Newtonian Dynamics (MOND) [Mil83]. A major drawback of this concept is that it introduces a specific scale into the law of gravitation, which cannot be explained from first principles and makes it difficult for this ansatz to be applicable to all the different scales at which deviations from Newton's law are observed if only the visible matter is taken into account. Constructing a relativistic theory from MOND is also problematic. With the obervation of the bullet cluster (section 1.3.6) MOND is now excluded; other theories of modified gravity, however, might still be an option [Bro07].

The following discussion will therefore assume the existence of Dark Matter and will concentrate on WIMPs as Dark Matter candidates.

1.5. Detection of Dark Matter

1.5.1. Interactions of Dark Matter

Particles can only be detected by observing their interactions. For some particles this is—at least in principle—easy, especially for charged particles like electrons or protons. For others it is more difficult. Dark Matter particles unfortunately are an extreme example of the latter case as they only very rarely interact. If the interaction takes place inside the detector, it can be observed directly; this is called *direct detection*. If the interaction happens outside the detector, it can still be observed if the interaction products make their way into the detector; this is called *indirect detection*. In principle, direct detection is preferable over indirect detection, as the particles interpreted to be interaction products of the Dark Matter in indirect detection could in reality also originate from other sources; however, there are also backgrounds in direct detection, such as recoils of neutrons produced by high energy muons. The shielding of this background is studied in the present work.

The two main interaction types of WIMPs are WIMP annihilation and elastic scattering off nuclei.

1.5.2. Indirect Detection of WIMP Annihilations

In indirect detection experiments, reaction products of WIMP annihilations such as photons, neutrinos, positrons and antiprotons are observed [Ber05]. WIMP annihilations will mainly take place in regions of increased WIMP density, such as halos and centres of galaxies and centres of stars. One possible detection of such WIMP annihilation products could be the observation of an increased positron fraction at high energies, e. g. by the satellite experiment PAMELA [Adr08, Adr09]. However, this is no proof for the detection of WIMPs as a positron excess could also originate from cosmic rays, possibly from the Geminga pulsar [Yük09]. Detection of a gamma ray line from WIMP annihilation would be a much clearer signature as it would be a sharp line at the mass of the WIMP and there are no known competing astrophysical processes in the expected energy range [Gon05]. Unfortunately, no such line has been observed up to now.

1.5.3. Direct Detection of WIMP Elastic Scattering

In direct detection experiments, the elastic scattering of WIMPs off target nuclei inside the detector is observed. In contrast to charged particles WIMPs scatter off the nucleus and not off the electron shell, leading to nuclear recoils instead of electron recoils. Suitable detectors can distinguish these types of recoil, thereby WIMPs can be discriminated from most of the radioactive background. Unfortunately neutrons also produce nuclear recoils, therefore the discrimination of WIMPs and neutrons is significantly more difficult and neutrons remain the most dangerous background. The interactions of WIMPs with nuclei can be either spin-dependent or spin-independent. In spin-dependent (axial vector) interactions the WIMPs couple to the spin J of the nucleons, the cross section is proportional to $J(J+1)$. In spin-independent (scalar) interactions the WIMPs couple to the mass of the nucleus, the cross section increases with the number of nucleons. The detection probability can therefore be increased by using heavy atoms as targets [Ber05].

Nuclear recoils can be detected by the phonons, ionization and scintillation they produce. As their energy depositions are small (about a few ten keV), very sensitive detectors and a very low radioactive background are required.

A good choice are cryogenic calorimeters. At low temperatures the heat capacity C_v depends cubically on the temperature:

$$C_v \propto \left(\frac{T}{T_D}\right)^3$$

where T_D is the Debye temperature of the material. The detectors are crystals which are cooled to temperatures between 10 and 50 mK in order to decrease the heat capacity, which increases the sensitivity to small energy depositions. An incoming particle produces high frequency phonons, which expand through the crystal with a velocity of about 1/3 of the velocity of sound. They interact with the crystal by elastic scattering and anharmonic decay. If the frequency of the phonons has become sufficiently low, they become ballistic and move with the velocity of sound. Their mean free path length becomes large and exceeds the size of the crystal; if they hit the walls they are scattered back into the crystal unless they are extracted by a metal absorber. Over time the ballistic phonons thermalize [Ake05, Mar93].

There are two common types of phonon detectors: Neutron transmutation doped germanium crystals, which can only detect the slower signals of thermal phonons, and superconducting phase thermometers (SPT), which can also detect the faster signals of nonthermal phonons.

Neutron transmutation doped (NTD) germanium crystals are high-resistance thermistors (temperature-dependent resistors) which are operated close to the metal-insulator transition. A change in temperature ΔT leads to a change in resistance ΔR which is measured as a change in voltage ΔV by biasing the sensor with a constant current.

Superconducting phase transition thermometers (SPT; also called transition edge sensors, TES [Irw05]) have low resistance and consist of metallic phonon collecting strips typically made of aluminum connected to a film often made of tungsten stabilised on the superconducting-to-normal phase transition. A small change in temperature ΔT therefore leads to a large change in resistance ΔR. As the temperature change induced by the interaction of the particle is much smaller than the width of the transition, the relation between ΔR and ΔT is approximately linear. The change in resistance is read out as a current change by a SQUID readout system.

Cryogenic scintillators can be used to simultaneously measure scintillation and phonons. In this case the detector consists of a large crystal in which the particle interacts and which detects the phonons produced in the interaction, and a separate detector in which the scintillation light is detected via the phonons it produces there. The amount of scintillation light produced by nuclear recoils is much smaller than that produced by electron recoils of the same energy (quenching), therefore these types of events can be separated. A discrimination efficiency of 99.7% at 15 keV can be achieved [Meu99]. This technique is used, e. g., in the CRESST-II experiment which is located in the Laboratori Nazionali del Gran Sasso (LNGS) underground laboratory inside the Gran Sasso mountain, Italy. It uses up to 33 $\mathrm{CaWO_4}$ detector modules with a mass of about 300 g each. The ballistic phonons are read out by W TES. The current limit for spin independent WIMP-nucleon scattering obtained with an exposure of $48\,\mathrm{kg}\cdot\mathrm{days}$ is $4.8 \times 10^{-7}\,\mathrm{pb}$ for a $50\,\mathrm{GeV}/c^2$ WIMP [Ang09].

Cryogenic germanium detectors can be used to simultaneously measure ionization and phonons. A nuclear recoil produces less ionization than an electron recoil of the same energy, allowing event by event discrimination; however, incomplete charge collection of electron recoil events taking place close to the surface of the detector is a problem, as it mimicks nuclear recoil events. As nonthermal phonons still contain information on the position inside the detector at which the interaction took place, by their detection this problem can be circumvented. CDMS II operates 19 germanium detectors with masses of 230 g each as well as 11 silicon detectors with masses of about 100 g each in the Soudan Underground Laboratory in Minnesota, USA, to detect nonthermal phonons with TES [Ake05], while EDELWEISS, operating 10 germanium detectors of 400 g each in the Laboratoire Souterrain de Modane (LSM) at the Frejus tunnel close to the French-Italian border, mainly detects thermal phonons with NTD thermistors [Arm11, San05]. The current limit for the spin-independent WIMP-nucleon cross section given by CDMS II is $3.8 \times 10^{-8}\,\mathrm{pb}$ for a $70\,\mathrm{GeV}/c^2$ WIMP based on an exposure of $612\,\mathrm{kg}\cdot\mathrm{days}$[Ahm09b]. EDELWEISS II gives a limit of $4.4 \times 10^{-8}\,\mathrm{pb}$ for a $85\,\mathrm{GeV}/c^2$ WIMP from $384\,\mathrm{kg}\cdot\mathrm{days}$ of exposure [Arm11].

Liquid noble gas detectors are used for the simultaneous detection of scintillation and ionization [Bol99, Yam03]. Common materials for this type of detector are liquid xenon and liquid argon, which are good scintillators. The detectors contain a liquid as well as a gaseous phase. The particle interacts in the liquid phase. The scintillation is observed directly in the liquid phase by an array of photomultipliers. The ionization electrons are extracted by a high electric voltage to the gaseous phase, in which they produce proportional scintillation which is detected by another array of photomultipliers. The ratio of the two signals is different for electron and nuclear recoils, allowing event by event discrimination. Additionally, the position of the event can be reconstructed in 3 dimensions. Therefore a fiducial volume can be defined in which the background rate is lower, as many background particles are stopped already in the outer parts of the detector due to the high stopping power of liquid xenon. Advantages of this type of detector compared to cryogenic detectors are the relatively moderate operating temperature of 180 K (compared to several mK) and the quite large masses. The XENON collaboration has used this techique at Gran Sasso successfully to determine the currently best limits for WIMP interactions: $7.0 \times 10^{-9}\,\mathrm{pb}$ for the spin-independent cross section of a $50\,\mathrm{GeV}/c^2$

WIMP in XENON100 with 1471 kg · days of exposure [Apr11, Apr12] and 5×10^{-3} pb for the spin-dependent pure neutron cross section of a 30 GeV/c^2 WIMP in XENON10 with about 136 kg · days of exposure [Ang08b].

The only experiment actually claiming direct detection of Dark Matter up to now is the DAMA experiment [Ber08] located at Gran Sasso. Its current incarnation DAMA/LIBRA is a 250 kg NaI(Tl) scintillation detector operated at ambient temperature in the Gran Sasso underground laboratory. The detection signature used is the annual modulation of the WIMP signal (see also section 1.4.3). The collaboration claims a Dark Matter detection with 8.9 σ confidence level based on an exposure of 1.17 tonne · days [Ber10]. The CoGeNT experiment operating a 440 g germanium detector in the Soudan laboratory has also observed a signal which could be interpreted as originating from light WIMPs [Aal11]. Together with the DAMA/LIBRA result a cross section of 2×10^{-4} pb for a 7 Gev/c^2 WIMP can be deducted [Hoo10]. CRESST II has now reached an exposure of 730 kg · days and also observed something which could be interpreted as a WIMP signal [Ang12]. However, the allowed regions of WIMP masses and cross sections extracted from these evidences contradict the exclusion lines obtained by CDMS II and XENON100. Specifically, for low mass WIMPs with masses below about 7 GeV/c^2 CDMS II currently provides the best conservative limits for the spin-independent WIMP-nucleon and the spin-dependent WIMP-neutron cross sections [Ahm11].

Experimental results as well as SUSY predictions are shown in Figs. 1.11 and 1.12. For most experiments an exclusion limit for the cross section as a function of the WIMP mass is given, meaning that the parameter space above the line is excluded by the data. DAMA/LIBRA, CoGeNT and CRESST II evidences as well as SUSY predictions result in evidence regions of allowed parameter ranges. The experimental evidence regions are almost completely excluded by more sensitive measurements and the supersymmetric predictions extend to much lower cross sections than the current experiments and their future extensions are expected to reach. Therefore new experiments are needed which extend their sensitivity to smaller cross sections (10^{-10} pb). The European Underground Rare Event Calorimeter Array (EURECA), to be constructed in an extension of the Frejus underground laboratory, is such an experiment. It will be discussed in more detail in section 5.2.1.

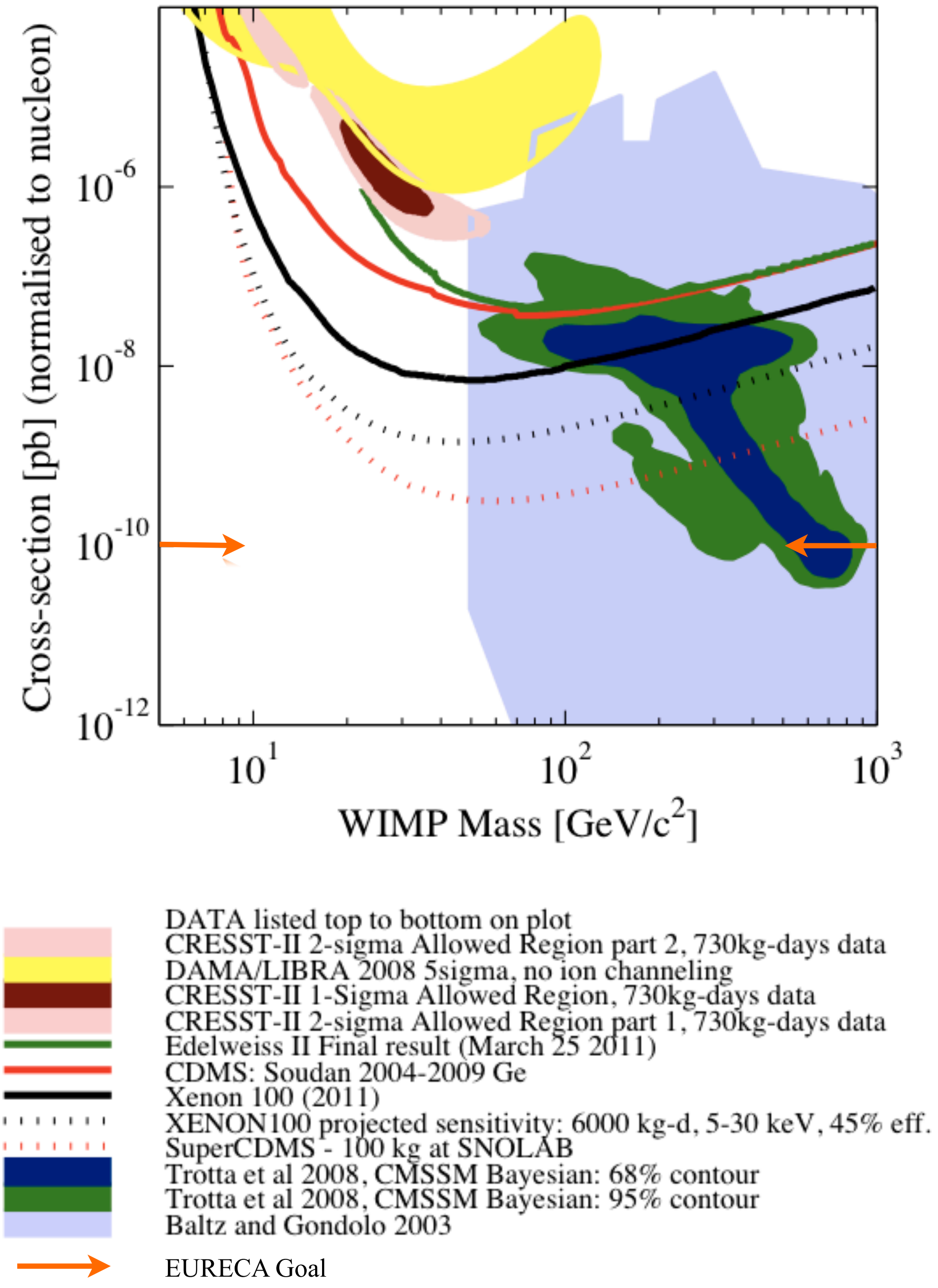

Figure 1.11.: Current WIMP evidence and allowed regions, exclusion limits and SUSY predictions for spin-independent interactions as a function of WIMP cross section and mass [Gai12]

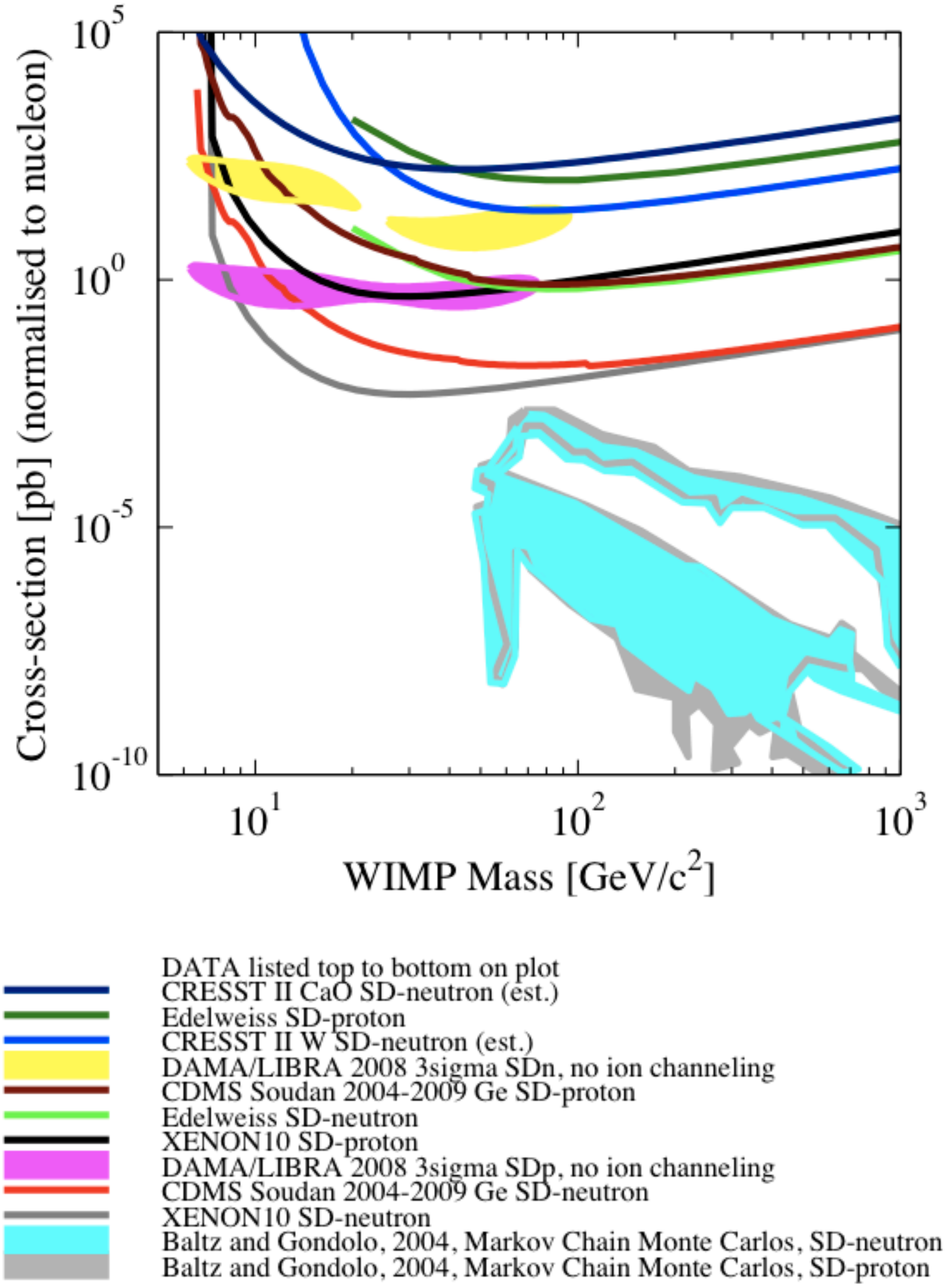

Figure 1.12.: Current WIMP evidence regions, exclusion limits and SUSY predictions for spin-dependent interactions as a function of WIMP cross section and mass. The experimental results do not even reach into the region of the theoretical predictions. Note that results of different experiments are not directly comparable as different target nuclei are being used [Gai12].

2. Normal Matter

2.1. Cosmic Rays

Cosmic rays are particles coming from space into the atmosphere of the Earth. They have been discovered by Viktor Hess in 1912 [Hes12]. Their study is interesting not only by itself but has also triggered many important developments in physics: Antiparticles, pions and muons were discovered in cosmic rays in the 1930's and 1940's, leading to the development of particle accelerators and the Standard Model of particle physics. The first strong evidence for neutrino oscillations—which was the first hint to physics beyond the Standard Model—came from observations of atmospheric neutrinos which are produced by cosmic rays in the atmosphere of the Earth.

The energy spectrum of cosmic rays follows a power law [Per03]:

$$\frac{dN}{dE} \propto E^{-\gamma}$$

with γ=2.7 for energies below the so-called *knee* at $10^{15} - 10^{16}$ eV and γ=3.0 for higher energies up to the *ankle* at 10^{19} eV (see also Fig. 2.1). The acceleration of charged particles to energies up to $10^{14}\,Z$ eV is supposed to happen in supernova shock waves; for higher energies, the acceleration mechanism is still unknown.

Cosmic rays originate mainly in our galaxy; however, the origin of the particles with the highest energies (above 10^{20} eV) is still unclear. On the one hand they should be of extragalactic origin since the galactic magnetic field could not contain them inside the galaxy. On the other hand, protons with energies above $\sim 6 \cdot 10^{19}$ eV lose energy quickly via pion photoproduction

$$\gamma + p \to \Delta^+ \to p + \pi^0$$

$$\gamma + p \to \Delta^+ \to n + \pi^+$$

which limits their range to ~50 Mpc (Greisen-Zatsepin-Kuzmin cutoff [Abb08, Gre66, Zat66]) so their sources should be nearby; however, no such sources are known at the moment. Whether the flux of cosmic rays at the highest energies is actually attenuated or not is currently unclear [Abb08, Abr08, Aug10, Sok10, Tak03].

Neutral cosmic rays are γ particles, neutrinos and antineutrinos.

Charged primary cosmic rays (i.e. the ones coming directly from the original sources) consist of 86% protons, 11% α-particles, 1% heavier nuclei and 2% electrons. The small amounts of positrons and antiprotons observed are believed to originate from interactions

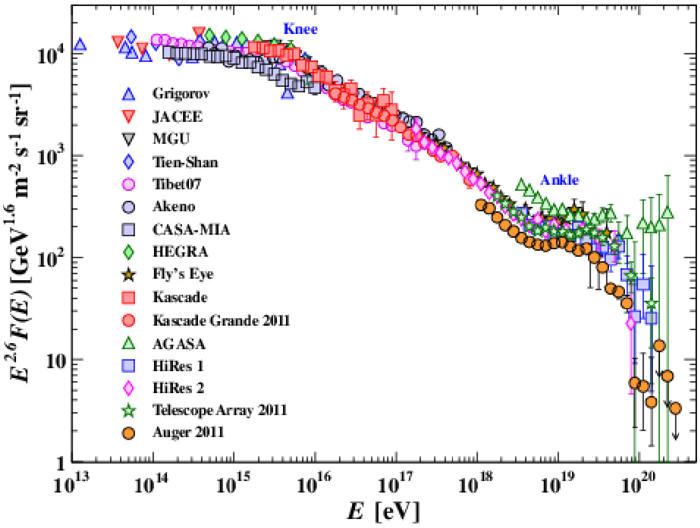

Figure 2.1.: Spectrum of cosmic rays [PDG10]

of the primary particles with the interstellar gas. The chemical composition of the cosmic rays is also modified by interactions: most of it is comparable to the distribution of elements in the solar system; however, Li, Be and B as well as Sc, Ti, V, Mn, which are quite rare in the solar system as they are easily destroyed during stellar nucleosynthesis, are significantly more abundant in the cosmic rays since they are produced by spallation of the abundant C, O and Fe, Ni nuclei.

Charged cosmic rays interact in the atmosphere producing especially pions and kaons. Pions can be either charged (π^+, π^-) or neutral (π^0). Charged pions with energies below about 100 GeV mainly decay in flight, resulting in muons:

$$\pi^+ \to \mu^+ + \nu_\mu, \qquad \pi^- \to \mu^- + \bar{\nu}_\mu$$

Higher energy pions often undergo nuclear interaction instead of decaying, therefore the energy spectrum of the daughter muons is steeper by $1/E$ than that of the pions or the primary protons. Neutral pions have an extremely short lifetime of $8 \cdot 10^{-17}$ s and decay to photons:

$$\pi^0 \to 2\gamma$$

which develop electromagnetic cascades.

In the interactions of cosmic rays in the atmosphere short-lived particles, e. g. charm mesons, are also produced. Their decays can generate muons, the so-called “prompt” muons. As charmed particles decay rather than interact because of their short lifetimes, the spectrum of these prompt muons is not steepened by $1/E$ but has the same exponent as the primary spectrum, therefore at very high energies prompt muons will dominate the muon flux although their parents initially are produced in much smaller quantities. Prompt muons are distributed isotropically [Gai90].

On their arrival on Earth cosmic rays with energies above 30 GeV are distributed isotropically. At lower energies, the east-west effect and the anticorrelation with the solar cycle play a role; see, e. g., [Per03].

Due to their relatively long lifetime ($2.2 \cdot 10^{-6}$ s) and small cross section high energy muons are the most penetrating component of cosmic rays. For example, a 3 GeV muon has a decay length of 20 km and can pass the entire atmosphere without decay or interaction. Higher energetic muons can even propagate through large amounts of rock. This is the reason why Dark Matter searches and other low background experiments have to be carried out at as large depths underground as possible.

On the surface, muons are distributed isotropically in azimuthal angle, while their zenith angle distribution varies with $1/\cos\theta$ due to the larger thickness of atmosphere they have to cross. The differential muon energy spectrum on Earth at energies above 10 GeV, at which muon decay and energy loss may be neglected, can be approximated by [Gai90]:

$$\frac{dN_\mu}{dE_\mu} \approx \frac{0.14 E_\mu^{-2.7}}{\mathrm{cm^2\,s\,sr\,GeV}} \left\{ \frac{1}{1 + \frac{1.1 E_\mu \cos\theta}{115\mathrm{GeV}}} + \frac{0.054}{1 + \frac{1.1 E_\mu \cos\theta}{850\mathrm{GeV}}} \right\}$$

The first term inside the brackets represents the muons originating from pion decay, the second the ones from kaon decay. At angles θ larger than 60° the curvature of the Earth has to be taken into account. The zenith angle θ on the surface of the Earth is connected to the zenith angle θ^* at the top of the atmosphere by the relation $\sin\theta = \sin\theta^* \frac{R_E + H_{\mathrm{int}}}{R_E}$ with $R_E = 6600\,\mathrm{km}$ being the Earth radius and $H_{\mathrm{int}} = 18.6\,\mathrm{km}$ the mean interaction height for primary particles in the atmosphere [Hor07, Rho93].

Underground the muon distribution reflects the topography of the rock overburden. Therefore, to study the muon background in an underground experiment the mountain profile has to be known as precisely as possible.

2.2. Interactions of Muons

Muons can interact with matter either continuously by ionization of the surrounding material or discretely by the radiative processes bremsstrahlung, pair production and nuclear interaction. In bremsstrahlung and pair production electrons, positrons and gammas are produced, which in turn can undergo bremsstrahlung and pair production, leading to the development of electromagnetic showers. In a similar way, hadronic showers can be induced by the nuclear interaction of muons. In hadronic showers also neutrons are produced which are the most dangerous background in Dark Matter search experiments, therefore it is important to know the numbers of neutrons as precise as possible. To determine these numbers for muon-induced neutrons is the topic of the present work.

2.2.1. Ionization

The energy loss of muons by ionization is given by the Bethe-Bloch formula [Bet30, PDG10]:

$$-\frac{dE}{dx} = 4\pi N_A r_e^2 m_e c^2 z^2 \frac{Z}{A}\frac{1}{\beta^2}\left[\frac{1}{2}\ln\frac{2m_e c^2\beta^2\gamma^2 T_{\max}}{I^2} - \beta^2 - \frac{\delta(\beta\gamma)}{2}\right]$$

with N_A Avogadro's number, $r_e = \frac{e^2}{4\pi\epsilon_0 m_e c^2}$ the classical electron radius, m_e the mass of the electron, ze the charge of the incoming particle (in this case the muon), Z the atomic number and A the atomic mass of the absorber, $T_{\max}$ the maximum kinetic energy which a free electron can obtain in a single collision, I the mean excitation energy, $\beta = \frac{v}{c}$ and $\gamma = \frac{1}{\sqrt{1-\beta^2}}$ the usual kinematic variables and $\delta(\beta\gamma)$ the density effect correction. $T_{\max}$ is given by

$$T_{\max} = \frac{2m_e c^2\beta^2\gamma^2}{1 + 2\gamma m_e/m_\mu + (m_e/m_\mu)^2}$$

with m_μ the mass of the muon. The determination of I is difficult; values are recommended by the International Commission on Radiation Units & Measurement (ICRU) [ICRU49]. The density effect correction is usually calculated by Sternheimer's parameterization [Ste71].

The ionization energy loss is approximately $2\,\mathrm{MeV}/(\mathrm{g}\cdot\mathrm{cm}^2)$.

2.2.2. Bremsstrahlung

In bremsstrahlung a photon is emitted by the interaction of the muon with matter. The cross section has originally been calculated by Bethe and Heitler [Bet34]. In GEANT4 an improved version by Kelner, Kokoulin and Petrukhin is used [G4PRM, Kel95]:

$$\begin{aligned}\frac{\mathrm{d}\sigma(E,\epsilon,Z,A)}{\mathrm{d}\epsilon} &= \frac{16}{3}\alpha N_A\left(\frac{m_e}{m_\mu}r_e\right)^2\frac{1}{\epsilon A}Z(Z\Phi_n + \Phi_e)(1 - v + \frac{3}{4}v^2)\\ &= 0 \quad \text{if} \quad \epsilon \geq \epsilon_{\max} = E - m_\mu\end{aligned}$$

with α the fine structure constant, N_A Avogadro's number, m_e and m_μ the masses of the electron and muon, respectively, r_e the classical electron radius, E the initial total energy of the muon, $\epsilon = E - E'$ the energy of the emitted photon, Z the atomic number and A the atomic mass of the absorber and $v = \epsilon/E$ the relative energy transfer of the muon. Φ_n and Φ_e are the contributions of the nucleus and of the electron, respectively; for details see [G4PRM].

2.2.3. Pair Production

In pair production, an electron-positron pair is generated by the muon. The differential cross section is given by [G4PRM]

$$\sigma(Z,A,E,\epsilon) = \frac{4}{3\pi}\frac{Z(Z+\zeta)}{A}N_A(\alpha r_0)^2\frac{1-v}{\epsilon}\int_0^{\rho_{\max}} G(Z,E,v,\rho)\mathrm{d}\rho$$

with

$$G(Z,E,v,\rho) = \Phi_e + \left(\frac{m_e}{m_\mu}\right)^2 \Phi_\mu$$

ζ is the inelastic atomic form factor contribution from pair production on atomic electrons. Z the atomic number and A the atomic mass of the material, N_A Avogadro's number, α the fine structure constant, ϵ the total energy of the produced pair corresponding to the energy loss of the muon $E-E^{'}$, $v=\epsilon/E$ the fractional energy loss. Φ_e and Φ_μ are complicated QED functions and also take atomic and nuclear cross sections into account; formulas are given in [G4PRM, Loh85].

2.2.4. Nuclear Interaction

Muon nuclear interaction is especially important at high muon energies ($E \geq 10\,\mathrm{GeV}$), high energy transfers ($\nu/E \geq 10^{-2}$) and for light target materials. The contribution of this process to the total energy loss increases almost linearly with energy, reaching about 10% for TeV muon energies. The cross section and energy loss is dominated by the low Q^2 region ($Q^2 \ll 1\,\mathrm{GeV}^2$). The electromagnetic interaction of the muon with the nucleus is mediated by a virtual photon. In this sense the muon nuclear interaction is comparable to the photonuclear interaction (see section 4.1.2.7).

It can be described by the Borog and Petrushkin formula for the cross section [Bor75], which is based on Hand's formalism for inelastic muon scattering [Han63], a vector dominance model with parameters estimated from experimental data for the inelastic form factor and theoretically parameterized nuclear shadowing effects [Bro72]. If the same photonuclear cross section is used it agrees to better than 10% with the formula given by Bezrukov and Bugaev. For $E \geq 10\,\mathrm{GeV}$ it can be written as [G4PRM]

$$\sigma(E,\nu) = \Psi(\nu)\Phi(E,v)$$

$$\Psi(\nu) = \frac{\alpha}{\pi}\frac{A_{\mathrm{eff}}N_A}{A}\sigma_{\gamma N}(\nu)\frac{1}{\nu}$$

$$\Phi(E,v) = v-1+\left[1-v+\frac{v^2}{2}\left(1+\frac{2m_\mu^2}{\Lambda^2}\right)\right]\ln\frac{\frac{E^2(1-v)}{m_\mu^2}\left(1+\frac{m_\mu^2 v^2}{\Lambda^2(1-v)}\right)}{1+\frac{Ev}{\Lambda}\left(1+\frac{\Lambda}{2M}+\frac{Ev}{\Lambda}\right)}$$

with α the fine structure constant, N_A Avogadro's number, A the atomic mass of the material, ν the energy lost by the muon, $v=\nu/E$, m_μ the muon and M the nucleon mass. Λ is a vector dominance model parameter estimated to be $\Lambda^2 = 0.4\,\mathrm{GeV}^2$. The effect of nuclear shadowing is included in A_{eff}, which is parameterized as

$$A_{\mathrm{eff}} = 0.22A + 0.78A^{0.89}$$

A possible dependence on ν and E is currently neglected in this formalism.

For the photonuclear cross section $\sigma_{\gamma N}$ the parameterization of Caldwell of experimental data of real photoproduction [Cal79] is chosen:

$$\sigma_{\gamma N} = \left(49.2 + 11.1 \ln K + 151.8 K^{-1/2}\right) \cdot 10^{-30}\,\mathrm{cm}^2, K \,\text{in }\, \mathrm{GeV}$$

which should be valid at least up to 100 TeV.

2.3. Muons Underground

On their way through atmosphere and rock muons lose about $2\,\mathrm{MeV}/(\mathrm{g}\cdot\mathrm{cm}^2)$ by ionization; at higher energies the energy loss rate $\frac{dE}{dx}$ increases slowly with muon energy E_μ and can be approximated to better than 5% for $E_\mu > 10\,\mathrm{GeV}$ by [Gai90]

$$-\frac{dE}{dx} \approx \left(1.9 + 0.08 \ln \frac{E_\mu}{\mathrm{GeV}}\right) \left[\frac{\mathrm{MeV}}{\mathrm{g/cm}^2}\right]$$

At even higher energies also the other energy loss processes bremsstrahlung, pair production and inelastic scattering on nuclei become important; their energy loss rate is proportional to the muon energy. Therefore, the average muon energy loss can be written as

$$-\frac{dE(E_\mu)}{dx} = a(E_\mu) + b(E_\mu)E_\mu$$

with $a(E_\mu)$ the ionization energy loss and $b(E_\mu) = b_{\mathrm{brems}}(E_\mu) + b_{\mathrm{pair}}(E_\mu) + b_{\mathrm{inelastic}}(E_\mu)$ the sum of the radiative contributions.

Neglecting fluctuations the relation between the initial and final energies of a muon passing a distance x is given by

$$x = \int_E^{E_0} \frac{dE_\mu}{\langle dE(E_\mu)/dx \rangle}$$

If a and b are energy-independent, this can be expressed as

$$E = (E_o + \epsilon)e^{-bx} - \epsilon$$

where $\epsilon = a/b$ is the critical energy above which the radiative energy losses become more important than the ones due to ionization. In the case of the Frejus laboratory with mean depth $\langle x \rangle = 4600\,\mathrm{m\,w.e.}$, where EURECA is planned to be located, $a =$

0.217 GeV/m w.e., $b = 4.38 \cdot 10^{-4}$/m w.e. and therefore $\epsilon = 495$ GeV [Hor07]. The minimum energy a muon has to have initially in order to reach depth x is therefore

$$E_0^{\text{min}} = \epsilon(e^{bx} - 1)$$

In the Frejus laboratory $E_0^{\text{min}} = 3.22$ TeV. For a primary muon differential power spectrum $KE_0^{-\gamma_\mu}$ (with E_0 the initial muon energy and K the normalization factor) the muon spectrum at a depth x will be [Lip91]:

$$\frac{dN}{dE_\mu} = Ke^{-bx(\gamma_\mu - 1)} \left[E_\mu + \epsilon \left(1 - e^{-bx} \right) \right]^{-\gamma_\mu}$$

For each specific depth this expression can be simplified by combining the constants

$$\frac{dN}{dE_\mu} = K_1 \left[E_\mu + K_2 \right]^{-\gamma_\mu}$$

with $K_1 = Ke^{-bx(\gamma_\mu - 1)}$, $K_2 = \epsilon \left(1 - e^{-bx} \right)$ and $\gamma_\mu = 3.7$ (note that $\gamma_\mu = \gamma + 1$ due to pion decay). The unit "m w.e." stands for "metres water equivalent". It is used to normalize the shielding effectiveness of different materials and gives the thickness of water which has the same shielding effectiveness as the material under consideration.

2.4. Neutron Background

Detectors typically used in a Dark Matter search experiment can discriminate between electron and nuclear recoils (see section 1.5.3). This removes most of the potential background, as photons and electrons interact via electron recoils. However, neutrons remain as background as they produce only nuclear recoils and can be distinguished from WIMPs only if they scatter in multiple parts of a segmented detector, which is not always the case. The neutron flux in the detector therefore limits the sensitivity of the experiment and should be minimized. As the mass of the neutron is approximately the same as the mass of hydrogen, scattering of neutrons is especially effective on hydrogen. Hydrogen-rich materials such as polyethylene are therefore suitable as neutron moderators.

There are four types of neutron background in an underground experiment [Wul04b]:

- low energy neutrons ($<$ 10 MeV) from local radioactivity
    - induced by fission and (α, n) reactions due to uranium and thorium activities in the surrounding rock and concrete; this is the biggest part of the flux. It can be shielded by hydrogen-rich shielding material.
    - induced by spontaneous fission in the shielding material and the experimental setup. This contribution can be minimized by using radiopure detector material and shielding.

- high energy neutrons induced by cosmic ray muons via muon photonuclear interaction and via the electromagnetic and hadronic showers produced by the muons
    - in the rock; these neutrons can produce additional neutrons by spallation in the shielding material. They are the hardest to get rid of as they can neither be shielded (due to their high energy) nor vetoed (unless there is some kind of muon veto inside the rock, as the corresponding muons do not pass the experimental setup)
    - in the shielding material. They can be vetoed by a muon veto located outside the shielding.

At a depth of several thousand m w.e., where Dark Matter search experiments are typically located, the flux of high energy neutrons is about 3 orders of magnitude lower than that of low energy neutrons. Nevertheless it is extremely important to take into account as it may be the limiting factor for the sensitivity of the experiment due to the following reasons [Wul03, Bau04]:

- Due to their high energies they can reach a detector which is located far away from the track of the associated muon, making it unlikely that this muon is seen in the muon veto.
- They can transfer a large amount of energy to a nucleus in a reaction. Therefore their nuclear recoils are usually above detector threshold, leading to an increase of the background, while the recoils induced by the low energy neutrons often remain undetected.
- The hydrogen-rich shielding material commonly used against low energy neutrons doesn't protect against high energy neutrons, but is itself a target for high energy muons in which additional neutrons can be produced.

The present work is concerned with muon-induced neutrons only, neutrons from radioactivity are studied in [Sch11]. The aim in both cases is to determine the respective neutron flux inside the laboratory and to find the most effective shielding strategy. This is done by simulation of the interactions of muons in different shielding designs. A short introduction to computer simulations is given in the following chapter.

3. Monte Carlo Simulations

3.1. Introduction

Monte Carlo methods are based on the use of random numbers and probability to solve problems [Wit04]. They are often used if analytical methods are too difficult or completely unavailable, or if the precise values of the input parameters are unknown and are represented by appropriate probability distributions. A simple example is the determination of π [Wol96] (see also Fig. 3.1): put a circle inside a square so that the diameter of the circle matches the edge length of the square and distribute points randomly but equally over the whole area. From the ratio of the number of points inside the circle to the number of points inside the square π can be determined; however it takes a huge number of points to get a precise value. The interaction of particles with matter can be simulated in a similar way. Primary particles are chosen randomly according to their energy and momentum distribution and transported stepwise through the geometry. At each step the physics processes taking place are selected randomly according to their probability. By simulating a large amount of particles the expected behaviour of the whole population of primary particles is approximated. The final goal is to determine how particles are "seen" by a detector, i.e. how much energy is deposited at which point in space and time.

3.2. A Simulation Run—Step By Step

Similar to a real experiment Monte Carlo simulations of particle interactions also come in the form of *runs*. A run is a sequence of *events*, usually a predefined number of them, simulated in one go. An event consists of the simulation of one or more primary particles and all their secondaries. The primary particles are produced by a particle source at a certain point in space at time zero of the respective event. Their kinetic energy and momentum direction are selected randomly according to the true energy and momentum distributions applicable to the situation. The starting point can be smeared out to take into account the actual size of the particle source. The particles are then transported stepwise through the simulation geometry. The geometry has to consist of all geometrical objects which are relevant for the outcome of the experiment. Obviously this includes the detector and all objects through which the particles pass on their way from the source, but objects located close enough nearby should also be taken into account. The length of the steps is determined by the physics processes: at the beginning of each step all

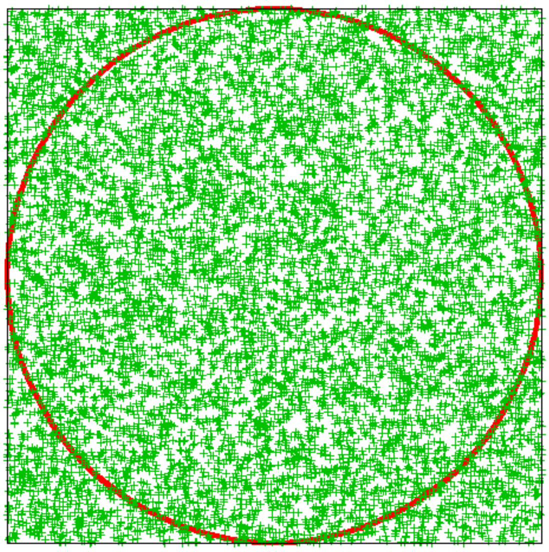

Figure 3.1.: Monte Carlo determination of π: Put a circle inside a square, distribute points randomly over the whole area and take the ratio of the points within the circle to all points. In the above picture 7799 out of 10000 points lie inside the circle, corresponding to a value of 3.1196 for π. Using a large number of points is important to obtain precise results from a simulation.

processes registered for this particle type suggest a step length, the shortest suggested length is actually taken. All continuous processes (e. g. ionization) are then carried out. A discrete process (e. g. photoelectric effect) is only taking place if it suggested the shortest step length. If a process involves energy loss, the energy is deposited at that point. If a process intends to produce secondary particles, they are created if their expected range in the material is at least the minimum required range or if their creation is enforced, else their energy is also deposited. All particles which are actually created are tracked until they have no kinetic energy left, disappear by a reaction or leave the simulated volume, which is called *world volume*. If particles deposit energy in a sensitive detector, after each step *hits* can be created to buffer information on the energy deposition until the end of the event, at which point the data can be analyzed or stored permanently.

While the principles of particle simulation as described above are valid in general, details may vary between different simulation codes. The previous description is based on the simulation toolkit Geant4 which has been used in this work and is described in more detail in the next section. In GEANT3 [Geant3], its FORTRAN-based predecessor, particles are automatically stopped and killed when their energy falls below a cut value given in energy. As described above, Geant4 uses a single *production threshold in range* instead, which is then converted to energy according to particle type and material. The advantages over a *tracking cut in energy* are as follows [G4UAD, Wri07]:

1. The energy deposition takes place at the correct point in space. With an energy

Material	electron	positron	gamma
Air	990 eV	990 eV	990 eV
Natural Ge	658.44 keV	626.80 keV	16.96 keV
Enriched Ge	634.56 keV	604.07 keV	16.67 keV
CaWO4	708.91 keV	674.85 keV	45.71 keV
Water	274.74 keV	268.06 keV	2.49 keV
Liquid Helium	78.27 keV	77.31 keV	990 eV
Plastic Scintillator	281.59 keV	274.74 keV	2.08 keV
Lead	1.00 MeV	940.93 keV	94.72 keV
Copper	1.03 MeV	976.33 keV	20.52 keV
Steel	952.58 keV	906.81 keV	16.97 keV
PE	274.74 keV	268.06 keV	1.96 keV
LNGS Rock	478.09 keV	460.75 keV	5.62 keV
LNGS Concrete	427.95 keV	412.43 keV	5.38 keV
Frejus Rock	478.09 keV	466.46 keV	5.73 keV

Table 3.1.: The production threshold for secondary particles which is used by default in Geant4 physics lists (0.7 mm) is converted to energy for the materials used in the present work.

cut, on the other hand, the spatial resolution of the energy deposition depends on the material as well as on the particle type.

2. The simulation is more efficient by automatically producing the “right” amount of secondaries: For example, in a liquid argon–lead sandwich calorimeter, energy loss electrons are produced in argon but not in lead. With an energy cut one can choose between setting a suitable energy threshold for the scintillator, producing too many electrons in lead which are of no interest to the experiment and only unnecessarily consume CPU time, or setting a suitable energy threshold for the lead, thereby missing many potentially interesting secondaries in the argon.

In the present work the standard production threshold of the QGSP_BIC_HP physics list (see chapter 4.1.1) of 0.7 mm is used. The versions of Geant4 used in this work honor the production threshold only for electrons, positrons and gammas. The corresponding energies for the different materials used are given in Table 3.1.

3.3. Geant4 Overview

Geant4 is a toolkit for the simulation of the passage of particles through matter by the Monte Carlo method [Geant4]. It has started development as the RD44 project at CERN in 1993 as the successor to the Fortran-based GEANT3 [Geant3] and is now maintained by the international Geant4 collaboration, at the time of writing consisting of about 100 scientists and software engineers from about 50 institutions worldwide. It is written in the programming languages C++ [Str97] according to the principles of object-oriented software design: the whole system is split up into small parts which communicate via clearly defined interfaces only and can therefore be developed independently, making distributed development possible in the first place. This modularity enables the user to easily select which physics processes and models describing them should be enabled in the simulation.

Geant4 is selected as the tool of choice for the present work because it promises to be able to treat all the required physics processes in one single simulation, from the muons hitting the surface of the mountain down to the recoils in the detector. In previous works simulations often had to be split up into different parts as the simulation codes used could only treat part of the required physics. For example, in simulations of the muon-induced neutron background in CRESST [Wul03] the neutron production by muons is simulated with FLUKA [Fas00] while the nuclear recoils of the neutrons are treated with MCNP [Bri97]. It is not possible to use only one of these codes for both tasks as MCNP does not contain muon nuclear interaction and is therefore unsuitable for the simulation of neutron production while FLUKA treats nuclear recoils only statistically but not for each individual neutron. However following individual particle tracks is necessary for the following reasons: (i) to study correlations between the production of neutrons and charged particles which can be seen in the muon veto, thereby removing the corresponding neutrons from the background of the experiment, (ii) to treat the multiple scattering of neutrons which allows their discrimination from WIMPs which will scatter only once, and (iii) to include neutrons produced by muons in the experimental setup [Bau04]. Geant4 covers all the relevant physics processes over the whole energy range and is therefore, at least in principle, the ideal tool for this task.

Geant4 is a highly modular system in which the user can influence almost every aspect of the simulation. This is in stark contrast to its predecessor GEANT3 where the user has to input the geometry but which is more or less fixed with respect to the physics processes simulated, the models describing them and the output obtained. On the one hand, this new flexibility of GEANT4 has the advantage that the simulation can be tailored individually to its specific needs. A typical example is choosing the right balance between precision and speed, especially with respect to hadronic processes, which can only be approximated by models as there is no exact theory. On the other hand, as almost nothing is predefined, it is the sole responsibility of the user to put everything together correctly, which requires a substantial amount of knowledge and leaves a lot of room for mistakes. This is especially true with respect to the selection of physics processes and models. A *process* is a physical effect such as photoelectric effect, ionization, or elastic scattering. A *model* is a description of such a process. Sometimes a model covers only a certain energy range, sometimes it is possible to choose between several different models describing the same physics process, especially if there is no unambiguous theory which is the case for most hadronic processes. At most two different models describing the same process at the same energy can be selected simultaneously in Geant4. All processes and models which should be taken into account in the simulation have to be enumerated in a *physics list*. For most of the processes and models their physics content is described in

[G4PRM]; however, that document gives only vague advice on which models to choose for any given application. Fortunately, the situation has improved quite a bit during the course of this work as the selection of predefined physics lists provided by the Geant4 collaboration for different use-cases has been increased considerably.

Inputs are done by writing C++ classes which inherit from abstract base classes provided by the Geant4 framework. At least the following inputs are required:

- a description of the geometry which should be simulated (abstract base class: *G4VUserDetectorConstruction*)
- a list of the particles and physics processes as well as the models describing them which should be included in the simulation (*G4VUserPhysicsList*)
- a primary particle generator (*G4VUserPrimaryGeneratorAction*)

To extract results from the simulation, Geant4 uses the concept of *hits* which have to be defined by the user (by inheriting from *G4VHit*) and may contain any information which could be available in a real experiment such as energy deposition, time, position and momentum. Hits are produced in specifically assigned sensitive volumes (derived from *G4VSensitiveDetector*) only and processed or stored at the end of the event in a class derived from *G4UserEventAction*. One advantage of a simulation compared to a real experiment is that some information which is as a matter of principle unavailable in a detector can be extracted, such as causal connections between parent and child particles or which physics process actually took place. This information has to be processed individually at each step of the particle in a class derived from *G4SteppingVerbose*.

There is no standardized data output format in Geant4. The officially favoured way is to use an AIDA (Abstract Interfaces for Data Analysis, [AIDA]) compliant histogramming program such as JAS (Java Analysis Studio) [JAS3] or Open Scientist [OPS]. Other possibilities are saving the data in ROOT files [ROOT] or in ASCII format. In the simulations used for the present work ROOT and ASCII outputs are implemented. The advantages of the ROOT files are that they are compressed and therefore take up substantially less disk space than their ASCII equivalents, and that their contents can be directly visualised using ROOT; however the disadvantage is that they are saved in certain intervals only and are not closed properly if the simulation terminates unexpectedly, which leads to a partial data loss in case of a crash of the simulation. As this tended to happen quite often during the course of the present work, primarily the ASCII output has been used in order to avoid this problem.

4. Customizing Geant4

4.1. Physics Lists

4.1.1. A Physics List for Dark Matter Searches

As discussed in chapter 3.3, there is no fixed set of physics processes which are automatically included in a Geant4 simulation. Instead, all types of particles which could appear and all physics processes which should be taken into account as well as the models describing them have to be selected by the user. There are two possibilities to do this:

- select all particles, processes and models individually in a class derived from *G4VUserPhysicsList* or
- select one of the predefined reference physics lists based on *G4VModularPhysicsList*; if none of them fits the needs of the simulation, modify it accordingly.

Background studies for Dark Matter searches depend on the use of precise physics models over a wide energy range–from the high energy muons down to the neutron recoils in the detector–which is a requirement quite different from most other use cases of Geant4. Besides, the choice of reference physics lists is quite a moving target as lists are being added, changed and removed with almost every Geant4 release. At the time when the present work was started no predefined list containing all the required physics was available, therefore a new one had to be developed. It is based on the QGSP_GN educated guess physics list provided with Geant4 6.2 [Wel04a]. The muon nuclear interaction above 1 GeV (the lowest energy for which a reasonable implementation of this process is available in Geant4—see also section 4.1.2.8) and high precision models for neutrons below 20 MeV (the highest energy for which these models are available—see also section 4.1.2.9) have been added, as well as either the Bertini or the binary cascade for protons and neutrons below 9.9 GeV (see sections 4.1.2.4 and 4.1.2.5). This combination results in the use of the physics processes listed in appendix A. Not all of them are equally important for the present work—for example, it is not expected to encounter copious amounts of the heavy baryons such as Λ, Σ, Ξ or Ω—but all of these particles are included in the QGSP_GN list by default, they may appear in the hadronic showers induced by the muons and therefore have to be included in the simulation, especially as the search for Dark Matter is a search for rare events, implying that also other rare events should be taken into account. The selection (in the following named the QGSP_GN_HP_BIC physics list) has been made in cooperation with the Geant4 collaboration [Wel04b]. It has also been adapted by the Dark Matter search experiment EDELWEISS [Hor07]. A similar list is used by the UK Dark Matter Collaboration (UKDMC) [Ara05]. The physics content of the models used in the list is described in section 4.1.2; results of a comparison with FLUKA are given in section 4.1.3.

In Geant4 version 8.2 the official physics list QGSP_BIC_HP has become available [G482]. It is almost identical to the physics list described above using the binary cascade; the only explicit differences are:

- the quark-gluon string model now includes the quasi-elastic channel (since version 8.3) to reduce the deep inelastic component in order to improve shower shapes
- the hadron elastic scattering now uses cross sections from the chiral invariant phase space (CHIPS) model, where appropriate
- the capture at rest of negatively charged particles, including muons, is described using CHIPS (since version 8.3)
- the binary cascade is also used for d, t, ^{3}He, α and ions

Photo- and electronuclear reactions as well as muon-nuclear reactions can be switched on for this physics list via user interface commands.[1] This list has been used in the later parts of the present work in section 5.2.

4.1.2. Physics Content of the Models

In order to motivate and explain the selection of physics processes and models used in the simulation, a description of their physics contents is given in the following sections 4.1.2.1–4.1.2.9. This description is adapted from the official Geant4 Physics Reference Manual [G4PRM].

4.1.2.1. Quark-Gluon String Model

The Quark Gluon String (QGS) models for hadrons describe the inelastic interactions of n, p, π^+, π^-, K^+, K^-, K^0_S and K^0_L and are used in this physics list in the energy range from 12 GeV to 100 TeV. In this work these particles are expected to appear in the hadronic showers which muons generate when passing through rock. The high energy interactions of the aforementioned particles are described by a string model and create an excited nucleus, the de-excitation of which is simulated with a precompound model (see section 4.1.2.3). At lower energies, interactions are described by the low energy parameterized models (see section 4.1.2.6) or a cascade model (if BERT (section 4.1.2.4) or BIC (section 4.1.2.5) is used) [RPL08].

In the ultrarelativistic energy range inelastic hadron-nucleus interactions can be considered as independent hadron-nucleon collisions, as has been shown by the Regge-Gribov

---

[1] `/physics_engine/tailor/GammaNuclear on` and `/physics_engine/tailor/MuonNuclear on`, respectively

approach [Bak76]. A meson naturally consists of a quark and an antiquark, while a baryon is treated as consisting of a quark and a diquark. Between these constituents, as well as between valence and sea quarks and between the sea quarks, in the interaction a string is stretched, which can be excited in one of two possible ways: either by diffractive string excitation, in which only momentum can be transferred and which is described by the FRITIOF model [And87]; or by parton exchange, in which the rearrangement of partons as well as momentum transfer are allowed. The string can then be fragmented iteratively into a new string and a hadron, which is created randomly at one of its endpoints, either in the ground state or in its lowest excited state.

4.1.2.2. Chiral Invariant Phase Space Model

In the present work the CHiral Invariant Phase Space (CHIPS) model is used to describe the nuclear capture of negatively charged hadrons. It describes the fragmentation of a hadronic system into hadrons on the quark level in a non-perturbative way. Hadronic interactions create a quasmon, an excited hadronic system defined by its quark content and its mass, in which asymptotically free partons are distributed homogeneously over the invariant phase space. By fusion of quark-partons (in vacuum) or exchange with a neighbouring nucleon (in nuclear matter) the quasmon can decay into a final state hadron and a residual quasmon, which again can undergo decay, leading to iterative hadronization. A quasmon cannot be heated above the critical temperature $T_c \approx 200\,\mathrm{MeV}$, which is the main parameter of this model; if more energy is added to the system, more partons are produced. A quark with energy E will be created with a probability proportional to $e^{-E/T}$, therefore the heavy quarks are suppressed in this model and only u, d, s quarks are taken into account. The CHIPS event generator was originally developed to describe final state hadronic fragmentation only, but if the initial interaction of projectiles with targets is modeled appropriately it can be used for all kinds of hadronic interaction. Together with the Geant4 String Model interface it can also be used for nuclear fragmentation at extremely high energies.

4.1.2.3. Precompound Model

The precompound model of Geant4 is used in this work to describe the deexcitation of an excited nucleus created by the quark-gluon string model (see section 4.1.2.1). It is based on the cascade-exciton model of nuclear reactions [Gud83]. In order to describe nucleon-nucleus reactions in the intermediate energy range of about 100 MeV it combines features of the lower energy exciton and the higher energy intra-nuclear cascade models. In exciton models an excited nuclear state is defined by its excitation energy and the number of excitons n, i. e. particle hole pairs. Furthermore it is assumed that only exciton-exciton scattering is contributing to the reaction, leading to the selection rule $\Delta n = 0, \pm 2$. The intra-nuclear cascade model is based on a Boltzmann equation, but cascade particles and nucleons of the target nucleus which have not yet interacted are treated as different types of particles, and collisions between particles of the same type are not taken into account. Both models assume that the interaction is weak and treat only two-particle interactions. The cascade model keeps the reaction geometry and collision kinematics but neglects residual interactions between cascade particles, while for the exciton model it is exactly the other way around, making predictions of angular distributions difficult. In the cascade-exciton model these models are therefore combined in the following way. The nuclear reaction is assumed to proceed in three stages: cascade, pre-equilibrium and equilibrium. When a particle enters a nucleus it undergoes one or more collisions, thereby producing an excited many-quasiparticle state like a "doorway state". Due to residual interactions it evolves to a more complicated one and finally forms a compound nucleus. Particles can be emitted at any stage of this process. The primary and any secondary particles are treated via the intra-nuclear cascade as long as they are not captured by or emitted from the nucleus. The number of particle hole pairs produced in this way by the nuclear cascade determines the initial state of the remaining excited nucleus which is treated by the exciton model of pre-equilibrium and equilibrium decay. The cascade stage is described by the Dubna version of the intra-nuclear cascade, the exciton model has been developed by Gudima [Gud83].

4.1.2.4. Bertini Cascade Model

The Bertini cascade model is one of several intranuclear cascade models available in Geant4. It has been tested in the present work for the inelastic scattering of protons below 9.9 GeV and neutrons between 19.9 MeV and 9.9 GeV; however in the final simulations the binary cascade model described in the next section is used instead. The intranuclear cascade has been proposed already by Serber in 1947 [Ser47]. As the de Broglie wavelength of a particle colliding with a nucleus is usually shorter than the average distance between nucleons, the interaction can be described as a collision with a nucleon inside the target nucleus. In this interaction secondaries can be produced, which can then interact with other nucleons or be absorbed. The cascade ends when all particles which can leave the nucleus have done so. The remaining excitation energy of the final nucleus is then used as input for a non-equilibrium model. To treat this collision the Bertini model solves the corresponding Boltzmann equation on average. It has been used successfully in Monte Carlo simulations since its very introduction. The implementation in Geant4 is based on a re-engineering of the INUCL code [Tit99] and includes the Bertini intra-nuclear cascade model with excitons, a pre-equilibrium model, a nucleus explosion model, a fission model, and an evaporation model. While only protons, neutrons and pions are allowed as projectiles, gammas and radioactive isotopes are also treated in the model, and all types of targets are allowed. The energy range is limited to 100 MeV–5 GeV by the condition $\lambda_B/v \ll \tau c \ll t$, with λ_B the de Broglie wavelength of the nucleons, v the average relative velocity between two nucleons and t the time interval between collisions. In the first 10^{-23}–10^{-22} seconds a highly excited nucleus is produced, which may decay by fission or pre-equilibrium emission. After 10^{-18}–10^{-16} seconds a compound nucleus phase with evaporation follows.

4.1.2.5. Binary Cascade Model

Another intranuclear cascade model is the binary cascade. It is used in the present work for the inelastic scattering of protons below 9.9 GeV and neutrons between 19.9 MeV and 9.9 GeV. Reactions are described by two particle binary collisions of primary or secondary particles and an individual nucleon of the nucleus, hence the name *binary* cascade. Cross section data—experimental data, where available—are used to select collisions; angular distributions for elastic scattering of nucleons are taken from the SAID phase-shift analysis, and final states are sampled from tables of cumulative distribution functions. The model uses cross sections for free particles; Pauli blocking is used to incorporate the influence of the Fermi statistics in the nucleus. Collective nuclear elastic interactions are approximated by a nuclear potential, in which the particles are propagated by solving the equation of motion numerically. The cascade ends when there are no particles left above the kinetic energy threshold (75 MeV), or the mean kinetic energy of the particles has dropped below another threshold (15 MeV). The remaining particles and the nucleus are then treated by an exciton-driven de-excitation model.

4.1.2.6. Parameterized Cascade Model

The parameterized models in Geant4 are based on GEANT3's GHEISHA [Fes85, Geant3] and come in two versions: the low energy models cover the range from 1 to 25 GeV projectile energy, the high energy models the range from 25 GeV to at least 10 TeV. In the present work they are used to describe the inelastic interactions of protons and neutrons between 9.5 and 25 GeV, neutron fission and capture between 19.9 MeV and 20 TeV, inelastic interactions of pions and kaons up to 25 GeV and inelastic interactions of the rare particles as listed in appendix A up to 10 TeV. Similar to the Bertini or binary cascade the parameterized models also describe hadronic interactions in terms of an intra-nuclear cascade; however only the first hadron-nucleon collision is simulated in detail, while the remaining interactions within the nucleus are simulated by generating additional hadrons, which are treated as secondaries from the initial collision. Hadron production is approximated by the formation zone concept: the interacting quark-partons require some time and therefore range to hadronize into real particles; their numbers, types and distributions are determined by functions fitted to experimental data or reproducing general trends in hadron-nucleus collisions. It is unknown in many cases how the tuning parameters of these functions relate to physical quantities, therefore the usefulness of these models is limited. As minimum bias events can be simulated with high precision, the models can however be used to make significant predictions for calorimetry.

The low energy parameterized model can be applied to the π^+, π^-, K^+, K^-, K^0 and $\overline{K^0}$ mesons, the p, n, Λ, Σ^+, Σ^-, Ξ^0, Ξ^- and Ω^- baryons and their antiparticles and the d, t and α nuclei. The mean number of hadrons is calculated as $N_m = C(s)A^{1/3}N_{ic}$ (with $C(s)$ a function of the centre of mass energy, A the atomic mass and N_{ic} the number of nucleons in the initial collision), then the total number of hadrons in the intranuclear cascade is sampled from a Poisson distribution about the mean. The combined multiplicity for all particles, the additive quantum numbers energy, charge, strangeness and baryon number in the entire phase space region as well as the reaction products from nuclear fission and evaporation are sampled from additional distribution functions. The beam energy influences the multiplicity distribution and the available phase space only.

A disadvantage of the parameterized models is the fact that they conserve energy and multiplicities of the secondaries on average only, making them unsuitable for event-by-event simulations in which every single event should be physically correct on its own, as the correlations between primary muons and resulting recoils of neutrons in the detector are lost by an average-only treatment. Unfortunately it is hard to avoid their use completely as there are no alternative models for some processes in some energy ranges; as, however, the high precision neutron models also do not guarantee energy conservation (see section 4.1.2.9), the original goal to do the simulations event-by-event could not be achieved in any case. Therefore the use of the parameterized models, although being far from optimal, is not completely detrimental to this work.

4.1.2.7. Photo-Nuclear Interaction

Photonuclear interactions taking place in the showers induced by muons are important for this work as they are the biggest single contribution to the total neutron flux [Hor07]. They can be divided into five energy regions, according to the physics processes taking place (see Fig. 4.1):

- giant dipole resonance (GDR) region from about 10 to 30 MeV: a collective excitation in which protons and neutrons oscillate in opposition. This is usually one large peak in the energy dependence of the cross section; however, in deformed nuclei, the oscillation can take place parallel and perpendicular to the symmetry axis, leading to two maxima. [Pov99]
- quasi-deuteron region from 30 MeV to the pion threshold (around 135 MeV): the photon is absorbed on a proton neutron pair (quasi-deuteron) while the rest of the nucleus watches as spectator; the cross section is small, leading to a broad, low peak
- Δ region from pion threshold to about 450 MeV: the Δ resonance ($I = \frac{3}{2}$, $J = \frac{3}{2}$) is excited. This is the dominant peak in the excitation function.
- N^* region from about 450 MeV to 1.2 GeV: among others, the $N(1440)\ P_{11}$ Roper resonance ($I = \frac{1}{2}$, $J = \frac{1}{2}$, $\Gamma \approx 300\,\mathrm{MeV}$) is excited
- Regge-Pomeron region from 1.2 GeV upwards: the cross section rises logarithmically with energy, resulting from averaging over further resonances.

In Geant4 the cross section is parameterized individually for each of these regions, based on measured absorption data of 49 nuclei at lower energies (below about 100 MeV) and 14 nuclei at higher energies.

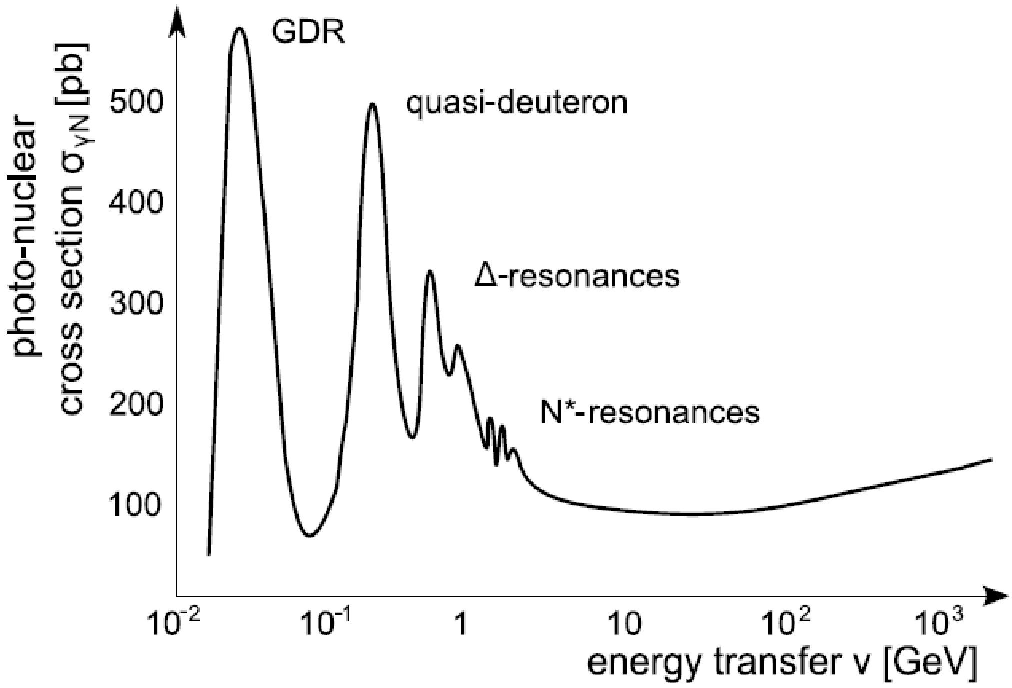

Figure 4.1.: Photonuclear cross section as a function of energy [Hor07]

4.1.2.8. Muon-Nuclear Interaction

Muon-nuclear interactions can lead to the production of hadronic showers, which are responsible for part of the neutron background in Dark Matter search experiments and therefore very important for the present work. The physics of the muon-nuclear interaction is described in section 2.2.4. Although it is comparable to the photonuclear interaction (see section 4.1.2.7), the more precise cross section parameterization based on measured data of up to 50 nuclei described in that section unfortunately is not used for muon nuclear interactions in Geant4. Also, the resonance region is neglected completely in Geant4. In the versions of Geant4 used in the present work two different models for muon-nuclear interaction are available: *G4MuonNucleusProcess* and *G4MuNuclearInteraction.*

G4MuonNucleusProcess is a reimplementation of the old GEANT3 / GHEISHA GMUNU and GMUSIG routines [Geant3]. The cross section $\sigma_{\mu A}$ for the muon photonuclear interaction is approximated very crudely:

$$\sigma_{\mu A} = A\sigma_{\mu N}$$

where A is the atomic number of the nucleus and the cross section for the interaction with a single nucleon is given by:

$$\sigma_{\mu N} \;=\; \begin{cases} 0.3 & (E \leq 30\,\mathrm{GeV}) \\ 0.3(E/30)^{0.25} & (E > 30\,\mathrm{GeV}) \end{cases} [\mu\mathrm{b}]$$

This is not only low precision but also too low by about 3 orders of magnitude [Cha04]. To produce hadronic final states the virtual photon is replaced by a pion of same Q^2 with randomly selected charge, which is then treated according to the parameterized models (see section 4.1.2.6). This automatically implies an energy threshold of about 140 MeV.

The *G4MuNuclearInteraction* describes muon deep inelastic scattering between 1 GeV and 1000 PeV muon energy. It uses the Borog and Petrushkin formula for the cross section described in section 2.2.4. It is much more precise than the parameterization used in the *G4MuonNucleusProcess* described above. The drawback is that its energy threshold is even higher (1 GeV instead of 140 MeV). Fortunately this is no big concern for the present work as muon-nuclear interaction only becomes important at much higher muon energies $E_\mu \geq 10\,\mathrm{GeV}$ [Gro01].

Due to its higher precision, only the *G4MuNuclearInteraction* has been used.

4.1.2.9. Low Energy Neutron Interactions

For low energy neutrons from thermal energies up to 20 MeV special high precision models for elastic and inelastic scattering, radiative capture and fission are available, which are based on the ENDF/B-VI evaluated data library [T2NIS]. These models are very important for the present work as neutron recoils are the most dangerous background in Dark Matter searches and therefore have to be known as precisely as possible. In order to improve performance all neutron nuclear resonances have been integrated into the data so that cross sections can be treated as point-wise. Fission is simulated up to fourth chance fission, and for inelastic interactions the following final states are taken into account: $n\gamma$, np, nd, nt, n^3He, $n\alpha$, nd2α, nt2α, $n2p$, $n2\alpha$, $np\alpha$, $n3\alpha$, $2n$, $2np$, $2n$d, $2n\alpha$, $2n2\alpha$, nX, $3n$, $3np$, $3n\alpha$, $4n$, p, pd, $p\alpha$, $2p$d, dα, d2α, dt, t, t2α, ^{3}He, α, 2α and 3α. Unfortunately, for some important chemical elements insufficient or no neutron data are available and the models cannot conserve energy on an event-by-event basis [Sch11, Wel01] or neutron interactions can even be described by the low energy parameterized models only, leading to a significant loss in accuracy. Results should therefore be taken with a grain of salt only.

4.1.3. Test of the Physics List

To check the correctness of the selection of physics processes and models and to assess the overall reliability of Geant4, test simulations using several slightly different versions of this physics list are compared to a simulation [Wul04c] written in FLUKA [Fas00], which is renowned for its high precision. FLUKA version 2003 and Geant4 version 6.2

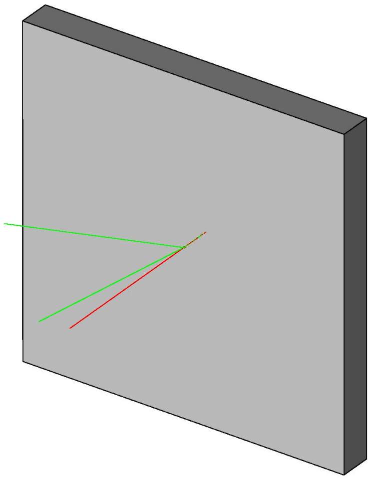

Figure 4.2.: Principle of neutron production test simulations: A muon is shot on a wide slab of material and the produced neutrons are counted. The picture shows the muon coming from behind the slab (dark/red track) and some of its secondaries (light/green track).

have been used for this comparison. Monoenergetic muons with an energy of 270 GeV, which is the mean muon energy at Gran Sasso [Amb03], are shot on wide slabs of different materials of a thickness of about 5000 g/cm^2, which is chosen such that showers are well developed but the muon doesn't lose too much energy in the material, and the produced neutrons are counted. For details of the geometry see Fig. 4.2 and Table 4.1. When counting neutrons one has to make sure that all neutrons are counted only once. Double counting can occur if scattered neutrons, for example in $(n,\, n')$ reactions, are not really scattered, but killed and created again by the simulation code, similar to the concept of "stars" in FLUKA [Fer05, Wul04c]. The behaviour of Geant4 in this respect is, in principle, unspecified [Wel04b]; however, an analysis of the source code carried out in

Material	Thickness [m]	Density [g/cm^3]	Thickness [g/cm^2]
Copper	8	8.96	7168
Lead	4	11.35	4540
LNGS concrete	12	2.3	2760
LNGS rock	12	2.71	3252
Polyethylene	40	0.96	3840

Table 4.1.: Details of the simulation geometry used for the neutron production test. The dimensions perpendicular to the muon flight direction of the slab of material are 40 m × 40 m in all cases. The particle source is centred 50 cm away from the target. For the composition of LNGS rock and concrete see Tables 4.2 and 4.3.

Element	O	Ca	C	Mg	Si	Al	K
Weight %	47.91	30.29	11.88	5.58	1.27	1.03	1.03

Table 4.2.: Elemental composition of LNGS rock [Cat86, Wul04a]. The sum of the known contributions adds up to 98.99% only and is scaled up to 100% in the simulation.

Element	O	Ca	C	Si	Al	H	Mg
Weight %	48.43	34.06	7.99	3.86	0.9	0.89	0.85
Element	Na	K	Fe	S	P	Ti	
Weight %	0.6	0.54	0.43	0.16	0.04	0.04	

Table 4.3.: Elemental composition of LNGS dry concrete (with 8% water content) [Wul04a]. The sum of the known contributions adds up to 98.79% only and is scaled up to 100% in the simulation.

the course of this work has shown that neutrons are always killed and recreated in all the models relevant to this work, leading to the maximum possible amount of double-counting. The results of the simulation have been corrected for this. The following variants of the physics list described in section 4.1.1 are used in the comparison:

1. The educated guess “QGSP_GN” physics list with the addition of muon deep inelastic scattering only
2. The same as 1., including high precision neutron models for neutrons below 20 MeV
3. The same as 2., with binary cascade for protons and neutrons below 10 GeV
4. The same as 3., but with Bertini cascade instead of binary cascade

In Geant4, 10000 muons are simulated for each of the settings. The results are given in Table 4.4.

Material	G4 (1)	G4 (2)	G4 (3)	G4 (4)	FLUKA
Copper	77.1	82.6	76.8	90.3	135.6
Lead	212.2	224.5	281.6	268.9	421.0
LNGS concrete	31.1	34.3	33.4	36.9	35.1
LNGS rock	36.0	36.2	36.9	31.4	40.4
Polyethylene	21.2	23.9	21.6	21.1	26.1

Table 4.4.: Neutron production rates by 270 GeV muons in units of $10^{-5}\, n/\mu/(\mathrm{g} \cdot \mathrm{cm}^2)$ for different variants of the Geant4 physics list described in section 4.1.1 and FLUKA “precision” simulations [Bau04]. G4 (1) is the QGSP_GN physics list only, G4 (2) is QGSP_GN and NHP, G4 (3) is QGSP_GN, NHP and BIC, and G4 (4) is QGSP_GN, NHP and BERT.

Material	FLUKA (1)	FLUKA (2)	G4 (1)	G4 standard
Copper	131.94	135.64	80.2	76.8
Lead	424.16	421.0	291.02	281.6
LNGS concrete	36.82	35.07	30.64	33.4
LNGS rock	37.45	40.44	31.38	36.9
Polyethylene	26.11	26.11	20.63	21.6

Table 4.5.: Influence of tracking cut value on simulation results of neutron production rates by 270 GeV muons in units of $10^{-5}\, n/\mu/(\mathrm{g} \cdot \mathrm{cm}^2)$. The FLUKA results are obtained with "NEW-DEFAults" (1) and "PRECISIOn" (2) settings. [Wul04c] In the "NEW-DEFA" case the cut value for γ has been set to 100 keV and for e^- and e^+ to 1 MeV; for all other particles it is fixed to 10 MeV. The Geant4 simulation uses the standard production threshold of the QGSP_GN_HP_BIC physics list of 0.7 mm (see Table 3.1 for a conversion to energy). To obtain a "NEW-DEFA"-like result in Geant4 (1) particles are killed as soon as their energy falls below the corresponding FLUKA cut value. The differences between the two settings are quite small in both simulation codes, the largest being for rock with 8% in FLUKA and 17.5% in Geant4.

When comparing Geant4 and FLUKA the fact that cuts are handled differently in these two codes has to be taken into account. FLUKA uses the traditional tracking cut in energy, while Geant4 employs a production threshold in range (see section 3.2). In FLUKA, the remaining energy of a muon or charged hadron below the cut value—which is 100 MeV by default—is distributed homogeneously over the remaining expected path length [Fer05]. The FLUKA results presented here have been obtained with the "precision" settings, in which the cut value is 100 keV for all particle types except for antineutrons, which could not be simulated below 50 MeV in FLUKA version 2003. For a description of the parameters and physics content of these settings see [Fer05]. In Geant4 the standard production threshold of the QGSP_GN physics list of 0.7 mm is used; the material-dependent corresponding energy values are given in Table 3.1. These thresholds are quite different from the FLUKA "precision" cut values and closer to the FLUKA "NEW-DEFA" settings, where the transport threshold is fixed to 10 MeV for all particles except for electrons, positrons and gammas for which it has to be set by the user and has been set to 100 keV for photons and 1 MeV for electrons and positrons in [Wul04c]. However, switching between these two settings in the comparison simulations in FLUKA changes the results at most by 8%, as shown in Table 4.5. For testing purposes the FLUKA "NEW-DEFAult" like cut has also been imitated in Geant4 using the QGSP_GN_HP_BIC physics list by killing all particles as soon as they fall below the corresponding energy values instead of tracking them further (however, their energy is not deposited there but just lost); also in this case the results change at most by 17.5% compared to the version using the standard production threshold.

Results obtained with different versions of the Geant4 physics list agree within about 25%, and Geant4 results are consistent within a factor of two with FLUKA results, with a much higher degree of agreement for most materials. Similar results have also been obtained by the UK Dark Matter collaboration [Ara05]. The conclusion is that Geant4, with a proper selection of physics processes and models, can be used for the simulation of muon-induced neutron background, with results reliable within a factor of two. In the custom physics list used in this work BIC is preferred over BERT as BIC is supposed to deliver more precise results [Wel04a].

4.2. Generators

The task of a muon generator is to provide the primary muons which are then propagated through the simulation. For the simulation to be realistic the spectrum of the muons should follow the actual spectrum at the experimental site. In reality muons can come from all directions and they either have to do this also in the simulation or provisions have to be taken to emulate this effect. Therefore, if the generator shoots muons onto the detector from one side only, its starting area has to be significantly larger than the detector to also include muons coming from large angles. This is especially important if also the rock surrounding the experimental hall should be included in the simulation and therefore has to be illuminated by the generator.

In the present work three different muon generators are used: a simple monoenergetic, monodirectional muon generator using the mean muon energy at the Gran Sasso laboratory and generators using the muon spectrum inside the Gran Sasso and Frejus underground laboratories. They are described in the following subsections.

4.2.1. Monoenergetic (Mean Muon Energy) Generator

The mean depth of the Gran Sasso laboratory is 3650 m w.e. corresponding to a mean muon energy of 270 GeV [Amb03]. Muons with this energy are shot from a single point in space about 50 cm away from the surface of the target, aiming at the centre of the target, i. e. there is no randomization in muon energy, starting point or starting momentum direction. The charge of the muon is randomly selected according to the charge ratio in cosmic ray muons of $N_{\mu^+}/N_{\mu^-} = 1.3$ [Vul98]. All differences between the fates of individual muons can therefore be attributed to the physics processes they undergo. This generator is especially easy to implement and understand and mainly useful for testing purposes. In the present work it has been used for the comparison of Geant4 and FLUKA results described in section 4.1.3.

4.2.2. Gran Sasso Generator

The muon spectrum in the Gran Sasso laboratory has been measured by the MACRO [Ahl93, Amb95] and LVD [Agl95] experiments. MACRO (Monopole, Astrophysics and Cosmic Ray Observatory) is an experiment dedicated mainly to the search for heavy

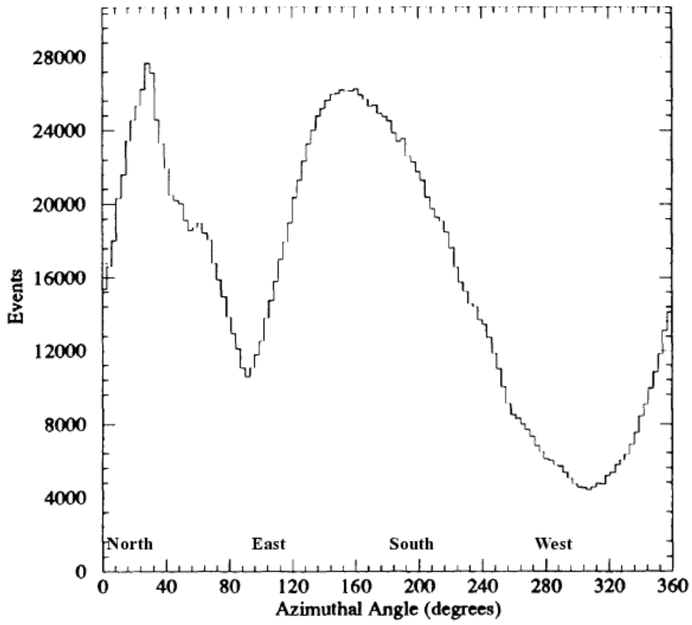

Figure 4.3.: Azimuthal angle distribution of muons in the Gran Sasso underground laboratory as measured in MACRO [Ahl93]

magnetic monopoles [Amb02]. It was operating from 1988 to 2000 in Hall B of the LNGS laboratory. LVD (Large Volume Detector) is a large liquid scintillator detector with a mass of about 1000 tonnes looking for supernova neutrinos [Alb86]. It is running since 1992 in Hall A of the LNGS, the same hall as CRESST and GERDA. The azimuthal and cosine zenith angle distributions measured by MACRO are shown in Figs. 4.3 and 4.4. The LVD experiment gives the muon intensity as a function of slant depth only. The slant depth is the actual distance the particle travels through the rock depending on the angle of its flight path, to be distinguished from the vertical depth which is the thickness of the rock measured vertically. It is found that for slant depths larger than 14000 hg/cm^2 of standard rock neutrino-induced muons dominate the spectrum.

The generator used in the present work is taken from the MaGe framework [Cha08], a simulation framework jointly developed by the Majorana and GERDA collaborations looking for neutrinoless double beta decay. The muon energy spectrum follows the parameterization of [Lip91], the angular distribution is based on the MACRO measurements from [Ahl93]. The starting positions of the muons are distributed uniformly on a horizontal circle positioned above the detector (see Fig. 4.5). μ^+ and μ^- are produced with equal probability. The generator covers an energy range from 1 GeV to 10 TeV, which contains 99.4% of the total Gran Sasso muon flux.

This generator has been used for the simulation of the generic shieldings described in chapter 5.1, some of which were also used for the GERDA double beta decay experiment

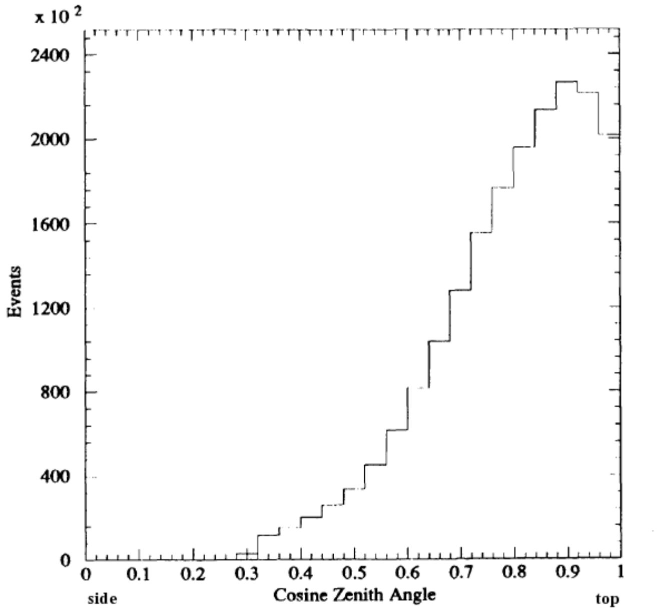

Figure 4.4.: Cosine zenith angle distribution of muons in the Gran Sasso underground laboratory as measured in MACRO [Ahl93]

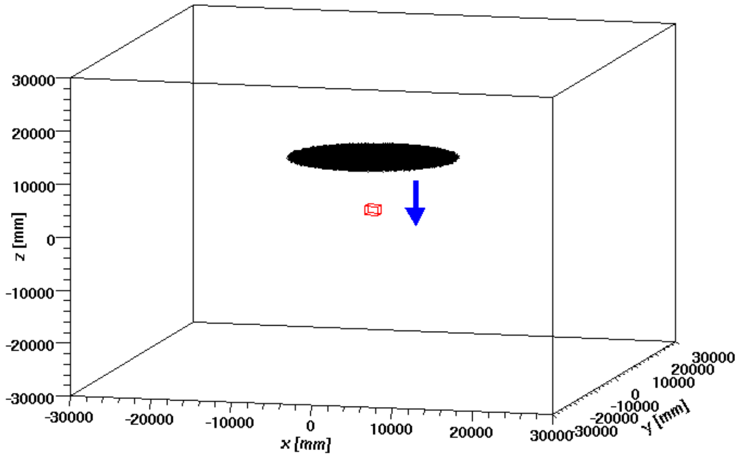

Figure 4.5.: Starting points of muons for the Gran Sasso muon generator. In this picture the radius of the generator is set to 9.9 m and its centre is located 9.9 m above the centre of the detector, which has 1.6 m edge length (shown in red). These settings are used in the determination of the optimum thickness of shielding materials in chapter 5.1.3. The blue arrow indicates the main muon flight direction.

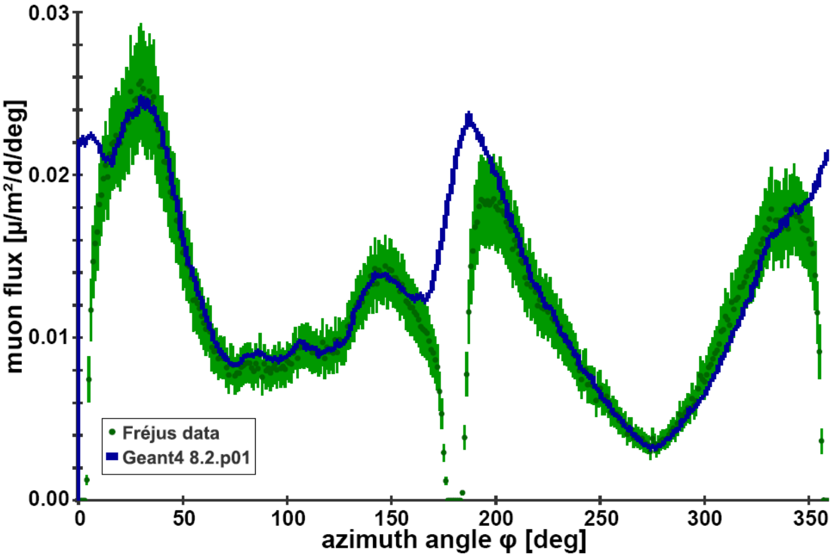

Figure 4.6.: Azimuthal muon distribution in the Frejus underground laboratory as measured by the Frejus experiment and as produced by the Monte Carlo muon generator from [Hor07]

located at Gran Sasso [Abt04]. Also, at the time these simulations were carried out the location of the future Dark Matter experiment EURECA which is now planned to be located in the future extension of the Frejus laboratory had not been fixed yet and the Gran Sasso laboratory was also taken into consideration. EURECA is described in more detail in section 5.2.1.

4.2.3. Frejus Generator

The muon spectrum in the Frejus laboratory has been measured by the Frejus collaboration [Ber89]. Its azimuthal and zenithal angular distributions are shown in Figs. 4.6 and 4.7. The shape of the azimuthal angular distribution is strongly influenced by the geography of the overlying mountains. These plots also show the implementation of this spectrum in the Monte Carlo muon generator, which was developed by M. Horn during his PhD thesis [Hor07] for the simulation of the EDELWEISS experiment. In this generator the angular distribution of muons is reproduced by using a measured elevation map of the mountains [Wei93]. Measurement and simulation are in good agreement; the clearly visible differences in Fig. 4.6 originate from the fact that the detector has two blind angles.

The technical implementation of this generator differs quite substantially from the one of the Gran Sasso generator described in the previous chapter. Muons are shot from a hemisphere to the centre of the detector (see Fig. 4.8). The starting points of the

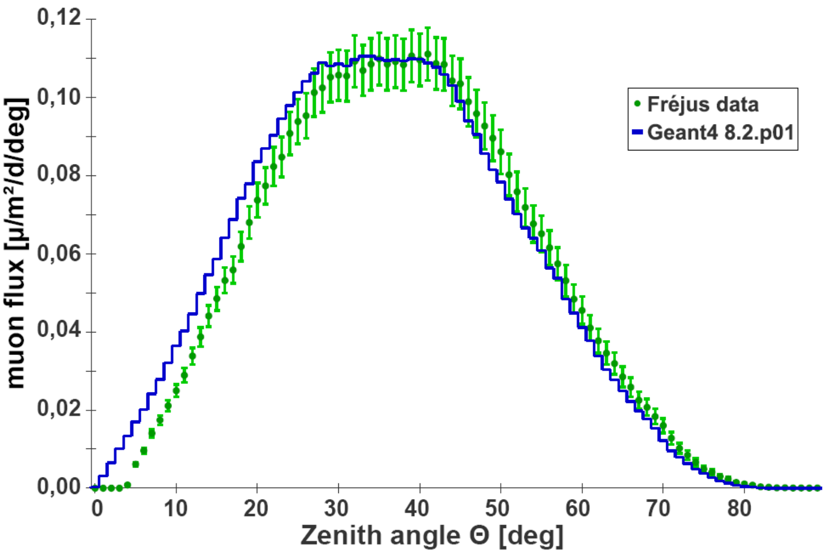

Figure 4.7.: Zenithal muon distribution in the Frejus underground laboratory as measured by the Frejus experiment and as produced by the Monte Carlo muon generator from [Hor07]

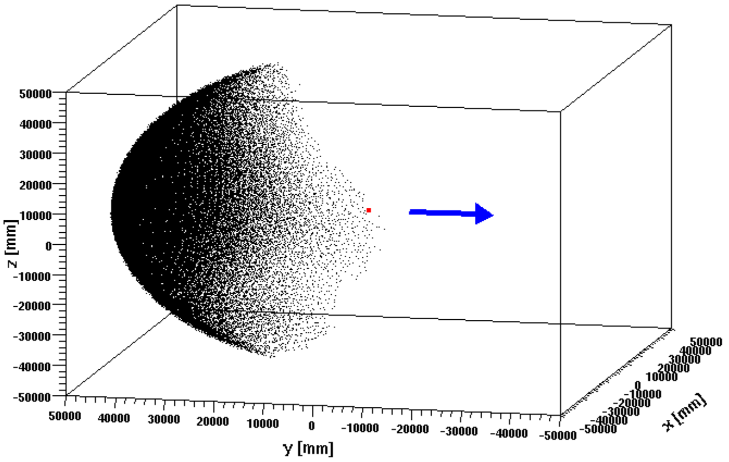

Figure 4.8.: Starting points of muons for the Frejus muon generator. In this picture the hemisphere radius of the generator is set to 50 m and the smearing radius to 15 m. The detector (shown in red) has 60 cm edge lenght. These values are used for the EURECA simulations in section 5.2. The blue arrow indicates the main muon flight direction.

muons on the hemisphere are determined according to their angular distribution, then their actual starting positions are smeared out on a circle centred around that point in order to illuminate the whole detector setup evenly. The radii of the hemisphere and the smearing circle can be set in a macro file. The standard values of these parameters as used for the simulation of EDELWEISS are 30 m for the hemisphere radius and 5 m for the smearing radius. As EURECA will be a much larger experiment, the values have been increased to 50 m hemisphere radius and 15 m smearing radius in the present work. As this generator aims all muons directly at the detector, simulation time is reduced significantly compared to the conventional method of starting the muons on a plane above the experimental hall, in which most of the muons actually miss the setup. However, the disadvantage is that the normalization to the actual running time of the experiment is more complicated; for details see section 4.2.4. The generator does not take into account the muon charge distribution but uses the muon charge selected in the source code; in the present work, only negative muons are shot. The energy range of the generator can be set via a macro file. In the present work the energy range from 20 GeV to 2000 GeV has been used which corresponds to 87% of the total flux [Hor07]. This range has been selected by taking into account the combined effects of the muon flux falling and the neutron production yield per muon rising with energy: Energies below 20 GeV have not been taken into account since at these low energies the neutron production yield per muon is low. For energies above 2 TeV, on the other hand, the muon flux is low, therefore the neutron production is suppressed by an order of magnitude.

This generator has been used to study the different possible shielding designs for EURECA (see chapter 5.2).

4.2.4. Conversion of Simulation Results to Experimental Live Time

In a Monte Carlo simulation the physical reactions of a defined number of primary particles, e. g. 1 million muons, are simulated. Therefore the results are obtained as a function of the number of primary muons, e. g. x neutrons are created per million muons. To get physically meaningful results such as the number of neutrons per year these numbers have to be converted to a function of time. For this purpose the number of muons per m^2 shot in the simulation and the muon flux in the laboratory have to be known. The muon flux in the LNGS is 1.1 $\mu/(\mathrm{m}^2 \cdot \mathrm{h})$; in the LSM it is 0.2 $\mu/(\mathrm{m}^2 \cdot \mathrm{h})$ [Mei06]. In the Gran Sasso generator the muons are shot from a horizontal circle and their angular distribution does not depend on their starting point within that circle, therefore the number of muons per m^2 can be calculated directly from the primary muons. The Frejus generator shoots the muons from a hemisphere, therefore the number of muons per m^2 has to be determined by counting the number of muons passing through a plane at the level of the experiment. This has to be done in dedicated Monte Carlo simulations of muon propagation in an empty setup. A result of such a simulation is shown in Fig. 4.9. The picture shows the number of muons per m^2 at the level of the experiment for a simulation with one million primary muons, as produced by the Frejus generator with a hemisphere radius of 50 m and a smearing radius of 15 m. In the central area the distribution of muons is homoge-

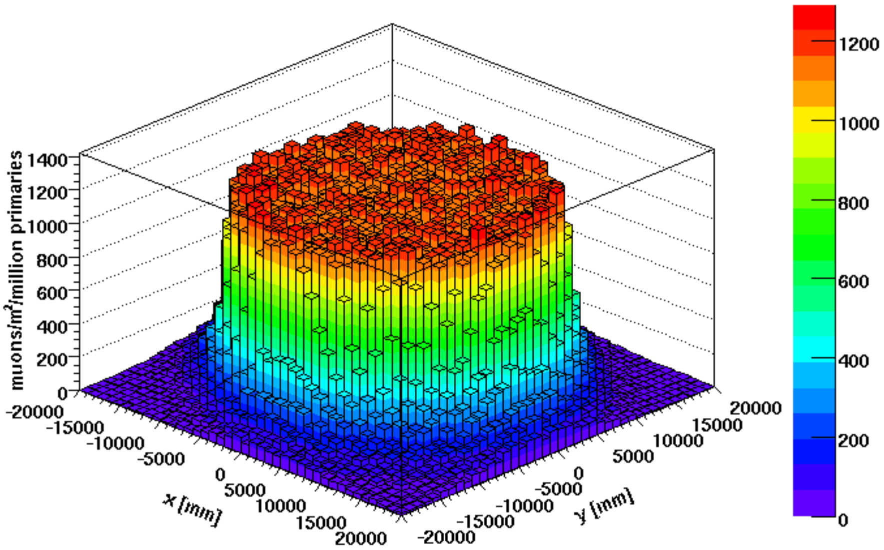

Figure 4.9.: Number of muons per m^2 at the level of the experiment, as produced by the Frejus generator with a hemisphere radius of 50 m and a smearing radius of 15 m. With these settings the muon distribution is flat in an area of more than 400 m^2 around the centre, meaning that the whole detector setup including some of the surrounding rock is illuminated evenly so that neutron production takes place in all regions of space relevant to the experiment. In the Frejus laboratory with its mean muon flux of 0.2 $\mu/(\mathrm{m}^2 \cdot \mathrm{h})$ the mean value of 1144.68 μ/m^2 corresponds to a live time of the experiment of 274.11 days for one million simulated primary muons.

neous; the whole experimental setup, including some rock, is illuminated evenly. This is important in order to ensure the production of neutrons in all regions of space from which they can make it into the detector and contribute to the background of the experiment. The average value in the central region is 1144.68 μ/m^2 on a rectangle with an area of $20\,\text{m} \times 20\,\text{m}$. The mean muon flux in the Frejus laboratory is 0.2 $\mu/(\text{m}^2 \cdot \text{h})$. Using the selected energy range of 20–2000 GeV (see chapter 4.2.3), the generator covers 87 % of the total muon flux, i.e. 0.174 $\mu/(\text{m}^2 \cdot \text{h})$, and the results have to be scaled accordingly. This leads to a slight overestimation of the neutron production as most of the "missing" flux is at lower energies,[2] at which the neutron yield is lower. This is actually good as it gives a conservative estimate of the background. One million simulated primary muons therefore correspond to a live time of the experiment of 274.11 days. Originally the hemisphere radius of this generator had been 30 m and the smearing radius 5 m. With these values one million muons correspond to an average of 10245.71 μ/m^2 for the central rectangle with an area of $8\,\text{m} \times 6\,\text{m}$ or a time of 2453.47 d $\approx$ 6.7 a.

Using the Gran Sasso generator with 9.9 m radius the average value is 3247.73 μ/m^2 for one million primary muons, corresponding to an experimental live time of 136.14 d in the Gran Sasso laboratory with its muon flux of 1.1 $\mu/(\text{m}^2 \cdot \text{h})$, 99.4% of which is covered by the generator.

---

[2] $E < 20\,\text{GeV}$: 12%, $20\,\text{GeV} < E < 200\,\text{GeV}$: 52%, $200\,\text{GeV} < E < 2\,\text{TeV}$: 35%, $E > 2\,\text{TeV}$: 1% of the total flux [Hor07]

5. Results

To obtain the highest possible sensitivity of a Dark Matter experiment it is not only necessary to place the experiment as deep underground as possible but also to select the type of shielding which is most effective against the remaining background of the laboratory. The shielding has to protect against low energy local radioactivity as well as neutrons and cosmic ray muons, which are typically of a higher energy. These requirements are partially contradictory; for example, a high-Z material such as lead protects well against gammas, but is a target for muons which can produce additional neutrons by spallation and thereby it may actually increase the relevant background. Therefore it could be a good idea to avoid the use of high-Z material as much as possible, but then the thickness of the shielding would have to be increased in order for it to still be effective against radioactivity. The subject of this work is to assess different shielding options with respect to muon-induced background. This is carried out in two parts: First, several conventional and less conventional general shielding designs are compared and the optimum thickness of the shielding materials is determined. This is done in a "toy geometry" consisting of concentric cubes of different materials using the Gran Sasso muon spectrum. The advantages of using a toy geometry instead of a full-fledged detailed geometry are that the main features of the different types of shielding stand out uninfluenced by technical details of their implementations, and that the materials and their sizes can easily be varied without the need for additional programming. The usefulness of this approach is demonstrated by comparison with a simulation using the "real" GERDA geometry and by comparing results obtained with the Frejus and Gran Sasso muon generators. Second, the different shielding designs initially proposed for the EURECA experiment are compared in order to decide how to build the experiment, and the actual decision is based on these results.

5.1. Generic Shielding Design Studies

5.1.1. Overview of Shielding Designs

5.1.1.1. Conventional Shielding Design

The conventional shielding consists of lead or copper, which is used to protect against γ particles, and polyethylene, which is used to protect against neutrons (see Fig. 5.1). The polyethylene (PE) can be located inside (*internal PE*) or outside (*external PE*) the lead or both. In the past, often only external polyethylene has been used. In this case, a muon

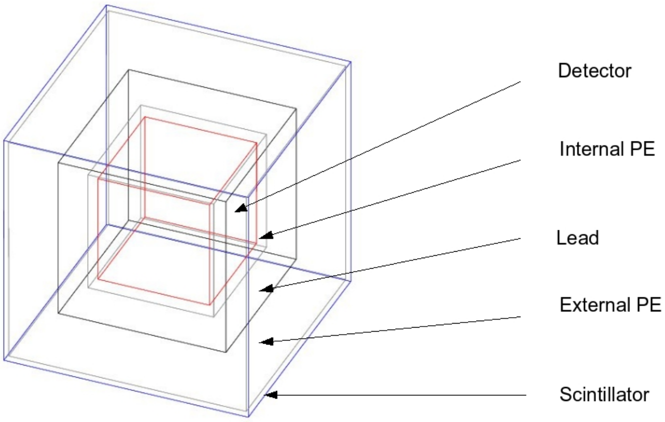

Figure 5.1.: Conventional shielding design with lead and polyethylene

veto (e. g. a thin layer of plastic scintillator around the shielding) is absolutely required as cosmic ray muons can produce neutrons in the lead which can easily enter the detector and therefore have to be vetoed. The advantage of having also internal polyethylene is that it moderates these neutrons; however, the amount of lead required is considerably increased due to the larger dimensions of the material which has to fit inside, which significantly increases the cost of the shielding as well as the neutron production rate, which might even cancel the advantages of the inner PE shielding.

5.1.1.2. Shielding Designs Avoiding the Use of High-Z Materials

The main drawback of the conventional shielding design is the use of a large amount of high-Z material which acts as a target for high energy muons. Thereby it actually *increases* the neutron background, which then has to be disposed of by additional low-Z material shielding. Of course it would be better if this additional neutron background would not even be produced in the first place. This could be achieved by replacing the high-Z material by a larger amount of lighter material, e. g. by thick polyethylene or by about 3–5 m of water. Given this thickness the water is also thick enough to act as a neutron moderator and a muon Cerenkov veto, therefore no additional polyethylene or plastic scintillator is necessary and the shielding consists *only* of water, see Fig. 5.2. This shielding is quite cheap and radiopure; however, the access to the detectors is not so easy as all the water has to be pumped out and afterwards pumped back in again, which requires an additional large storage tank with the capacity of the shielding; also,

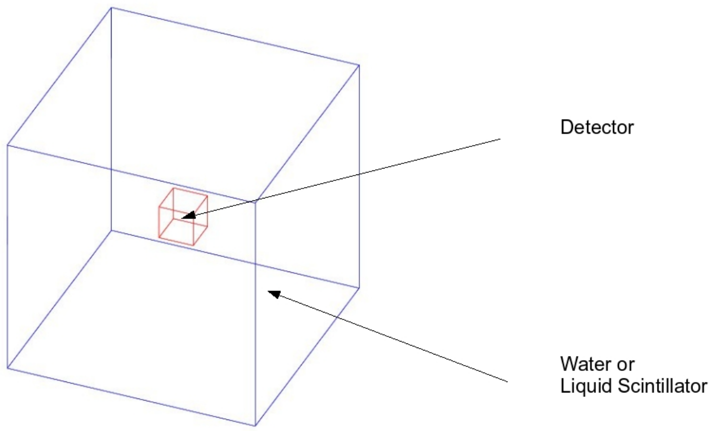

Figure 5.2.: Low-Z shielding consisting only of water or liquid scintillator

precautions have to be taken to keep the water as well as its vessel radiopure. It is also conceivable to replace the water by liquid scintillator, which will increase the light output by about three orders of magnitude, so that it might even be possible to detect the neutrons coming from the outside into the experimental setup. However it will also be about 1000 times as expensive and is therefore unfortunately highly unlikely to be implemented.

5.1.1.3. Shielding Design Deliberately Using High-Z Materials

Another option is to deliberately make use of the fact that a shielding typically contains a large amount of high-Z material and use it to detect high energy neutrons coming from outside. This can be done by building an iron–scintillator sandwich (see Fig. 5.3): the neutrons interact in the iron and these interactions are detected in the scintillator. The disadvantage of this approach is the large amount of high-Z material required and the rather high cost associated with it.

5.1.2. Simulation Results

The following shielding design variants are simulated:

1. *10PE-30Pb-50PE:* Conventional shielding design consisting of 10 cm internal polyethylene (PE), 30 cm lead and 50 cm external PE

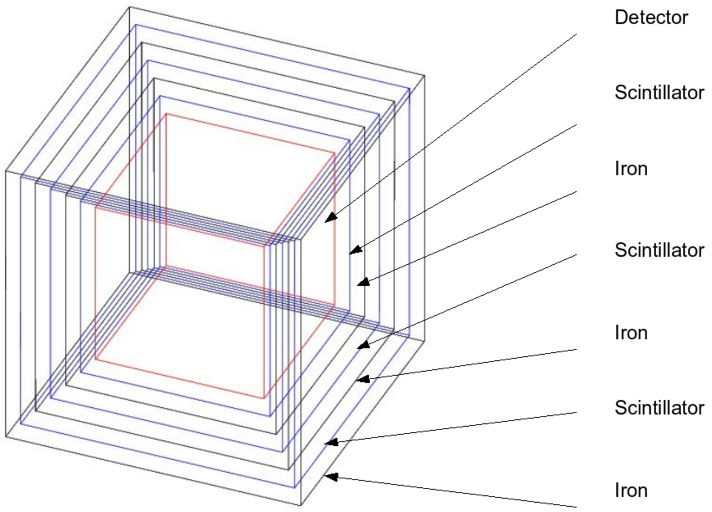

Figure 5.3.: Iron–Scintillator sandwich detector

2. *30Pb-50PE:* Conventional shielding design containing no internal PE but consisting of 30 cm lead and 50 cm external PE
3. *50PE-30Pb:* "Inverted" conventional shielding design consisting of 50 cm internal PE and 30 cm lead but no external PE
4. Variants of the above with 30 cm lead and 60 cm PE distributed differently between internal and external PE:
    a) *0PE-30Pb-60PE:* no internal but 60 cm external PE
    b) *20PE-30Pb-40PE:* 20 cm internal and 40 cm external PE
    c) *30PE-30Pb-30PE:* 30 cm internal and 30 cm external PE
    d) *60PE-30Pb-0PE:* 60 cm internal but no external PE
5. *H2O:* Low-Z shielding design consisting of 5 m water
6. *SCINT:* Low-Z shielding design consisting of 5 m liquid scintillator
7. *SANDWICH:* High-Z shielding design consisting of 3 pairs of alternating layers of 10 cm iron and 10 cm liquid scintillator, with liquid scintillator as the innermost layer around the detector.

There are two versions of most of the simulations: one in which the setup is placed just in air, and one in which the concrete and rock of the experimental hall is taken into account. Their compositions are given in Tables 4.2 and 4.3. The interior of the

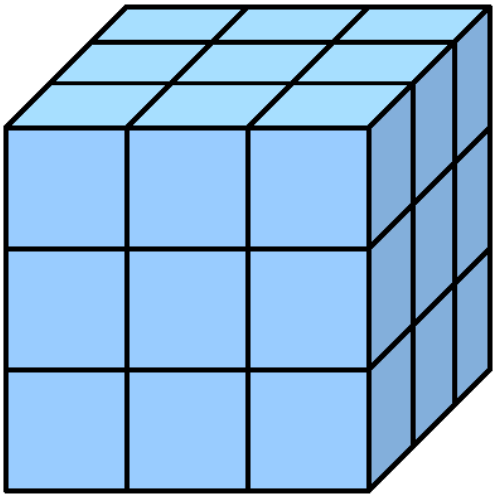

Figure 5.4.: Principle of detector segmentation: the detector is simulated as one large block of material in Geant4, but during analysis of the results the events taking place in the different segments are treated separately

shielding has an edge length of 1.6 m, which corresponds to a volume of about 4 m^3 and therefore matches the space requirements expected for the EURECA cryostats. In the simulation this volume is filled completely with enriched germanium acting as a detector in order to be sensitive to any background penetrating the shielding. In reality there will naturally be several separate detectors inside this volume between which coincidences can be evaluated to discriminate WIMPs (which will scatter only once) from neutrons (which may scatter multiple times); this is taken into account by segmenting the detector into $3 \times 3 \times 3$ segments during analysis (see Fig. 5.4). The conventional shieldings (nr. 1–4 above) are surrounded by a plastic scintillator of 5 cm thickness positioned directly around the outermost layer of shielding as a muon veto. In the simulations which include the experimental hall the thickness of the concrete is 40 cm and the thickness of the rock is 2 m. The muons are generated according to the energy and angular distribution inside the LNGS (see chapter 4.2.2). The radius of the generator is set to 20 m in all cases, its height (measured from the centre of the detector) is adapted to the size of the experimental setup: 2 m for the conventional and sandwich shieldings, 6 m for the water and liquid scintillator shieldings and 10 m for all simulations taking concrete and rock into account. This leads to the following conversion to real time for one million muons each (for details see chapter 4.2.4): 33.47 d for 2 m height, 33.16 d for 6 m height and 32.91 d for 10 m height. The simulation is carried out using GEANT4 version 7.1 with the physics list described in section 4.1.1.

The number we are interested in getting from the simulation is the background in units of counts/(kg·day) or counts/(tonne·year). It is extracted for different types of background with different cuts:

1. Background induced by all kinds of particles
    a) *seen in detector:* These are all events in which energy is deposited in the detector, regardless of the type and energy of the particle which made the deposition. Only a minimum total energy deposition of 10 keV in the detector is required corresponding to the expected nuclear recoil energy of a WIMP.
    b) *in detector but nothing in veto:* These are all events in which at least 10 keV of energy is deposited in the detector, but the amount of energy deposited in the veto is below the respective veto threshold.
    c) *in only one segment:* These are all events in which energy is deposited in only one segment of the detector with a minimum energy deposition of 10 keV.
    d) *in one segment but nothing in veto:* These are all events in which energy is deposited in only one segment of the detector with a minimum energy deposition of 10 keV, but the amount of energy deposited in the veto is below the respective veto threshold.
2. Background induced by hadronic particles
    a) *hadronics seen in detector:* These are all events in which energy is deposited in the detector by “hadronic” particles, the definition of “hadronic” being that any particle which is not an electron, positron, muon or gamma is regarded as “hadronic”. These particles are expected to produce nuclear recoils in the detector which look like a WIMP signal. An energy deposition of 10 keV is required. In this and the following three cases it is not taken into account whether there is also an “electromagnetic” energy deposition in the same event. For events containing a “hadronic” deposition *only*, see below.
    b) *hadronics in detector but nothing in veto:* These are all events in which at least 10 keV of “hadronic” energy is deposited in the detector, but the total amount of energy deposited in the veto is below the respective veto threshold.
    c) *hadronics in detector in only one segment:* These are all events in which at least 10 keV of “hadronic” energy is deposited in only one segment of the detector.
    d) *hadronics in only one segment but nothing in veto:* These are all events in which at least 10 keV of “hadronic” energy is deposited in only one segment of the detector, but the total amount of energy deposited in the veto is below the respective veto threshold.
3. Background induced by hadronic particles *only*
    a) *only hadronics in detector:* These are all events in which at least 10 keV of “hadronic” energy is deposited in the detector, but the amount of “electromagnetic” energy deposition (i.e. the deposition caused by electrons, positrons, muons and gammas) is below the threshold of 10 keV.

Shielding variant	seen in det	only one seg	had in det	had one seg	only had	only had one seg
1: 10PE-30Pb-50PE	$4.52 \cdot 10^{-3}$	$6.24 \cdot 10^{-4}$	$5.29 \cdot 10^{-4}$	$3.84 \cdot 10^{-5}$	$9.59 \cdot 10^{-6}$	$8.22 \cdot 10^{-6}$
2: 30Pb-50PE	$4.09 \cdot 10^{-3}$	$4.12 \cdot 10^{-4}$	$1.13 \cdot 10^{-3}$	$1.00 \cdot 10^{-4}$	$1.25 \cdot 10^{-4}$	$5.48 \cdot 10^{-5}$
3: 50PE-30Pb	$5.88 \cdot 10^{-3}$	$1.51 \cdot 10^{-3}$	$3.86 \cdot 10^{-4}$	$5.48 \cdot 10^{-6}$	–	–
4a: 0PE-30Pb-60PE	$3.95 \cdot 10^{-3}$	$4.07 \cdot 10^{-4}$	$1.05 \cdot 10^{-3}$	$1.04 \cdot 10^{-4}$	$1.21 \cdot 10^{-4}$	$5.76 \cdot 10^{-5}$
4b: 20PE-30Pb-40PE	$4.97 \cdot 10^{-3}$	$8.95 \cdot 10^{-4}$	$3.67 \cdot 10^{-4}$	$8.22 \cdot 10^{-6}$	–	–
4c: 30PE-30Pb-30PE	$5.53 \cdot 10^{-3}$	$1.25 \cdot 10^{-3}$	$4.34 \cdot 10^{-4}$	$9.59 \cdot 10^{-6}$	–	–
4d: 60PE-30Pb-0PE	$5.77 \cdot 10^{-3}$	$1.62 \cdot 10^{-3}$	$3.74 \cdot 10^{-4}$	$9.59 \cdot 10^{-6}$	–	–
5: H2O	$5.15 \cdot 10^{-3}$	$1.39 \cdot 10^{-3}$	$4.88 \cdot 10^{-4}$	$3.6 \cdot 10^{-5}$	–	–
6: SCINT	$5.59 \cdot 10^{-3}$	$1.61 \cdot 10^{-3}$	$4.47 \cdot 10^{-4}$	$2.63 \cdot 10^{-5}$	–	–
7: SANDWICH	$4.49 \cdot 10^{-3}$	$6.29 \cdot 10^{-4}$	$4.07 \cdot 10^{-4}$	$1.37 \cdot 10^{-6}$	–	–

Table 5.1.: Results of simulations of 1 million muons with different shielding designs in air, given in units of counts/(kg · days). For the definition of the shielding variants see page 66. The bars indicate that simulation of one million muons is not sufficient to produce any events in the respective category.

b) *only hadronics but nothing in veto:* These are all events in which at least 10 keV of "hadronic" energy is deposited in the detector, but the amount of "electromagnetic" energy deposition is below the threshold of 10 keV and the total amount of energy deposited in the veto is below the respective veto threshold.

c) *only hadronics in only one segment:* These are all events in which at least 10 keV of "hadronic" energy is deposited in only one segment of the detector, but the amount of "electromagnetic" energy deposition is below the threshold of 10 keV

d) *only hadronics in only one segment but nothing in veto:* These are all events in which at least 10 keV of "hadronic" energy is deposited in only one segment of the detector, but the amount of "electromagnetic" energy deposition is below the threshold of 10 keV and the total amount of energy deposited in the veto is below the respective veto threshold. These are the most dangerous events since they mimick WIMP signals but can neither be discriminated in the detector nor vetoed.

Results are given in Tables 5.1 and 5.2. With an increasing amount of internal polyethylene the total number of events *seen in the detector* increases slightly (up to 50 %) and the number of events seen *in only one segment* of the detector increases up to a factor of 3, but the dangerous *hadronics seen in detector* and the still more dangerous *hadronics in only one segment of the detector* are reduced by at least a factor of 2–3; with 20 cm internal PE or more the *hadronics in one segment* are even reduced by an order of magnitude. The alternative shielding designs specifically using low-Z or high-Z materials (variants 5–7 in the list on page 66) are comparable in effectiveness to the conventional ones with internal PE; they are not worse but also have no clear advantages, therefore

Shielding variant	seen in det	only one seg	had in det	had one seg	only had	only had one seg
1: 10PE-30Pb-50PE	$3.96 \cdot 10^{-3}$	$6.45 \cdot 10^{-4}$	$5.17 \cdot 10^{-4}$	$6.69 \cdot 10^{-5}$	$1.11 \cdot 10^{-5}$	$9.76 \cdot 10^{-6}$
2: 30Pb-50PE	$3.58 \cdot 10^{-3}$	$4.18 \cdot 10^{-4}$	$1.08 \cdot 10^{-3}$	$1.30 \cdot 10^{-4}$	$1.70 \cdot 10^{-4}$	$7.11 \cdot 10^{-5}$
3: 50PE-30Pb	$5.07 \cdot 10^{-3}$	$1.38 \cdot 10^{-3}$	$3.78 \cdot 10^{-4}$	$2.09 \cdot 10^{-5}$	–	–
4a: 0PE-30Pb-60PE	$3.59 \cdot 10^{-3}$	$3.46 \cdot 10^{-4}$	$9.85 \cdot 10^{-4}$	$1.39 \cdot 10^{-4}$	$1.62 \cdot 10^{-4}$	$8.08 \cdot 10^{-5}$
4d: 60PE-30Pb-0PE	$5.20 \cdot 10^{-3}$	$1.49 \cdot 10^{-3}$	$3.80 \cdot 10^{-4}$	$2.51 \cdot 10^{-5}$	–	–
5: H2O	$4.39 \cdot 10^{-3}$	$1.19 \cdot 10^{-3}$	$3.40 \cdot 10^{-4}$	$2.23 \cdot 10^{-5}$	$1.39 \cdot 10^{-6}$	–
6: SCINT	$4.74 \cdot 10^{-3}$	$1.45 \cdot 10^{-3}$	$3.58 \cdot 10^{-4}$	$1.67 \cdot 10^{-5}$	–	–
7: SANDWICH	$4.04 \cdot 10^{-3}$	$6.65 \cdot 10^{-4}$	$3.68 \cdot 10^{-4}$	$3.62 \cdot 10^{-5}$	$1.39 \cdot 10^{-6}$	–

Table 5.2.: Results of simulations of 1 million muons with different shielding designs, given in units of counts/(kg · days); setup with concrete and rock. For the definition of the shielding variants see page 66. The bars indicate that simulation of one million muons is not sufficient to produce any events in the respective category.

the decision between alternative and conventional shieldings can be based on practical and financial reasoning.

5.1.3. Determination of Optimum Thicknesses of Materials

In addition to the general comparison of the different shielding designs the optimum thicknesses of the lead and PE layers for the conventional type of shielding of muon-induced background are determined in a new set of simulations [Bau06]. Muons are shot according to the Gran Sasso spectrum: the height and radius of the generator are unified to 9.9 m each for all shielding variants and the Geant4 version is upgraded to 8.1. The edge length of the sensitive volume is kept at 1.6 m but its material is changed from enriched to natural germanium. The thicknesses of the internal and external PE layers and the lead are varied individually between 0 cm and 50 cm in steps of 10 cm while the other two thicknesses are kept constant. The thickness of the plastic scintillator muon veto is 5 cm in all simulations. In a first step the setup is placed in air; the muons are shot directly to the shielding. The results are shown in Figs. 5.5, 5.6 and 5.7; for numerical values see Tables 5.3, 5.4 and 5.5. As a second step the shieldings are placed inside a hall with 13 m edge length, surrounded by 50 cm of Gran Sasso concrete and 2.95 m of Gran Sasso rock; their compositions are given in Tables 4.2 and 4.3. It has been shown that most of the neutrons which make it into the hall are produced in the last few metres of rock [Dem99, Wul04b], therefore it is sufficient to take this amount of material into account. This saves a lot of computing time compared to a simulation of the passage of muons through the complete thickness of rock from the top of the mountain. The results are plotted in Figs. 5.8 and 5.9, the numerical values are given in Tables 5.6 and 5.7. As the thickness of the external polyethylene has almost no influence on the results in the setup without rock these simulations are not repeated with rock. In these

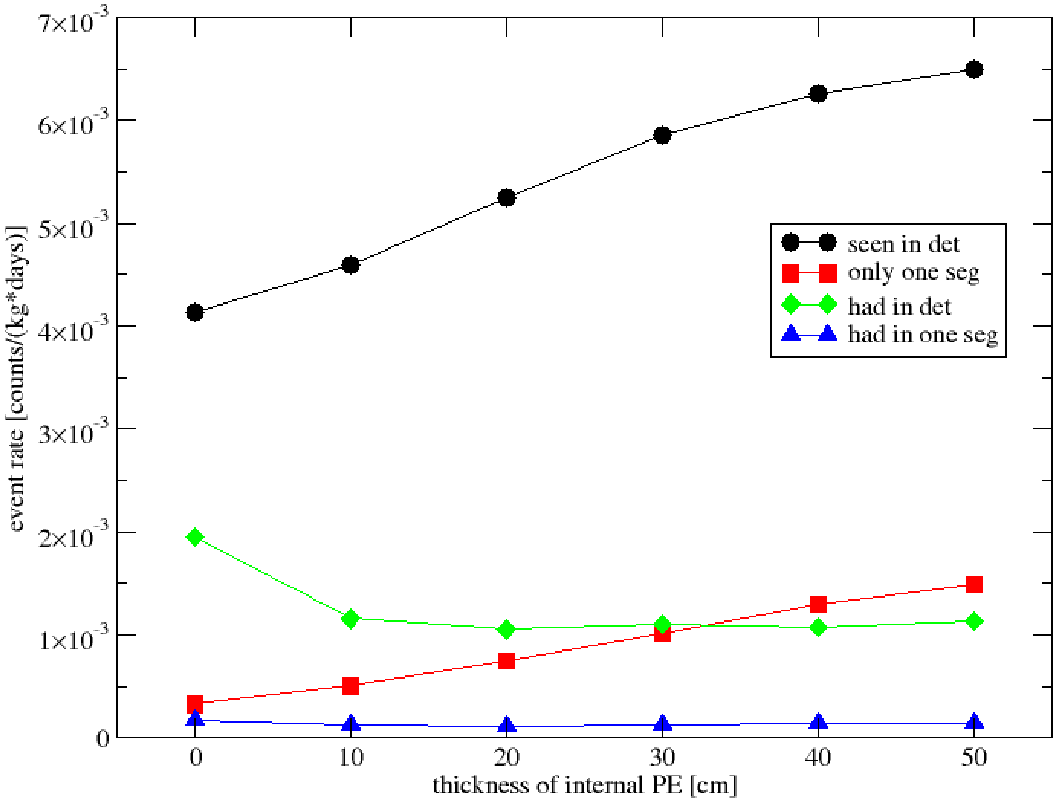

Figure 5.5.: Influence of the thickness of the internal polyethylene in a shielding with 30 cm lead and 30 cm external PE, for 1 million primary muons in air

Internal PE [cm]	seen in det	only one seg	had in det	had in one seg	only had	only had one seg
0	$4.14 \cdot 10^{-3}$	$3.25 \cdot 10^{-4}$	$1.95 \cdot 10^{-3}$	$1.70 \cdot 10^{-4}$	$1.41 \cdot 10^{-4}$	$7.14 \cdot 10^{-5}$
10	$4.60 \cdot 10^{-3}$	$5.03 \cdot 10^{-4}$	$1.16 \cdot 10^{-3}$	$1.24 \cdot 10^{-4}$	$3.37 \cdot 10^{-6}$	$3.03 \cdot 10^{-6}$
20	$5.25 \cdot 10^{-3}$	$7.47 \cdot 10^{-4}$	$1.05 \cdot 10^{-3}$	$1.08 \cdot 10^{-4}$	$1.01 \cdot 10^{-6}$	$6.47 \cdot 10^{-7}$
30	$5.85 \cdot 10^{-3}$	$1.02 \cdot 10^{-3}$	$1.11 \cdot 10^{-3}$	$1.26 \cdot 10^{-4}$	–	–
40	$6.25 \cdot 10^{-3}$	$1.30 \cdot 10^{-3}$	$1.07 \cdot 10^{-3}$	$1.38 \cdot 10^{-4}$	–	–
50	$6.50 \cdot 10^{-3}$	$1.48 \cdot 10^{-3}$	$1.14 \cdot 10^{-3}$	$1.41 \cdot 10^{-4}$	$6.74 \cdot 10^{-7}$	$6.74 \cdot 10^{-7}$

Table 5.3.: Results of simulations for different thicknesses of internal PE, all with 30 cm Pb and 30 cm external PE, for 1 million primary muons in air in units of counts/(kg · days). The bars indicate that simulation of one million muons is not sufficient to produce any events in the respective category.

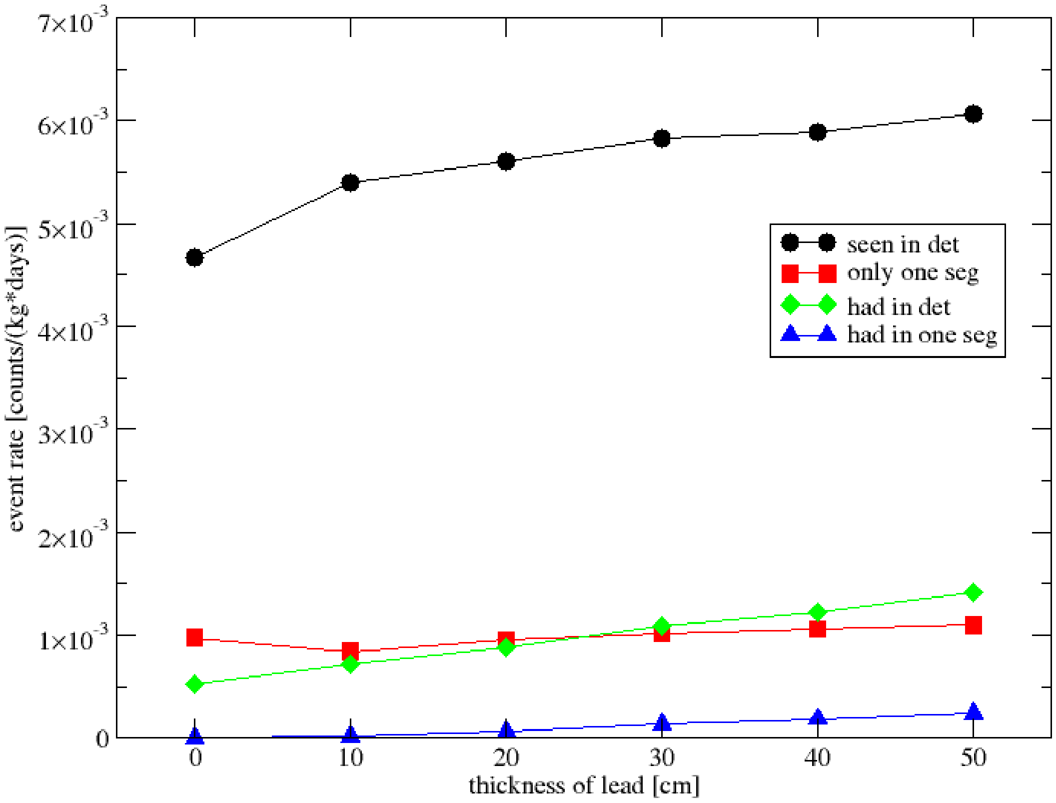

Figure 5.6.: Influence of the thickness of the lead in a shielding with 30 cm internal and 10 cm external PE, for 1 million primary muons in air

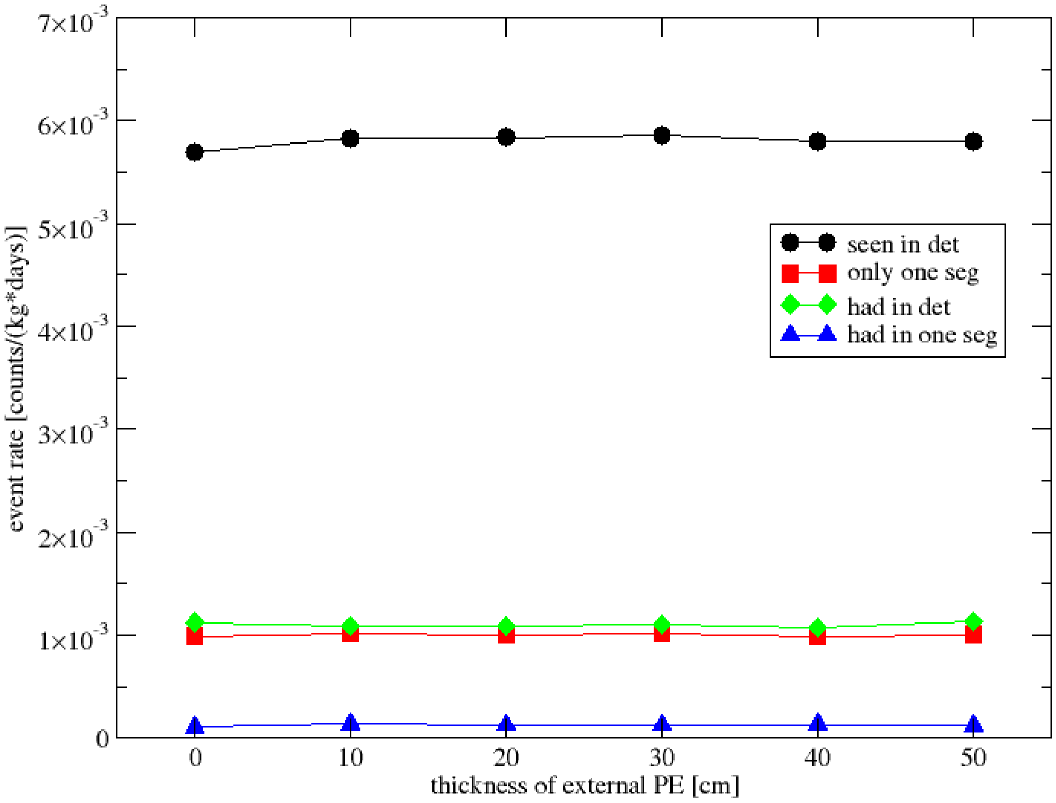

Figure 5.7.: Influence of the thickness of the external polyethylene in a shielding with 30 cm internal PE and 30 cm lead, for 1 million primary muons in air

Lead [cm]	seen in det	only one seg	had in det	had in one seg	only had	only had one seg
0	$4.66 \cdot 10^{-3}$	$9.75 \cdot 10^{-4}$	$5.23 \cdot 10^{-4}$	$3.37 \cdot 10^{-7}$	–	–
10	$5.40 \cdot 10^{-3}$	$8.42 \cdot 10^{-4}$	$7.16 \cdot 10^{-4}$	$1.28 \cdot 10^{-5}$	–	–
20	$5.60 \cdot 10^{-3}$	$9.54 \cdot 10^{-4}$	$8.74 \cdot 10^{-4}$	$6.20 \cdot 10^{-5}$	$3.37 \cdot 10^{-7}$	$3.37 \cdot 10^{-7}$
30	$5.82 \cdot 10^{-3}$	$1.01 \cdot 10^{-3}$	$1.08 \cdot 10^{-3}$	$1.30 \cdot 10^{-4}$	–	–
40	$5.89 \cdot 10^{-3}$	$1.05 \cdot 10^{-3}$	$1.22 \cdot 10^{-3}$	$1.84 \cdot 10^{-4}$	$3.37 \cdot 10^{-7}$	$3.37 \cdot 10^{-7}$
50	$6.06 \cdot 10^{-3}$	$1.10 \cdot 10^{-3}$	$1.42 \cdot 10^{-3}$	$2.39 \cdot 10^{-4}$	–	–
60	$6.35 \cdot 10^{-3}$	$1.17 \cdot 10^{-3}$	$1.57 \cdot 10^{-3}$	$2.84 \cdot 10^{-4}$	$3.37 \cdot 10^{-7}$	$3.37 \cdot 10^{-7}$
80	$6.63 \cdot 10^{-3}$	$1.35 \cdot 10^{-3}$	$1.94 \cdot 10^{-3}$	$4.52 \cdot 10^{-4}$	$3.37 \cdot 10^{-7}$	$3.37 \cdot 10^{-7}$
100	$6.92 \cdot 10^{-3}$	$1.47 \cdot 10^{-3}$	$2.23 \cdot 10^{-3}$	$5.69 \cdot 10^{-4}$	$6.74 \cdot 10^{-7}$	$6.74 \cdot 10^{-7}$
120	$7.14 \cdot 10^{-3}$	$1.59 \cdot 10^{-3}$	$2.58 \cdot 10^{-3}$	$6.97 \cdot 10^{-4}$	$1.68 \cdot 10^{-6}$	$1.68 \cdot 10^{-6}$
150	$7.62 \cdot 10^{-3}$	$1.83 \cdot 10^{-3}$	$2.95 \cdot 10^{-3}$	$8.69 \cdot 10^{-4}$	$1.01 \cdot 10^{-6}$	$6.74 \cdot 10^{-7}$
200	$8.19 \cdot 10^{-3}$	$2.07 \cdot 10^{-3}$	$3.54 \cdot 10^{-3}$	$1.12 \cdot 10^{-3}$	$1.35 \cdot 10^{-6}$	$1.35 \cdot 10^{-6}$
300	$8.82 \cdot 10^{-3}$	$2.49 \cdot 10^{-3}$	$4.18 \cdot 10^{-3}$	$1.49 \cdot 10^{-3}$	$2.02 \cdot 10^{-6}$	$2.02 \cdot 10^{-6}$
500	$9.43 \cdot 10^{-3}$	$2.93 \cdot 10^{-3}$	$4.77 \cdot 10^{-3}$	$1.85 \cdot 10^{-3}$	$1.01 \cdot 10^{-6}$	$1.01 \cdot 10^{-6}$
800	$9.62 \cdot 10^{-3}$	$3.14 \cdot 10^{-3}$	$4.95 \cdot 10^{-3}$	$2.02 \cdot 10^{-3}$	$1.76 \cdot 10^{-6}$	$1.76 \cdot 10^{-6}$

Table 5.4.: Results of simulations for different thicknesses of lead, all with 30 cm internal and 10 cm external PE, for 1 million primary muons in air in units of counts/(kg · days). The bars indicate that simulation of one million muons is not sufficient to produce any events in the respective category.

External PE [cm]	seen in det	only one seg	had in det	had in one seg	only had	only had one seg
0	$5.69 \cdot 10^{-3}$	$9.88 \cdot 10^{-4}$	$1.12 \cdot 10^{-3}$	$1.05 \cdot 10^{-4}$	$2.73 \cdot 10^{-5}$	$2.29 \cdot 10^{-5}$
10	$5.82 \cdot 10^{-3}$	$1.01 \cdot 10^{-3}$	$1.08 \cdot 10^{-3}$	$1.30 \cdot 10^{-4}$	–	–
20	$5.83 \cdot 10^{-3}$	$1.00 \cdot 10^{-3}$	$1.09 \cdot 10^{-3}$	$1.28 \cdot 10^{-4}$	$3.37 \cdot 10^{-7}$	$3.37 \cdot 10^{-7}$
30	$5.85 \cdot 10^{-3}$	$1.02 \cdot 10^{-3}$	$1.11 \cdot 10^{-3}$	$1.26 \cdot 10^{-4}$	–	–
40	$5.80 \cdot 10^{-3}$	$9.86 \cdot 10^{-4}$	$1.07 \cdot 10^{-3}$	$1.28 \cdot 10^{-4}$	$6.74 \cdot 10^{-7}$	$6.74 \cdot 10^{-7}$
50	$5.80 \cdot 10^{-3}$	$1.01 \cdot 10^{-3}$	$1.13 \cdot 10^{-3}$	$1.20 \cdot 10^{-4}$	$1.01 \cdot 10^{-6}$	$6.74 \cdot 10^{-7}$

Table 5.5.: Results of simulations for different thicknesses of external PE, all with 30 cm internal PE and 30 cm Pb, for 1 million primary muons in air in units of counts/(kg · days). The bars indicate that simulation of one million muons is not sufficient to produce any events in the respective category.

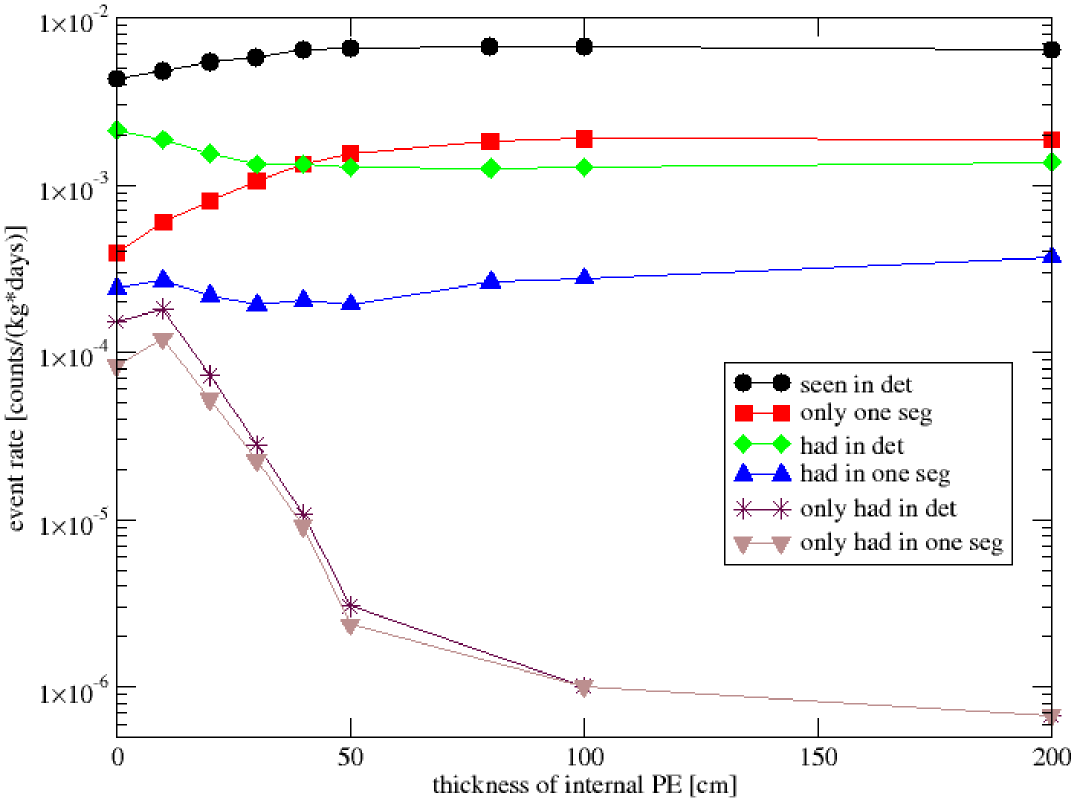

Figure 5.8.: Influence of thickness of the internal polyethylene in a shielding with 30 cm lead and 30 cm external PE, for 1 million primary muons in a setup with concrete and rock. In contrast to the other plots in this chapter this plot has a logarithmic y axis to emphasize the decrease in the number of purely hadronic events with increasing PE thickness

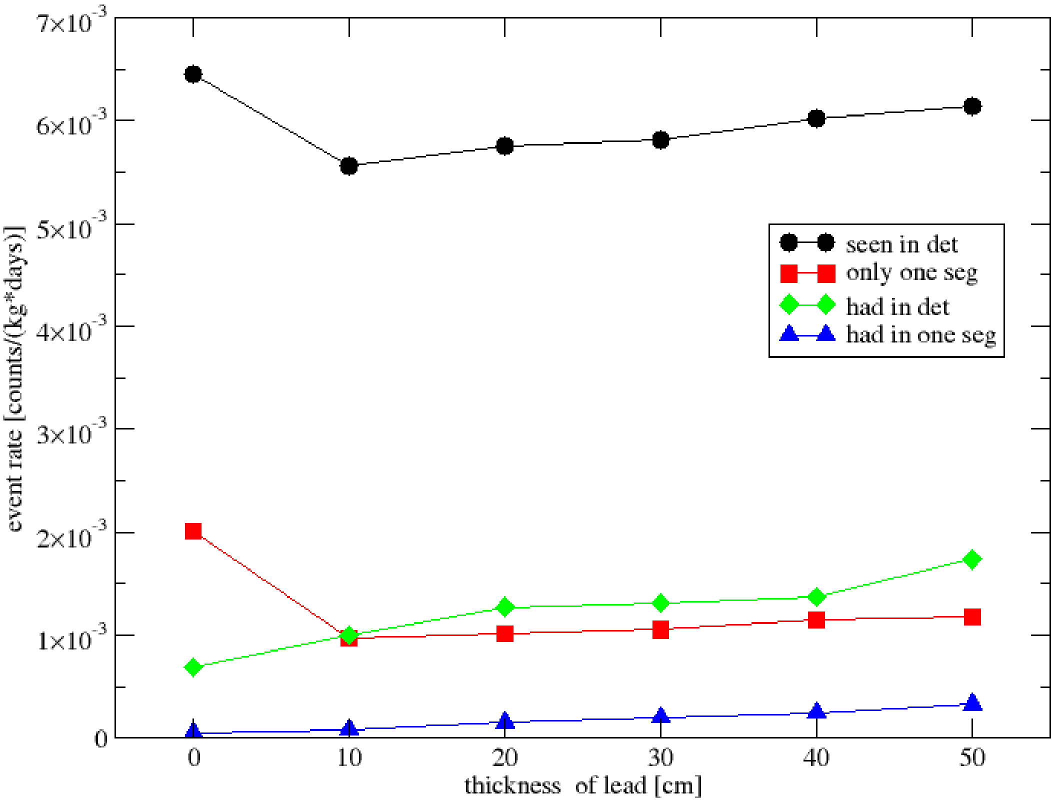

Figure 5.9.: Influence of the thickness of lead in a shielding with 30 cm internal and 30 cm external PE, for 1 million primary muons in a setup with concrete and rock

Internal PE [cm]	seen in det	only one seg	had in det	had in one seg	only had	only had one seg
0	$4.30 \cdot 10^{-3}$	$3.91 \cdot 10^{-4}$	$2.13 \cdot 10^{-3}$	$2.42 \cdot 10^{-4}$	$1.53 \cdot 10^{-4}$	$8.32 \cdot 10^{-5}$
10	$4.82 \cdot 10^{-3}$	$6.00 \cdot 10^{-4}$	$1.86 \cdot 10^{-3}$	$2.69 \cdot 10^{-4}$	$1.82 \cdot 10^{-4}$	$1.20 \cdot 10^{-4}$
20	$5.39 \cdot 10^{-3}$	$8.04 \cdot 10^{-4}$	$1.55 \cdot 10^{-3}$	$2.18 \cdot 10^{-4}$	$7.24 \cdot 10^{-5}$	$5.26 \cdot 10^{-5}$
30	$5.78 \cdot 10^{-3}$	$1.05 \cdot 10^{-3}$	$1.33 \cdot 10^{-3}$	$1.91 \cdot 10^{-4}$	$2.80 \cdot 10^{-5}$	$2.26 \cdot 10^{-5}$
40	$6.36 \cdot 10^{-3}$	$1.33 \cdot 10^{-3}$	$1.32 \cdot 10^{-3}$	$2.04 \cdot 10^{-4}$	$1.08 \cdot 10^{-5}$	$9.19 \cdot 10^{-6}$
50	$6.59 \cdot 10^{-3}$	$1.54 \cdot 10^{-3}$	$1.27 \cdot 10^{-3}$	$1.93 \cdot 10^{-4}$	$3.03 \cdot 10^{-6}$	$2.36 \cdot 10^{-6}$
80	$6.74 \cdot 10^{-3}$	$1.81 \cdot 10^{-3}$	$1.26 \cdot 10^{-3}$	$2.61 \cdot 10^{-4}$	–	–
100	$6.66 \cdot 10^{-3}$	$1.88 \cdot 10^{-3}$	$1.28 \cdot 10^{-3}$	$2.77 \cdot 10^{-4}$	$1.01 \cdot 10^{-6}$	$1.01 \cdot 10^{-6}$
200	$6.39 \cdot 10^{-3}$	$1.87 \cdot 10^{-3}$	$1.37 \cdot 10^{-3}$	$3.71 \cdot 10^{-4}$	$6.74 \cdot 10^{-7}$	$6.74 \cdot 10^{-7}$

Table 5.6.: Results of simulations for different thicknesses of internal PE, all with 30 cm Pb and 30 cm external PE, for 1 million primary muons, in units of counts/(kg · days); setup with concrete and rock. The bars indicate that simulation of one million muons is not sufficient to produce any events in the respective category.

Lead [cm]	seen in det	only one seg	had in det	had in one seg	only had	only had one seg
0	$6.45 \cdot 10^{-3}$	$2.01 \cdot 10^{-3}$	$6.88 \cdot 10^{-4}$	$5.22 \cdot 10^{-5}$	–	–
10	$5.56 \cdot 10^{-3}$	$9.68 \cdot 10^{-4}$	$1.00 \cdot 10^{-3}$	$7.78 \cdot 10^{-5}$	$1.68 \cdot 10^{-5}$	$1.08 \cdot 10^{-5}$
20	$5.75 \cdot 10^{-3}$	$1.01 \cdot 10^{-3}$	$1.27 \cdot 10^{-3}$	$1.50 \cdot 10^{-4}$	$5.93 \cdot 10^{-5}$	$4.38 \cdot 10^{-5}$
30	$5.81 \cdot 10^{-3}$	$1.05 \cdot 10^{-3}$	$1.31 \cdot 10^{-3}$	$2.00 \cdot 10^{-4}$	$2.02 \cdot 10^{-5}$	$1.58 \cdot 10^{-5}$
40	$6.02 \cdot 10^{-3}$	$1.14 \cdot 10^{-3}$	$1.37 \cdot 10^{-3}$	$2.45 \cdot 10^{-4}$	$3.37 \cdot 10^{-7}$	–
50	$6.14 \cdot 10^{-3}$	$1.18 \cdot 10^{-3}$	$1.73 \cdot 10^{-3}$	$3.25 \cdot 10^{-4}$	$4.35 \cdot 10^{-5}$	$3.44 \cdot 10^{-5}$

Table 5.7.: Results of simulations for different thicknesses of lead, all with 30 cm internal and 10 cm external PE, for 1 million primary muons, in units of counts/(kg · days); setup with concrete and rock. The bars indicate that simulation of one million muons is not sufficient to produce any events in the respective category.

simulations "hadronic" particles are always accompanied by "electromagnetic" particles and all detected events are also seen in the muon veto.

It is found that the total number of events seen in the detector increases with increasing thickness of internal polyethylene at least up to a thickness of 80 cm, from $4.30 \cdot 10^{-3}$ counts/(kg · days) with no internal polyethylene to $6.74 \cdot 10^{-3}$ counts/(kg · days) with 80 cm of internal polyethylene. On the other hand, the number of hadronic events in the detector decreases, also at least up to 80 cm; the number of hadronic events seen in only one segment of the detector decreases first but starts to rise again at 80 cm. However, most importantly, the number of the especially dangerous purely hadronic events keeps decreasing even with much larger thicknesses of internal PE, from $1.53 \cdot 10^{-4}$ counts/(kg · days) without internal PE to $2.80 \cdot 10^{-5}$ counts/(kg · days) with 30 cm of internal PE to $6.74 \cdot 10^{-7}$ counts/(kg · days) with 2 m of internal PE.

The number of hadronic events in the detector is increased by a factor of 2–3, the number of hadronic events in one segment of the detector even by an order of magnitude compared to the previous results of toy geometry simulations comparing conventional and alternative shielding designs given in section 5.1.2. Possible reasons could be the differences in the versions of Geant4, the target materials and the geometries used. This discrepancy limits the trust in the simulations and has to be taken as their uncertainty.

Concerning the lead shielding, the number of all types of events increases consistently with its thickness. However, when taking into account the presence of concrete and rock around the setup, the number of all events seen in the detector can be reduced by having at least some lead around the setup compared to a "conventional" shielding without lead. This indicates that lead increases the amount of hadronic background in the detector while decreasing the amount of electromagnetic background. Shielding of γ particles is the actual reason for having the lead in the shielding at all.

The thickness of the external polyethylene does not have a noticeable influence on the muon-induced background, except that the number of purely hadronic events seems to be reduced somewhat when at least some external polyethylene is present. External polyethylene is primarily used to shield against low energy neutrons from (α, n) reactions and fission which are not considered further in this work as it concentrates on muon-induced neutrons but which are treated in [Sch11].

The following conclusions regarding the design of conventional shieldings can be drawn from the results of the simulations with respect to the muon-induced background:

1. It is advisable to have about 20–30 cm of internal polyethylene to minimize the number of "dangerous" events.
2. Although lead is useful to reduce the amount of electromagnetic background, its thickness should be kept as small as possible.
3. The thickness of the external polyethylene has almost no influence on the results. External PE may however be useful to protect against neutrons from local radioactivity.

shielding	seen in det	only one seg	had in det	had in one seg	only had	only had one seg
100 cm PE	$5.18 \cdot 10^{-3}$	$1.28 \cdot 10^{-3}$	$5.53 \cdot 10^{-4}$	$6.74 \cdot 10^{-7}$	–	–
5 m water	$5.58 \cdot 10^{-3}$	$1.38 \cdot 10^{-3}$	$6.67 \cdot 10^{-4}$	$4.23 \cdot 10^{-5}$	$5.50 \cdot 10^{-7}$	$5.50 \cdot 10^{-7}$
5 m liq. scint.	$5.98 \cdot 10^{-3}$	$1.60 \cdot 10^{-3}$	$6.38 \cdot 10^{-4}$	$2.90 \cdot 10^{-5}$	–	–
no shielding	$3.22 \cdot 10^{-3}$	$2.68 \cdot 10^{-4}$	$4.90 \cdot 10^{-4}$	$1.01 \cdot 10^{-6}$	–	–

Table 5.8.: Results of simulations for alternative low-Z shielding designs, for 1 million primary muons in air, in units of counts/(kg · days). The value without any shielding is only given for reference; although with respect to muons only this actually gives the lowest background, a shielding will nevertheless be absolutely necessary against radioactivity. The bars indicate that simulation of one million muons is not sufficient to produce any events in the respective category.

shielding	seen in det	only one seg	had in det	had in one seg	only had	only had one seg
100 cm PE	$6.28 \cdot 10^{-3}$	$1.94 \cdot 10^{-3}$	$6.56 \cdot 10^{-4}$	$4.89 \cdot 10^{-5}$	$3.37 \cdot 10^{-7}$	$3.37 \cdot 10^{-7}$
5 m water	$5.48 \cdot 10^{-3}$	$1.38 \cdot 10^{-3}$	$6.10 \cdot 10^{-4}$	$7.15 \cdot 10^{-5}$	$4.77 \cdot 10^{-6}$	$4.77 \cdot 10^{-6}$
no shielding	$2.14 \cdot 10^{-2}$	$1.20 \cdot 10^{-2}$	$8.26 \cdot 10^{-4}$	$5.34 \cdot 10^{-5}$	$1.64 \cdot 10^{-5}$	$1.23 \cdot 10^{-5}$

Table 5.9.: Results of simulations for alternative low-Z shielding designs, for 1 million primary muons, in units of counts/(kg · days); setup with concrete and rock. As in Table 5.8, the value without any shielding is only given for reference.

Also with this slightly modified setup some simulations avoiding the use of high-Z materials have been performed; results are shown in Tables 5.8 and 5.9. As can be seen by comparison with Tables 5.3–5.7, the background is comparable to or even lower than in the case of conventional shieldings.

5.1.4. "Toy Geometry" vs "Real Geometry"

In the present work the geometries used in the simulations are simple "toy" geometries—consisting mostly of concentric cubes—which concentrate on the general concepts of the shieldings, thereby allowing easy modification and comparison. The question is, of course, whether the information gained in this way is actually useful for the assessment of realistic shieldings. For this purpose a comparison has been made between existing simulations using the detailed GERDA geometry as implemented in MaGe [Bau05] (see Fig. 5.10) and new simulations using a toy geometry comparable in dimensions (see Fig. 5.11). In the toy geometry the detector is made of enriched germanium and has an edge length of 25 cm. It is concentrically embedded in an inner shielding of liquid nitrogen with an edge length of 3 m and an outer shielding of water with an edge length of 10 m. This setup is surrounded with a 4 cm thick plastic scintillator muon veto. Some results are given in Table 5.10. The differences between different runs of the unchanged toy geometry simulation are bigger than the differences between the simulations using

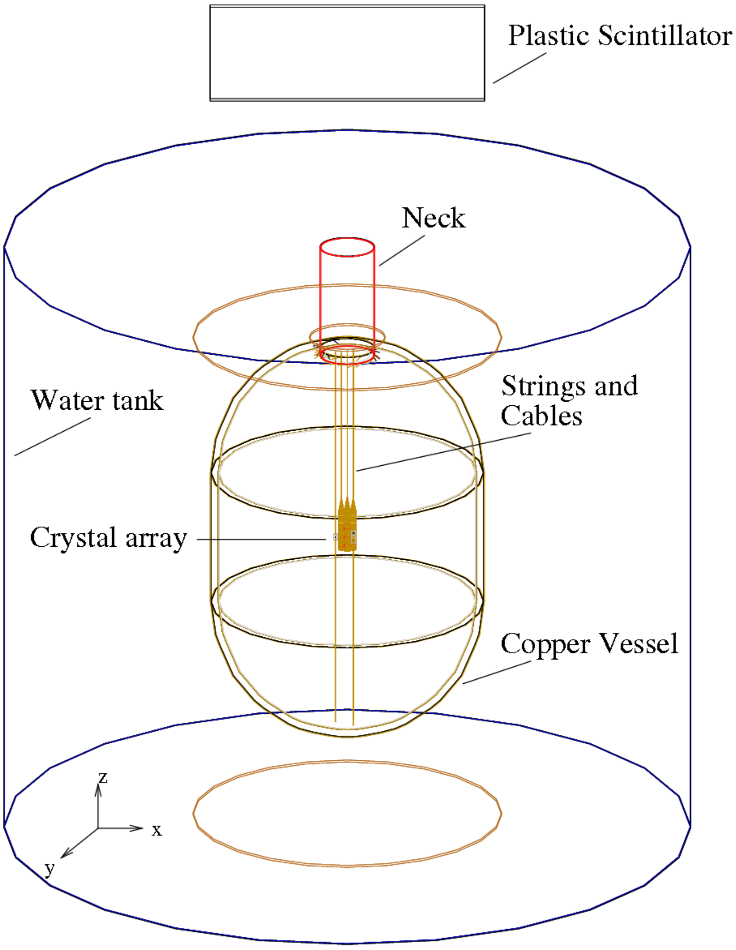

Figure 5.10.: GERDA geometry as implemented in MaGe [Krö05]

	GERDA	Toy-1	Toy-2	Toy-3
no cut	$3.3 \cdot 10^{-3}$	$3.0 \cdot 10^{-3}$	$7.8 \cdot 10^{-4}$	$6.3 \cdot 10^{-4}$
anticoincidence	$1.0 \cdot 10^{-3}$	$1.0 \cdot 10^{-3}$	$4.1 \cdot 10^{-4}$	$2.9 \cdot 10^{-4}$
top muon veto		$2.2 \cdot 10^{-3}$	$5.5 \cdot 10^{-4}$	$1.5 \cdot 10^{-5}$
anticoinc + top	$4.4 \cdot 10^{-4}$	$7.4 \cdot 10^{-4}$	$2.6 \cdot 10^{-4}$	

Table 5.10.: Comparison of toy geometry vs. realistic GERDA geometry. All results are given in units of counts/(kg · keV · year) for the range 1.5–2.5 MeV. The GERDA simulation uses a measured muon energy and angular distribution while the toy simulations use a measured muon energy and a $1/\cos\theta$ muon angular distribution. Toy-1 and Toy-3 are simulated using Geant4 version 6.2-patch02 64-bit, Toy-2 uses Geant4 version 7.0-patch01 32-bit. The GERDA and Toy-3 results are already published in [Bau05].

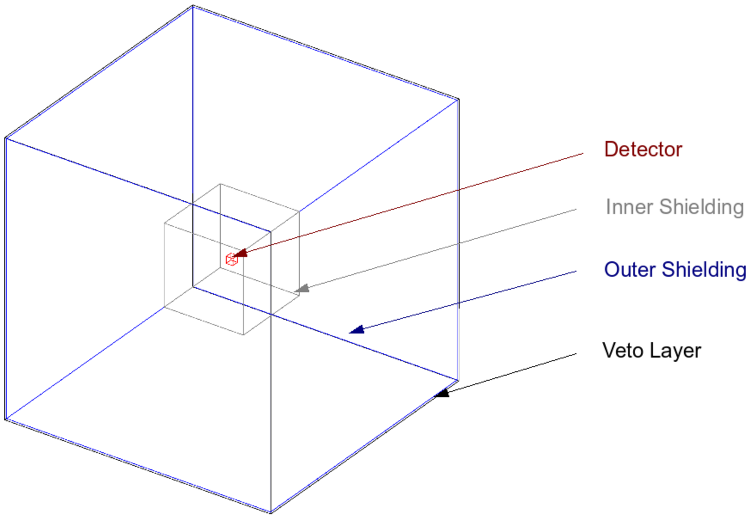

Figure 5.11.: Toy geometry as used in the GERDA comparison

the toy geometry and the full geometry. Therefore it is concluded that the toy geometry presented in this work is a good approximation to a realistic geometry and can be used for the comparison of different shielding designs.

5.1.5. Gran Sasso Generator vs Frejus Generator

A variant of the toy geometry comparable in dimensions to the CRESST geometry is simulated. The sensitive volume has an edge length of 30 cm. The shielding consists of 14 cm of copper, 20 cm of lead and 50 cm of polyethylene and is surrounded by a 5 cm thick plastic scintillator muon veto. The setup is placed in a hall of 13 m edge length filled with air and surrounded by 50 cm of LNGS concrete and 2.95 m of LNGS rock; their compositions are given in Tables 4.2 and 4.3. This simulation is done using Geant4 version 8.2.patch-01 and is also intended as a cross-check of the Gran Sasso and Frejus muon generators as well as of results obtained with $CaWO_4$ and Ge detectors, therefore all four possible combinations of generators and detector materials have been simulated. Results are shown in Table 5.11. There is no systematic difference in the results between the two different detector materials. Also, when taking into account the fact that the muon flux in Gran Sasso is about 5 times higher than in Frejus, i.e. about 1.1 $\mu/(\mathrm{m}^2 \cdot \mathrm{hr})$ instead of 0.2 $\mu/(\mathrm{m}^2 \cdot \mathrm{hr})$, results obtained with both generators are comparable and scale with muon flux; however, the veto efficiency seems to be somewhat higher with the

	Frejus $CaWO_4$	Frejus Ge	Gran Sasso $CaWO_4$	Gran Sasso Ge
seen in detector	$6.11 \cdot 10^{-3}$	$6.91 \cdot 10^{-3}$	$3.50 \cdot 10^{-2}$	$3.97 \cdot 10^{-2}$
in detector but not in veto	$6.91 \cdot 10^{-6}$	$7.07 \cdot 10^{-6}$	$4.33 \cdot 10^{-4}$	$4.86 \cdot 10^{-4}$
in only one segment	$1.55 \cdot 10^{-3}$	$1.52 \cdot 10^{-3}$	$7.38 \cdot 10^{-3}$	$6.74 \cdot 10^{-3}$
in one seg but not in veto	$3.58 \cdot 10^{-6}$	$2.67 \cdot 10^{-6}$	$2.27 \cdot 10^{-4}$	$1.62 \cdot 10^{-4}$
hadronics seen in det	$7.51 \cdot 10^{-4}$	$8.40 \cdot 10^{-4}$	$1.17 \cdot 10^{-2}$	$1.33 \cdot 10^{-2}$
had in det but nothing in veto	$1.69 \cdot 10^{-6}$	$3.77 \cdot 10^{-6}$	$3.79 \cdot 10^{-5}$	$2.01 \cdot 10^{-4}$
had in det in only one seg	$1.28 \cdot 10^{-4}$	$1.17 \cdot 10^{-4}$	$1.78 \cdot 10^{-3}$	$1.74 \cdot 10^{-3}$
had in one seg but not in veto	$5.90 \cdot 10^{-7}$	$6.29 \cdot 10^{-7}$	$1.08 \cdot 10^{-5}$	$7.71 \cdot 10^{-6}$
only hadronics in det	$2.95 \cdot 10^{-4}$	$3.46 \cdot 10^{-4}$	$4.46 \cdot 10^{-3}$	$5.25 \cdot 10^{-3}$
only had but nothing in veto	$1.08 \cdot 10^{-4}$	$1.04 \cdot 10^{-4}$	$1.57 \cdot 10^{-3}$	$1.53 \cdot 10^{-3}$
only had in only one seg	$1.18 \cdot 10^{-6}$	$1.89 \cdot 10^{-6}$	$5.41 \cdot 10^{-6}$	$3.86 \cdot 10^{-5}$
only had in one seg not in veto	$5.06 \cdot 10^{-7}$	$6.29 \cdot 10^{-7}$	–	$7.71 \cdot 10^{-6}$

Table 5.11.: Comparison of simulations in CRESST-like toy geometry with $CaWO_4$ or Ge target using the Gran Sasso and Frejus muon generators. Results are given in units of counts/(kg · days).

Frejus generator.

5.2. Shielding Design Studies for EURECA

5.2.1. Overview

The future tonne-scale cryogenic direct Dark Matter search experiment EURECA (European Underground Rare Event Calorimeter Array) [Kra08] will be located in an extension of the Laboratoire Souterrain de Modane (LSM) about 1700 m (4600 m w.e.) deep under the Frejus mountain, alongside a road tunnel close to the French–Italian border. As the space in the existing laboratory is already completely used up (see Fig. 5.12), two new halls will be built in order to extend the size of the laboratory from about 3500 m^3 to 55000 m^3 (see Fig. 5.13) [LSMHP]. Since the construction of the tunnel has to be extended anyway in order to meet European road safety standards, this expansion plans are rather cost-effective and have a good chance of being implemented. EURECA aims to reach a sensitivity for the WIMP–nucleon cross section of 10^{-9}–10^{-10} pb. This corresponds to only a few events per tonne of target material per year, therefore the background has to be even lower and an excellent shielding is extremely important. The following shielding and vetoing strategies for the new halls are discussed:

- A “standard” hall in which the vetoing of muon events and the shielding against local radioactivity is done directly around the experiment, as in conventional underground laboratories (see Fig. 5.14)

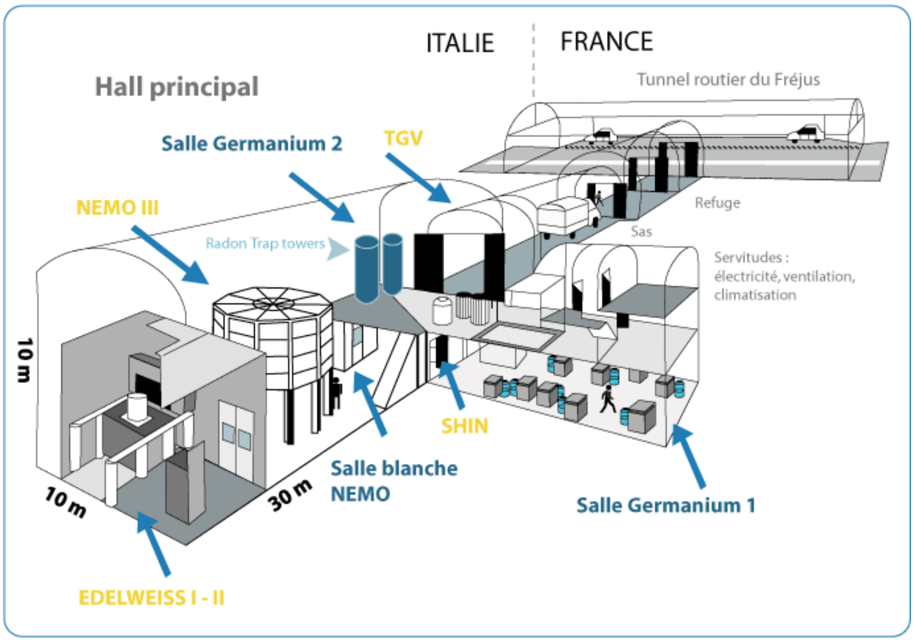

Figure 5.12.: Existing hall of the Frejus underground laboratory [LSMHP]

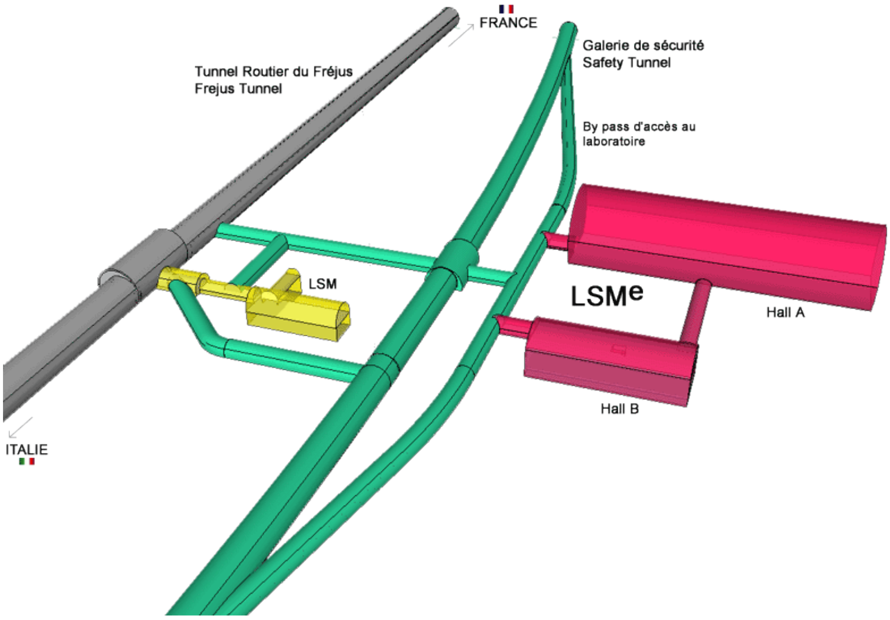

Figure 5.13.: Extension plans of the Frejus underground laboratory. The yellow hall labeled “LSM” is the currently existing lab, the pink halls labeled “LSMe” are the planned extensions which are much bigger than the original hall. They are intended to be built in conjunction with the road safety tunnel shown in green [LSMHP]

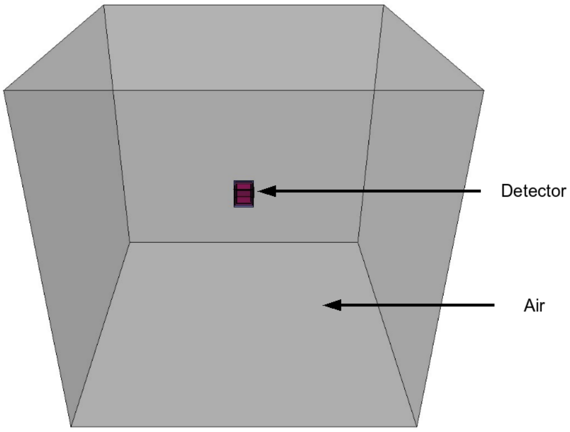

Figure 5.14.: “Standard hall” shielding design as implemented in the simulation

- A “submarine” design in which the complete hall is submerged in water (see Fig. 5.15). The water serves as a shielding and a Cerenkov muon veto. The fact that water is suitable as a shielding is shown in sections 5.1.2 and 5.1.3. This design is supposed to have the following advantages: The amount of high-Z material directly around the detector, which could increase the background by radioactivity or by acting as a spallation target for muons and high energy neutrons, is reduced. The muon veto surrounds the entire hall and not only the experimental setup itself, therefore also neutrons produced in the surrounding material can be vetoed: If a muon-induced shower passes in the rock a few metres away from the experimental hall so that the muon or other electromagnetic shower particles do not hit the experimental setup, there is still the possibility that neutrons produced by the shower in the rock enter the experiment, which are not seen by a conventional muon veto. In order for these neutrons to be vetoed the muon veto would have to be positioned some metres deep into the rock, which unfortunately is extremely difficult for practical as well as financial reasons. What however is possible is to use a huge water tank as an active shield. It can veto via the Cerenkov effect what is produced in the last few metres outside the experimental hall. It also moderates the neutrons produced in the last few metres of rock while due to its lower Z not so many new neutrons are produced there by the muons. Still, access to the cryostat is quite easy.
- A “pool” design in which the cryostat is directly submerged into the water shielding (see Fig. 5.16). In this case no steel hall construction is necessary, reducing the size of the water tank as well as the amount of high-Z material between the muon veto and the cryostat to the absolute minimum, at the expense of much more difficult access to the cryostat. A somewhat more conventional version of this design consists

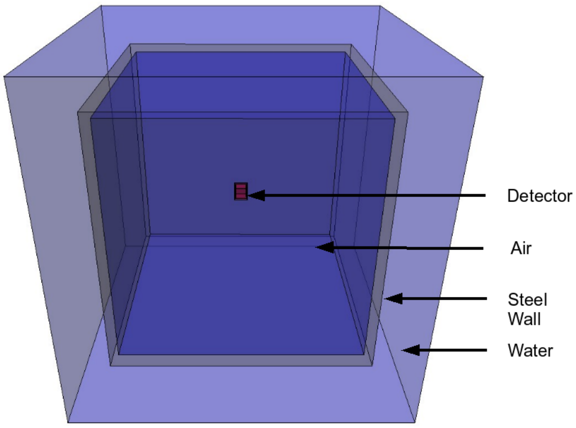

Figure 5.15.: "Submarine" shielding design as implemented in the simulation

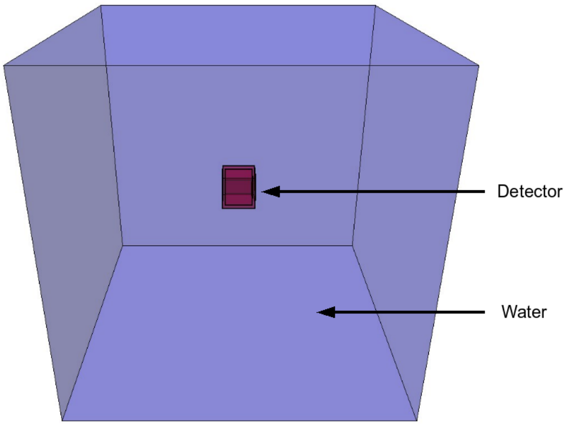

Figure 5.16.: "Pool" shielding design as implemented in the simulation

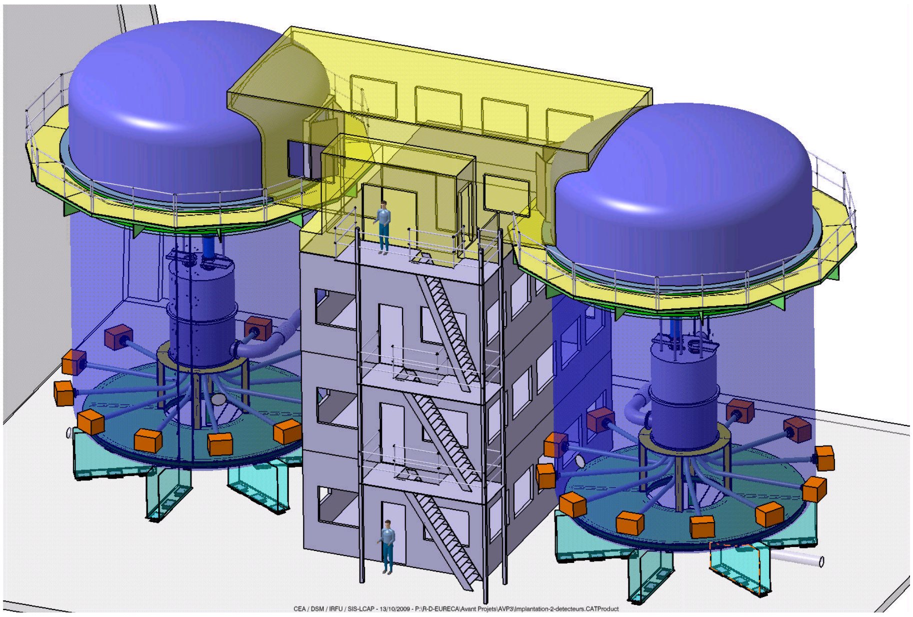

CEA / DSM / IRFU / SIS-LCAP - 13/10/2009 - P:\R-D-EURECA\Avant Projets\AVP3\Implantation-2-detecteurs.CATProduct

Figure 5.17.: More conventional version of the "pool" shielding design option with cryostats in water tanks inside a standard hall [Ger11]

of a cryostat in a water tank placed inside a standard hall (see Fig. 5.17). This still has the advantage of avoiding high-Z materials directly around the detector while possibly providing easier access to the experiment. At the time of writing this is the preferred option for the EURECA design.

In the present work schematic designs for these shielding strategies are simulated. Geant4 version 9.1.patch-01 is used for these simulations. The detector is assumed to be a cube with 60 cm edge length made from natural germanium (see Fig. 5.18). This amount of germanium has a mass of 1149.77 kg, corresponding nicely to the planned target mass of EURECA of 1 tonne. Of course, the EURECA detector will not be one monolithic block of material but consist of many smaller crystals, the main reason being that it is not possible to grow single crystals with a mass in the tonne-scale range. Using multiple detectors also has the advantage that anti-coincidences between the crystals can be evaluated in order to discriminate between neutrons (which may scatter in more than one detector) and WIMPs (which will only scatter once due to their small cross section). This effect is taken into account in the simulation by segmenting the detector into $3 \times 3 \times 3$ pieces in software during analysis. For the wall strengths of the cryostat and of the steel tank of the submarine design one rather small and one rather large value are simulated, so that results for the true wall strength can be obtained by interpolation between the four simulated combinations. In the version of the simulation with thin wall strength the cryostat is approximated by a copper dewar with 3 mm outer wall strength and 1 mm inner wall strength filled with 5 cm of liquid helium, while in the version with thick wall strength the inner and outer wall strengths are 1 cm each. The

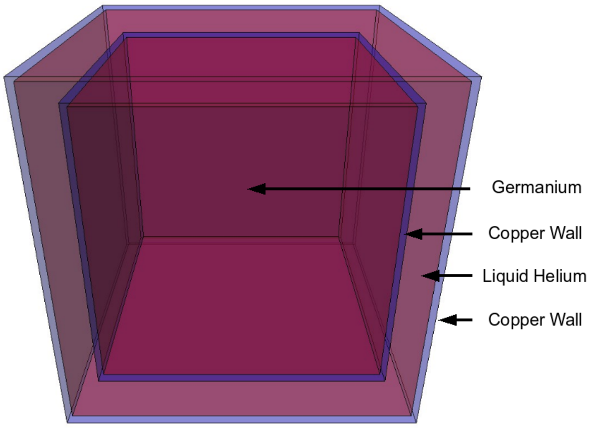

Figure 5.18.: Detector and cryostat as implemented in the simulation

Element	C	O	Mg	Al	Si
Weight %	6.56	48.6849	0.8856	4.7732	14.1776
Element	S	K	Ca	Mn	Fe
Weight %	0.4025	1.2504	20.4815	0.0953	2.6890

Table 5.12.: Elemental composition of Frejus rock as used in the simulations [Hor07, Rho93]

size of the halls which in reality is planned to be about $42 \times 11 \times 6\,\mathrm{m}^3$ (see Figs. 5.19 and 5.20) is simplified to $13 \times 13 \times 13\,\mathrm{m}^3$. For the submarine design the thickness of the water is assumed to be 2 m, with a steel wall of 4 cm (thin version) or 40 cm (thick version) thickness for the experimental hall. The pool design has an edge length of 7 m corresponding to a water thickness of 3.146 m around the thin and 3.13 m around the thick cryostat. The amount of rock taken into account in these simulations is 10 m. The composition of the rock is given in Table 5.12.

The threshold of the muon veto has initially been calculated using a typical energy deposition of $2\,\mathrm{MeV}/(\mathrm{g} \cdot \mathrm{cm}^2)$ for the shortest possible path length of a through-going muon in the veto. This corresponds to a threshold of 800 MeV for the submarine design with 4 m of water (2 m around each side of the hall), 1260 MeV for the pool design with roughly $2 \times 3.15\,\mathrm{m}$ of water and 16 MeV for the standard hall with $2 \times 4\,\mathrm{cm}$ of plastic scintillator. These values are also expected to be achievable in a real veto system: Super-Kamiokande in its original configuration, for example, reaches in its inner water Cerenkov detector (33.8 m radius, 36.2 m height, filled with 32 ktonnes of water, observed by 11146 50-inch PMTs) an energy threshold of 4.5 MeV with a PMT coverage of 40% [SK03]. The

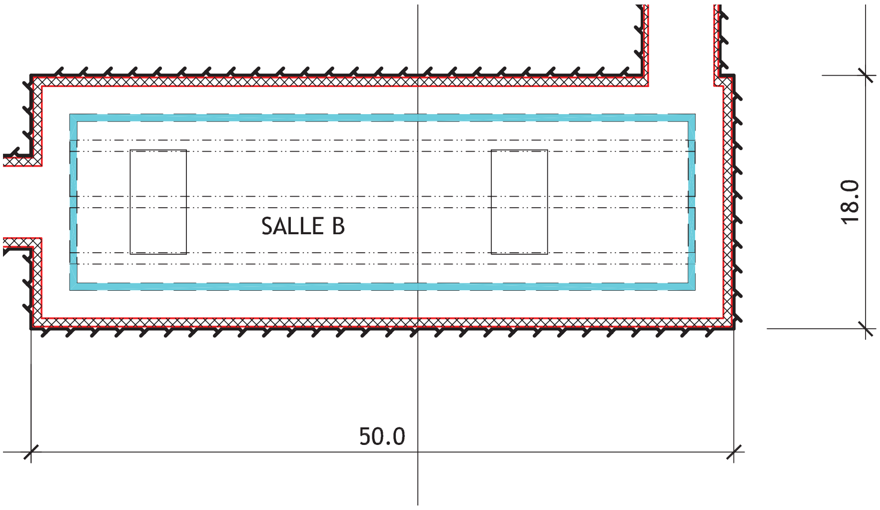

Figure 5.19.: Top view of the planned LSM extension hall B where the EURECA experiment will be located (all sizes given in metres) [Lom07]

PMT coverage of the EURECA muon veto will be much lower. If it is assumed to be 1% the threshold is expected to go up by a factor of 40 leading to a value of 180 MeV, and the possibility of geometric shading due to the experimental hall placed inside the water tank may lower the veto efficieny even further. However, it has been found that except for the standard hall, simulation results depend heavily on the veto threshold (see below). For some of the design variants under study the background is so low after applying the veto using these calculated veto thresholds that almost all background events are vetoed and that it is not possible to simulate a reasonable number of relevant background events in appropriate time. This is obviously good for the actual experiment, but the low statistics makes the comparison of the shieldings more difficult. Therefore, to highlight the differences between the shielding designs, the veto threshold has been increased for the following analysis. The veto energy spectra for the different designs are shown in figure 5.21. The muon peaks are clearly visible, its segmented structure in the submarine design is a geometry effect due to the hall being inside the veto. The veto threshold can now be selected below, inside or above the muon peak, depending on the preferences regarding maximum veto efficiency or reliable muon identification. The dependence of the results on the veto threshold is shown in Figs. 5.22, 5.23 and 5.24. In the case of the submarine design, the largest jump is between 800 and 1000 MeV veto threshold, therefore 1000 MeV is used as standard threshold in the following analysis. Similarly, in the pool design 1660 MeV is taken as standard threshold. In reality the veto thresholds are expected to be lower. In the case of the standard hall the influence of the

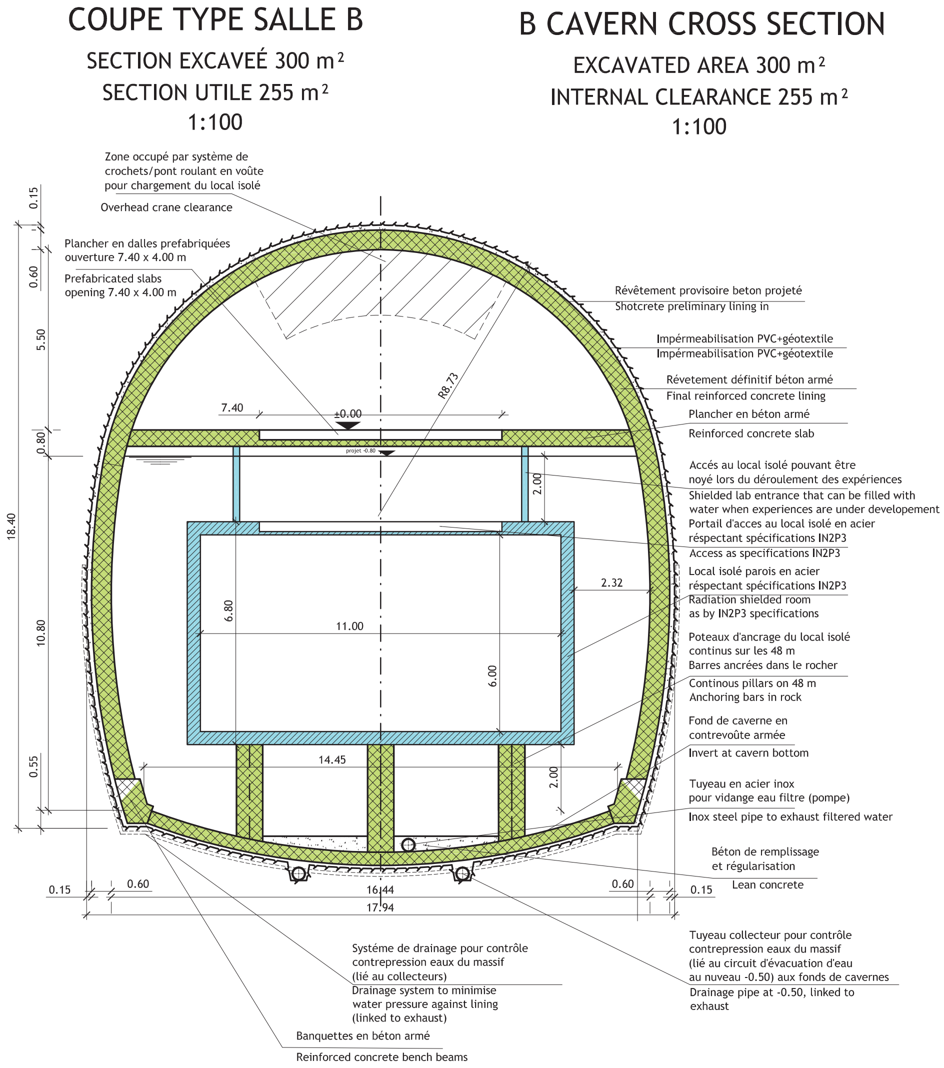

Figure 5.20.: Side view of the planned LSM extension hall B where the EURECA experiment will be located (all sizes given in metres) [Lom07]

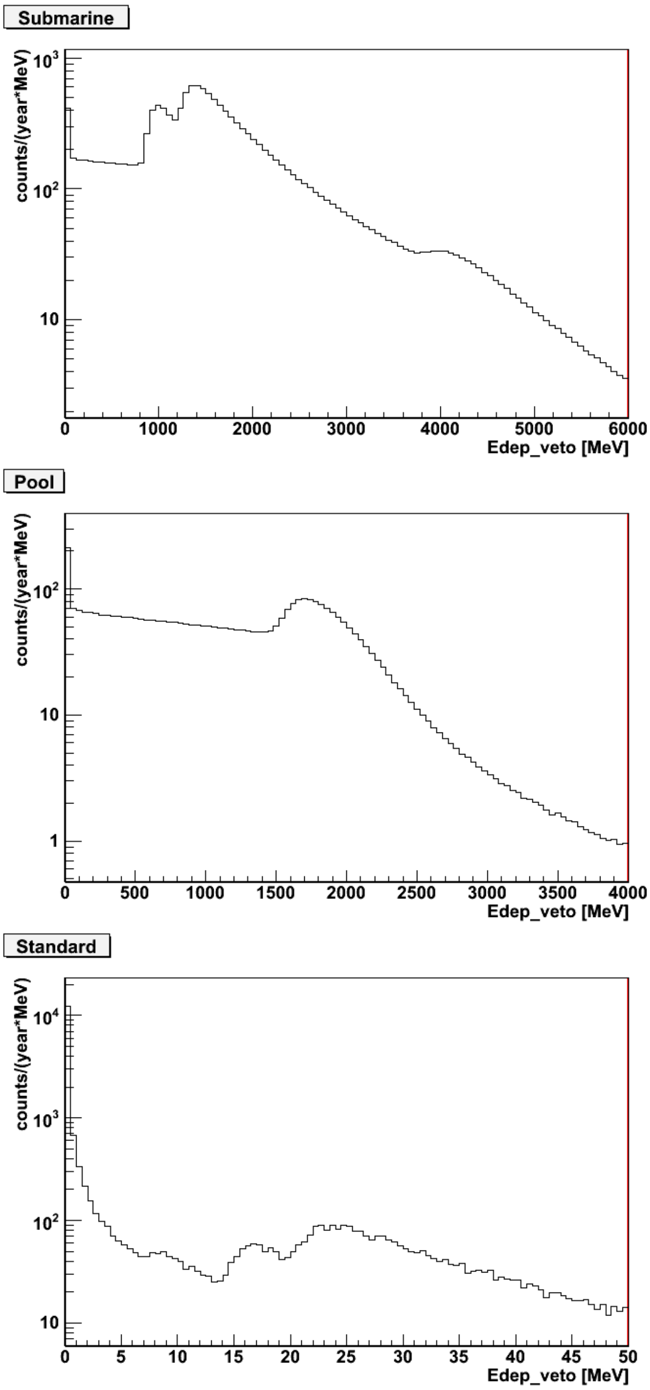

Figure 5.21.: Energy spectra of the veto detector in the submarine, pool and standard designs (from top to bottom); all with thick cryostat, submarine with thin steel wall. Position and shape of the peaks depend on the length of the path the muons travel through the veto.

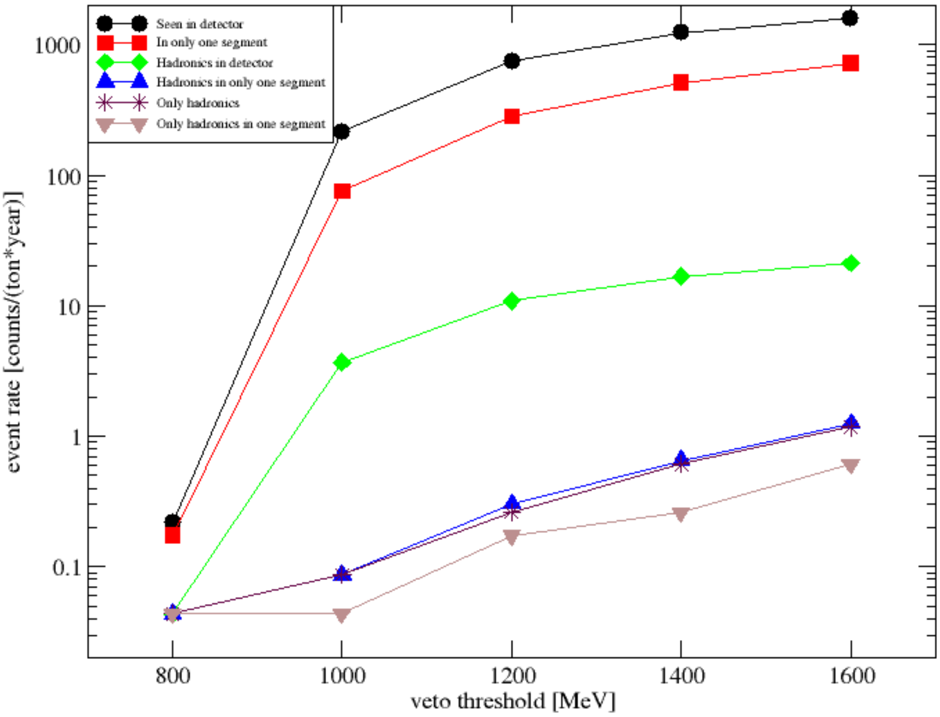

Figure 5.22.: Veto threshold dependence of background rates in the submarine design. Due to the steep increase between 800 and 1000 MeV, the latter value has been chosen as veto threshold.

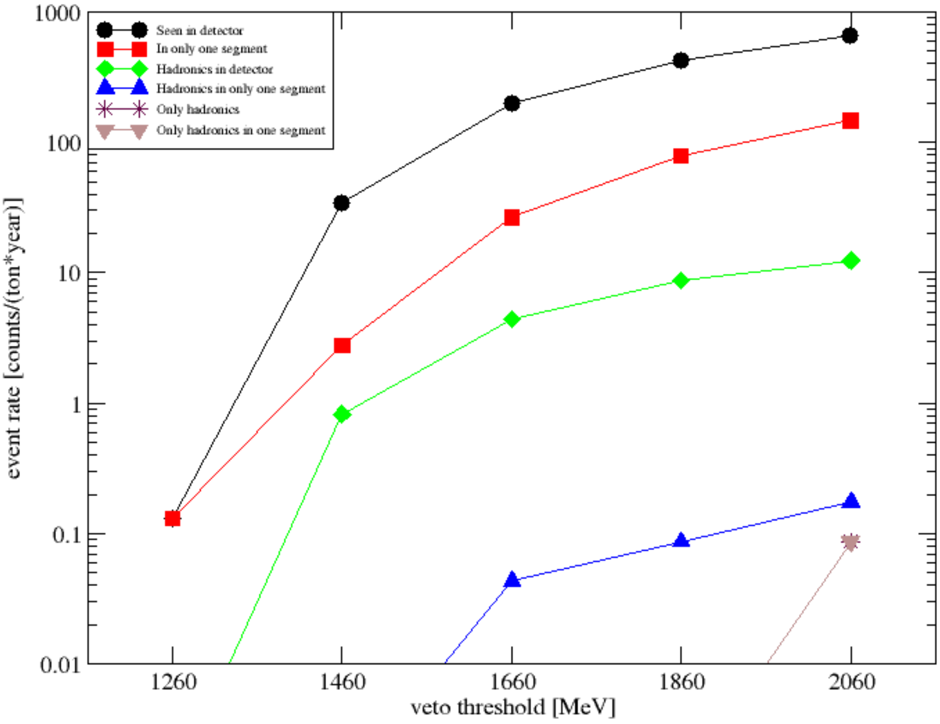

Figure 5.23.: Veto threshold dependence of background rates in the pool design. To include hadronic events seen in only one segment of the detector, the veto threshold has been set to 1660 MeV.

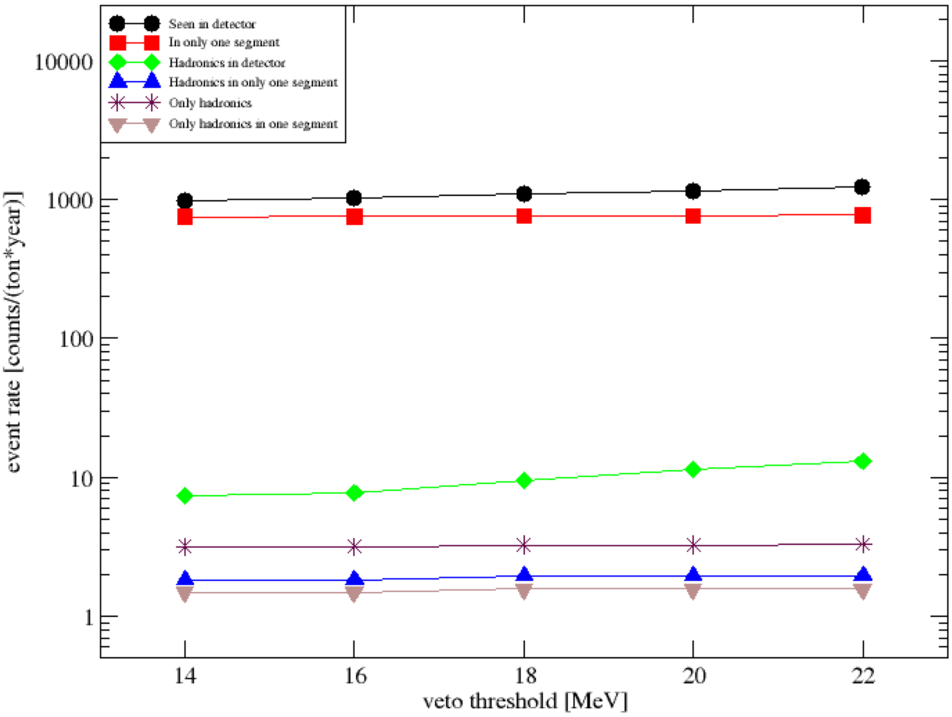

Figure 5.24.: Veto threshold dependence of background rates in the standard design. As the background rate is almost independent of the veto threshold, 16 MeV (corresponding to the expected energy deposition of a vertical muon in 2 × 4 cm of plasic scintillator) has been used.

steel wall	thin		thick	
cryostat	thin	thick	thin	thick
simulated time [years]	8.74	16	10.98	9.36
seen in detector	4951.66	2841.56	4793.66	2773.39
in detector but not in veto	256.22	217.11	513.76	352.83
in only one segment	3411.68	1632.26	3292.29	1587.3
in one seg but not in veto	117.47	75.61	308.48	171.63
hadronics seen in det	39.39	36.26	151.98	128.63
had in det but nothing in veto	2.78	3.7	12.04	12.45
had in det in only one seg	7.06	4.57	53.86	39.66
had in one seg but not in veto	0	0.11	3.33	3.06
only hadronics in det	8.16	5.82	97.73	75.51
only had but nothing in veto	0	0.11	6.97	5.67
only had in only one seg	5.77	2.99	49.1	35.2
only had in one seg not in veto	0	0.05	3.17	2.51

Table 5.13.: Simulation results for the different variants of the submarine design, in units of counts/(tonne · year)

veto threshold on the result is rather small, therefore the calculated value of 16 MeV is kept.

5.2.2. Submarine

In the submarine design the complete experimental hall is submerged in water. The results for the different variants of this design described in the previous section are given in Figs. 5.25 and 5.26 and Table 5.13. There are clear differences depending on the thicknesses of the cryostat and the steel wall. To understand the origin of these differences it is studied at which distances to the centre of the detector the muons responsible for the different types of event described on page 69 pass. This distance can be seen as an indication of how far from the detector the respective energy deposition takes place. To this end the cumulative sum of muons generating background as a function of distance is plotted. The muon trajectory is assumed to be a straight line, which is a good approximation at these high muon energies. The influence of the cryostat thickness is shown in Fig. 5.25. The steel wall is 4 cm thick in these simulations, while the cryostat is simulated once in its thinner and once in its thicker variant. The amount of background coming from the vicinity of the detector is only very slightly increased in the case of the thick cryostat as compared to the thin one; the amount of background coming from farther away, however, is much higher with the thin cryostat. This suggests that the copper of the cryostat acts as a shielding against events coming from outside. With respect to muon-induced background a thicker cryostat therefore even is an advantage.

The total number of background events is almost independent of the thickness of the steel

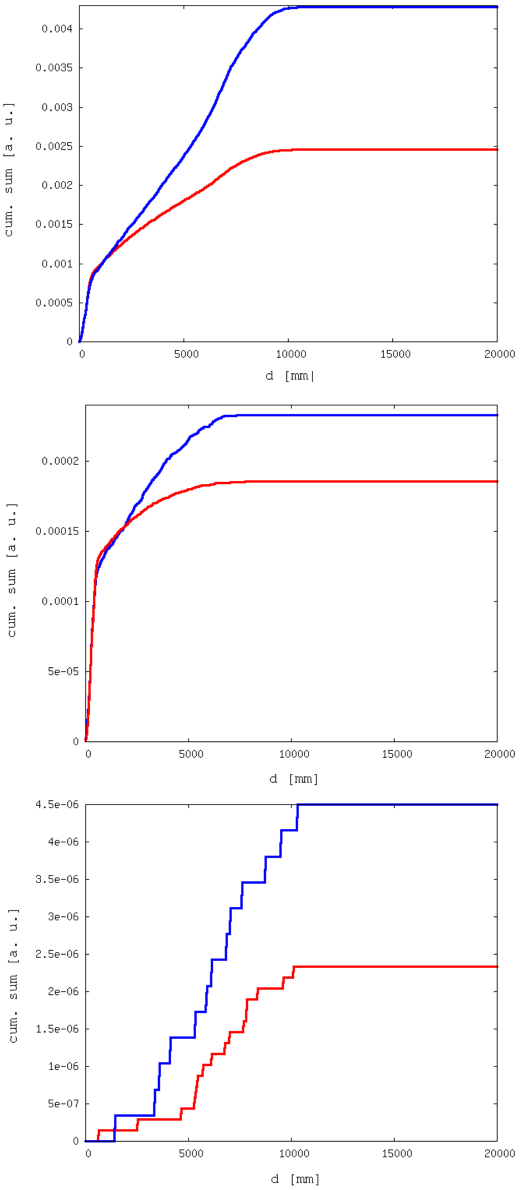

Figure 5.25.: Influence of cryostat thickness on the background in the submarine design with a thin steel wall. The version with the thin cryostat is shown in blue, the one with the thick cryostat in red. Shown is the cumulative sum of muons generating background depending on their closest distance d to the centre of the detector. From top to bottom: seen in detector; seen in detector but not in veto; only hadronics in only one segment. The background coming from the vicinity of the detector is only very slightly increased in the case of the thick cryostat compared to the thin one; on the other hand, the background coming from farther away is actually considerably lower with the thick cryostat, suggesting that it acts as a shielding against events coming from outside.

cryostat	thin	thick
simulated time [years]	43.87	20.14
seen in detector	1247.04	1192.53
in detector but not in veto	171.46	197.7
in only one segment	405.82	337.28
in one seg but not in veto	25.66	26.56
hadronics seen in det	21.27	25.78
had in det but nothing in veto	2.72	4.4
had in det in only one seg	0.22	0.43
had in one seg but not in veto	0.02	0.04
only hadronics in det	0.18	0.22
only had but nothing in veto	0	0
only had in only one seg	0.1	0.13
only had in one seg not in veto	0	0

Table 5.14.: Simulation results for the different variants of the pool design, in units of counts/(tonne · year)

wall (see Fig. 5.26). However, the number of events not seen in the veto as well as the number of dangerous events with only hadronic energy deposition in only one segment is significantly increased in the case of the thicker steel wall. Of all cases considered in the present work this is the only one in which the design background goal of one count per tonne and year cannot be reached without taking the veto into account. The situation is even aggravated by the fact that the thicker steel wall lowers the veto efficiency. Therefore, in the submarine design it is of utmost importance to keep the thickness of the steel wall down to an absolute minimum.

5.2.3. Pool

In the pool design the cryostat is directly submerged in water; in the version considered in this work there is no steel hall around the setup. The results for the two versions with the thin and the thick cryostat are given in Table 5.14. The selected cryostat thickness has almost no influence on the background. The shielding effect of the thicker cryostat which has been observed in the submarine design is only slightly seen in all events as well as in events seen in only one segment of the detector, while the number of events not seen in the veto as well as the number of hadronic events is slightly increased. All in all, however, this design is remarkably stable against changes in cryostat thickness.

5.2.4. Standard Hall

In the present work the standard hall is simulated for comparison to demonstrate the effect of the different types of integrated water shield. It is therefore treated only rudi-

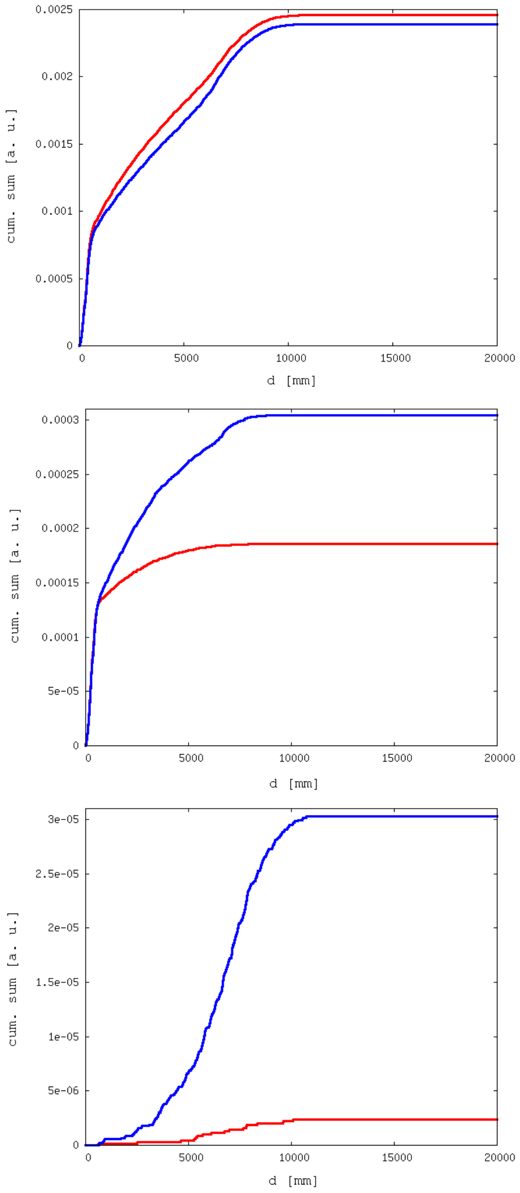

Figure 5.26.: Influence of steel wall thickness on the background in the submarine design with a thick croystat. The version with the thin steel wall is shown in red, the one with the thick steel wall in blue. Shown is the cumulative sum of muons generating background depending on their closest distance d to the centre of the detector. From top to bottom: seen in detector; seen in detector but not in veto; only hadronics in only one segment. While the total number of events seen in the detector is almost independent of the thickness of the steel wall, the number of events not seen in the veto and the number of dangerous events with only hadronic energy deposition in only one segment is significantly increased in case of the thick steel wall. Therefore the steel wall should be kept as thin as possible.

cryostat	thin	thick
simulated time [years]	13.31	17
seen in detector	3176.66	2020.33
in detector but not in veto	2185.2	1020.73
in only one segment	1988.21	987.02
in one seg but not in veto	1748.16	755.33
hadronics seen in det	30.65	30.13
had in det but nothing in veto	9.41	7.72
had in det in only one seg	3.01	2.35
had in one seg but not in veto	2.55	1.84
only hadronics in det	3.2	3.48
only had but nothing in veto	2.94	3.17
only had in only one seg	1.9	1.69
only had in one seg not in veto	1.7	1.48

Table 5.15.: Simulation results for the different variants of the standard hall design, in units of counts/(tonne · year)

mentary in the sense that it contains no shielding around the cryostat, which of course would be required in any real experiment to protect against local radioactivity. The muon veto is a 4 cm thick plastic scintillator located directly around the cryostat. Results for the two different cryostat thicknesses are given in Table 5.15. With respect to all events the thick cryostat serves as a good shielding, whether veto or segmentation is taken into account or not; for hadronic events the thickness of the cryostat almost makes no difference (see Fig. 5.27).

5.2.5. Comparison

Realistically it can be assumed that the amount of material used in construction of the cryostat is closer to the "thick" cryostat, while the wall thickness of the steel tank in the case of the submarine is expected to be closer to the "thin" steel wall of the simplified design (except for the girder structure). Therefore, only these variants are considered further. Events with purely hadronic energy deposition in only one segment of the detector are the most dangerous background. Without taking the muon veto into account, there are 2.99 counts/(tonne · year) of this background in the submarine design but only 0.13 counts/(tonne · year)in the pool design. The origin of this background in the submarine and pool designs is examined in Fig. 5.28. The background coming from the vicinity of the detector is almost the same for both designs, but in the case of the submarine there is a substantial amount of additional background coming from farther distances which is generated in the steel wall of the submarine. Although most of it will be seen by the muon veto, reducing the above numbers to 0.05 counts/(tonne · year)in the submarine design and zero events in about 20 years running time in the

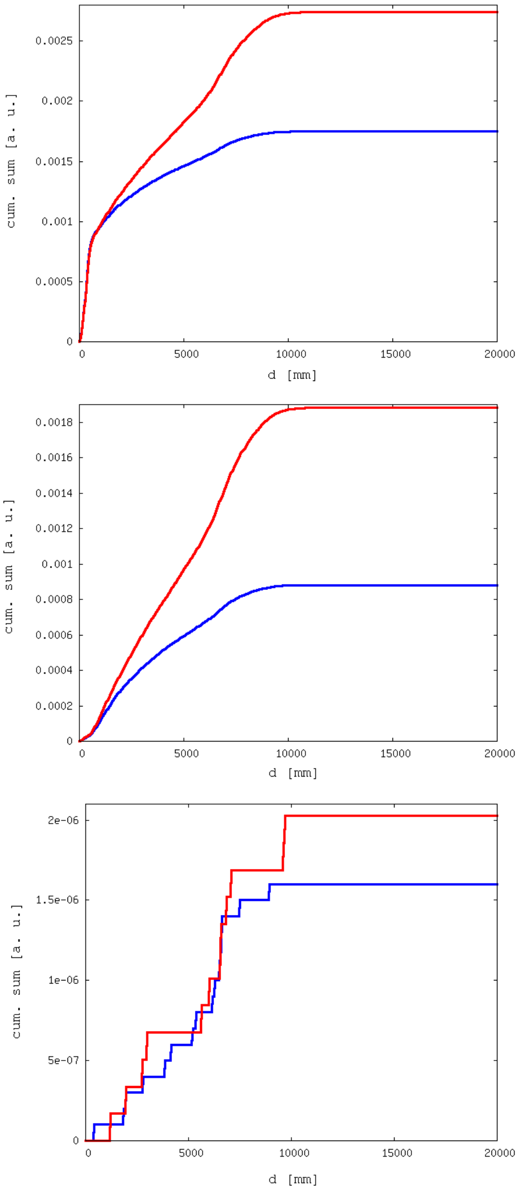

Figure 5.27.: Influence of cryostat thickness on the background in the standard design. The version with the thin cryostat is shown in red, the one with the thick cryostat in blue. Shown is the cumulative sum of muons generating background depending on their closest distance d to the centre of the detector. From top to bottom: seen in detector; seen in detector but not in veto; only hadronics in only one segment. The thick cryostat serves as a good shielding with respect to the total number of events seen in the detector; for hadronic events the difference is less pronounced.

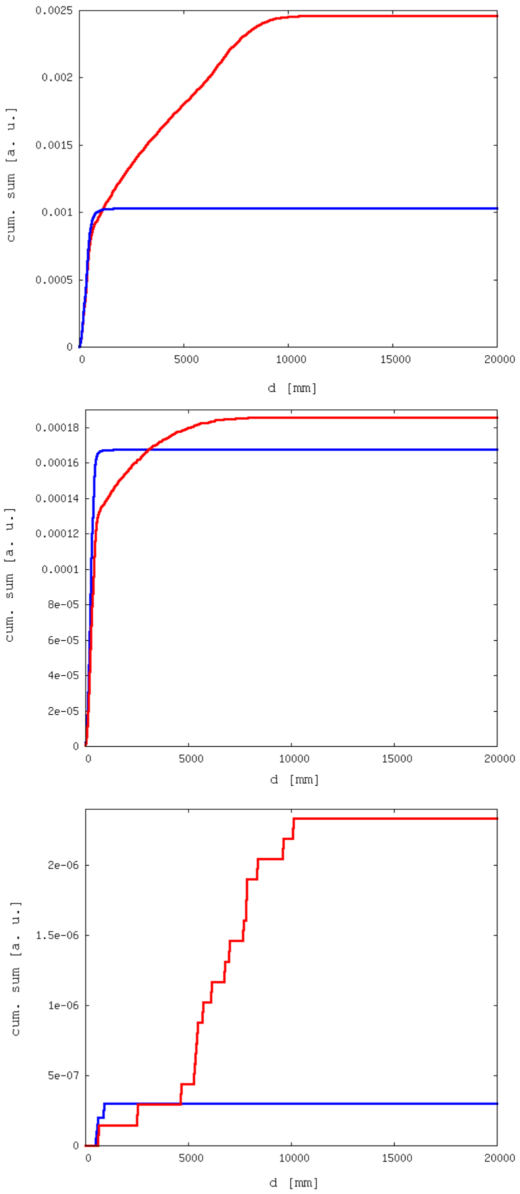

Figure 5.28.: Comparison of submarine (red) and pool (blue) designs. Shown is the cumulative sum of muons generating background depending on their closest distance d to the centre of the detector. From top to bottom: seen in detector; seen in detector but not in veto; only hadronics in only one segment. The background coming from the vicinity of the detector is almost the same for both designs, but in the case of the submarine a lot of additional background is coming from farther distances. Therefore the pool design clearly is the better option with respect to muon-induced background

pool design, it is still a disadvantage having to rely on the veto for reaching the design background, as the efficiency of any real veto system will be less than 100% and the veto may also have holes due to the details of the geometry (e. g. cable and cryogenic feedthroughs). Therefore, with respect to muon-induced background the pool design clearly is the better option. Fortunately this is also true with respect to the background from local radioactivity [Tom09], therefore it has been decided to construct EURECA using a pool design [EUR12].

6. Summary and Outlook

In the present work the fundamental design of the shielding of the future direct Dark Matter search experiment EURECA against muon-induced neutrons is developed by way of Monte Carlo simulations using the GEANT4 toolkit. In GEANT4 the physics processes and models which are to be taken into account have to be selected by the user in a physics list. As no suitable predefined list is available at the time of the beginning of this work a suitable list is developed and verified. To better focus on the main features of the shielding and to improve flexibility a toy geometry consisting of concentric cubes is used. The usefulness of this type of geometry is shown by comparison with a more detailed version of the GERDA geometry. The optimum thickness of the different materials in a conventional shielding design is determined. The use of 20–30 cm of internal polyethylene and an as small amount of lead as possible is recommended while the thickness of the external polyethylene has only a small influence on the background rate.

As EURECA will be placed in a newly built underground laboratory it is possible to integrate some of the shielding directly into the laboratory hall. The two options considered are (1) a "submarine" design in which the entire laboratory hall is placed in water and (2) a "pool" design in which only the cryostat is submerged in water. It is found that with respect to muon-induced neutron background the pool design is greatly preferable as the additional background from the steel wall of the submarine design nullifies the shielding effects of the water. The goal background of one count/(tonne · year) of dangerous events can be reached with the pool design already without the muon veto while in the case of the submarine design the muon veto is needed.

The pool design has been shown to be the better option also with respect to local radioactivity [Tom09] and will therefore be used by EURECA [EUR12]. The currently favoured design consists of one or two small pools inside a conventional hall. This geometry deviates quite substantially from the version with one pool directly inside the rock presented in this work and will have to be simulated in more detail in the future.

A. A Geant4 Physics List for Dark Matter Searches

The physics list developed in the course of this work contains the following particles, processes and models (see also section 4.1.1):

- e^-
  - bremsstrahlung
  - ionization
  - multiple scattering
  - synchrotron radiation (optional)
  - electro nuclear reaction
- e^+
  - bremsstrahlung
  - annihilation
  - ionization
  - multiple scattering
  - synchrotron radiation (optional)
  - electro nuclear reaction
- γ
  - photo effect
  - compton effect
  - pair production
  - gamma nuclear reaction (up to 3.5 GeV), at higher energies quark-gluon string (QGS) model
- μ^+
  - ionization
  - bremsstrahlung

  - pair production
  - multiple scattering
  - muon nuclear interaction for muon deep inelastic scattering above 1 GeV
- μ^-
  - ionization
  - bremsstrahlung
  - pair production
  - multiple scattering
  - capture at rest
  - muon nuclear interaction for muon deep inelastic scattering above 1 GeV
- τ^+, τ^-
  - ionization
  - multiple scattering
- n
  - elastic scattering: neutron high precision (NHP) and low energy parameterized (LEP) model
  - inelastic scattering: NHP, binary cascade (BIC) or Bertini cascade (BERT), LEP and QGS model
  - capture: NHP and LEP model
  - fission: NHP and LEP model
- p
  - elastic scattering: LEP model
  - inelastic scattering: BIC (or BERT), LEP and QGS model
  - hadronic ionization
  - multiple scattering
- π^+, K^+
  - elastic scattering: LEP model
  - inelastic scattering: LEP and QGS model
  - hadronic ionization
  - multiple scattering

- π^-, K^-
  - elastic scattering: LEP model
  - inelastic scattering: LEP and QGS model
  - absorption
  - hadronic ionization
  - multiple scattering
- K_L^0, K_S^0
  - elastic scattering: LEP model
  - inelastic scattering: LEP and QGS model
- $\overline{p}$
  - elastic scattering
  - inelastic scattering: low energy parameterized (LEP) and high energy parameterized (HEP) model
  - annihilation
  - hadronic ionization
  - multiple scattering
- $\overline{n}$
  - elastic scattering
  - inelastic scattering: LEP and HEP model
  - annihilation
- Λ, $\overline{\Lambda}$, Ξ^0, $\overline{\Xi}^0$
  - elastic scattering
  - inelastic scattering: LEP and HEP model
- Σ^-, $\overline{\Sigma}^+$, Σ^+, $\overline{\Sigma}^-$, Ξ^-, $\overline{\Xi}^+$, Ω^-, $\overline{\Omega}^+$[1]
  - elastic scattering
  - inelastic scattering: LEP and HEP model
  - hadronic ionization

---

[1] In Geant4 nomenclature, the antiparticle of the Σ^-, for example, is called "anti-sigma-minus", although it has of course a positive charge. According to the PDG [PDG10, p. 13] this is written as $\overline{\Sigma}^+$(and not $\overline{\Sigma}^-$or $\overline{\Sigma^-}$), and this convention has been adopted in this work.

  - multiple scattering
- generic ion, ^{3}He
  - elastic scattering
  - ionization
  - multiple scattering
- deuteron, triton, alpha
  - elastic scattering
  - inelastic scattering
  - ionization
  - multiple scattering
- all unstable particles
  - decay

Bibliography

[Aal11] C. E. Aalseth *et al.* (CoGeNT Collaboration): "Results from a Search for Light-Mass Dark Matter with a P-type Point Contact Germanium Detector", Phys. Rev. Lett. 106 (2011) 131301, arXiv:1002.4703 [astro-ph.CO]

[Abb08] R. U. Abbasi *et al.* (High Resolution Fly's Eye Collaboration): "First Observation of the Greisen-Zatsepin-Kuzmin Suppression", Phys. Rev. Lett. 100 (2008) 101101, arXiv:astro-ph/0703099

[Abr08] J. Abraham *et al.* (The Pierre Auger Collaboration): "Observation of the suppression of the flux of cosmic rays above 4×10^{19} eV", Phys. Rev. Lett. 101 (2008) 061101. arXiv:0806.4302 [astro-ph]

[Abt04] I. Abt *et al.*: "GERDA: The GERmanium Detector Array for the search of neutrinoless $\beta\beta$ decays of ^{76}Ge at LNGS", Proposal to the LNGS P38/04, September 2004

[Adr08] O. Adriani *et al.*: "Observation of an anomalous positron abundance in the cosmic radiation", arXiv:0810.4995 [astro-ph]

[Adr09] O. Adriani *et al.*: "An anomalous positron abundance in cosmic rays with energies 1.5–100 GeV", Nature 458 (2009) 607

[Agl95] M. Aglietta *et al.* (LVD Collaboration): "Neutrino-induced and atmospheric single-muon fluxes measured over five decades of intensity by LVD at Gran Sasso Laboratory", Astropart Phys 3 (1995) 311

[Agl99] M. Aglietta *et al.* (LVD Collaboration): "Measurement of the Neutron Flux Produced by Cosmic-Ray Muons with LVD at Gran Sasso", Proc. 26th Intern. Cosmic Rays Conf., V.2 (1999) 44, arXiv:hep-ex/9905047

[Ahl93] S. Ahlen *et al.* (MACRO Collaboration): "Muon Astronomy with the MACRO Detector", ApJ 412 (1993) 301

[Ahm09a] Z. Ahmed *et al.* (CDMS Collaboration): "A Search for WIMPs with the First Five-Tower Data from CDMS", Phys. Rev. Lett. 102 (2009) 011301, arXiv:0802.3530 [astro-ph]

[Ahm09b] Z. Ahmed *et al.* (CDMS Collaboration): "Results from the Final Exposure of the CDMS II Experiment", arXiv:0912.3592 [astro-ph.CO]

[Ahm10] Z. Ahmed *et al.* (CDMS Collaboration): "Dark Matter Search Results from the CDMS II Experiment", Science 327 (2010) 1619

[Ahm11] Z. Ahmed *et al.* (CDMS Collaboration): “Results from a Low-Energy Analysis of the CDMS II Germanium Data”, Phys. Rev. Lett. 106 (2011) 131302, arXiv:1011.2482 [astro-ph.CO]

[AIDA] AIDA—Abstract Interfaces for Data Analyis: http://aida.freehep.org/

[Ake05] D. S. Akerib *et al.* (CDMS Collaboration): “Exclusion Limits on the WIMP-Nucleon Cross-Section from the First Run of the Cryogenic Dark Matter Search in the Soudan Underground Lab”, Phys. Rev. D 72 (2005) 052009, arXiv:astro-ph/0507190

[Alb86] C. Alberini *et al.*: “The Large-Volume Detector (LVD) of the Gran Sasso Laboratory”, Nuovo Cimento C 9 (1986) 237

[Alc00] C. Alcock *et al.* (The MACHO Collaboration): “The MACHO Project: Microlensing Results from 5.7 Years of Large Magellanic Cloud Observations”, Astrophys. J. 542 (2000) 281, arXiv:astro-ph/0001272

[All02] S. W. Allen *et al.*: “Cosmological constraints from the X-ray gas mass fraction in relaxed lensing clusters observed with Chandra”, MNRAS 334 (2002) L11, arXiv:astro-ph/0205007

[Amb95] M. Ambrosio *et al.* (MACRO Collaboration): “Vertical muon intensity measured with MACRO at the Gran Sasso laboratory”, Phys. Rev. D 52 (1995) 3793

[Amb02] M. Ambrosio *et al.* (MACRO Collaboration): “The MACRO detector at Gran Sasso”, NIM A 486 (2002) 663

[Amb03] M. Ambrosio *et al.* (MACRO Collaboration): “Measurement of the residual energy of muons in the Gran Sasso underground laboratories”, Astropart. Phys. 19 (2003) 313, arXiv:hep-ex/0207043

[And87] B. Andersson, G. Gustafson and B. Nilsson-Almqvist: “A model for low-p_T hadronic reactions with generalizations to hadron-nucleus and nucleus-nucleus collisions”, Nucl. Phys. B281 (1987) 289

[Ang05] J. Angrik *et al.* (The KATRIN Collaboration): “KATRIN Design Report 2004”, Report NPI ASCR Řež, EXP-01/2005, FZKA Scientific Report 7090, MS-KP-0501

[Ang08a] J. Angle *et al.* (XENON Collaboration): “First Results from the XENON10 Dark Matter Experiment at the Gran Sasso National Laboratory”, Phys. Rev. Lett. 100 (2008) 021303, arXiv:0706.0039 [astro-ph]

[Ang08b] J. Angle *et al.* (XENON Collaboration): “Limits on Spin-Dependent WIMP-Nucleon Cross Sections from the XENON10 Experiment”, Phys. Rev. Lett. 101 (2008) 091301, arXiv:0805.2939 [astro-ph]

[Ang09] G. Angloher *et al.*: “Commissioning Run of the CRESST-II Dark Matter Search”, Astropart. Phys. 31 (2009) 270, arXiv:0809.1829 [astro-ph]

[Ang12] G. Angloher *et al.*: "Results from 730 kg days of the CRESST-II Dark Matter Search", EPJ C 72 (2012) 1971, arXiv:1109.0702 [astro-ph.CO]

[Apr11] E. Aprile *et al.* (XENON100 Collaboration): "Dark Matter Results from 100 Live Days of XENON100 Data", Phys. Rev. Lett. 107 (2011) 131302, arXiv:1104.2549 [astro-ph.CO]

[Apr12] E. Aprile *et al.* (XENON100 Collaboration): "The XENON100 Dark Matter Experiment", Astropart. Phys. 35 (2012) 573, arXiv:1107.2155 [astro-ph.IM]

[Ara05] H. M. Araujo *et al.*: "Muon-induced neutron production and detection with GEANT4 and FLUKA", NIM A 545 (2005) 398, arXiv:hep-ex/0411026

[Arm11] E. Armengaud *et al.* (The EDELWEISS Collaboration): "Final results of the EDELWEISS-II WIMP search using a 4-kg array of cryogenic germanium detectors with interleaved electrodes", Phys. Lett. B 702 (2011) 329, arXiv:1103.4070 |astro-ph.CO]

[Att06] Michael J. Attisha: "Cryogenic Dark Matter Search (CDMS II) - Application of Neural Networks and Wavelets to Event Analyis", PhD thesis, Brown University, May 2006

[Aug10] The Pierre Auger Collaboration: "Measurement of the energy spectrum of cosmic rays above 10^{18} eV using the Pierre Auger Observatory", Phys. Lett. B 685 (2010) 239, arXiv:1002.1975 [astro-ph.HE]

[Bak76] M. Baker, K. A. Ter-Martirosyan: "Gribov's Reggeon calculus: its physical basis and implications", Phys. Rep. 28 (1976) 1

[Bau04] M. Bauer *et al.*: "Simulations of muon-induced neutron background with Geant4", Proceedings of the Fifth International Workshop on the Identification of Dark Matter, Edinburgh, UK, 6–10 September 2004, published by World Scientific, Singapore 2005, p. 494

[Bau05] M. Bauer, L. Pandola and C. Tomei: "Muon background evaluation for Gerda", GERDA Scientific / Technical Report GSTR-05-003

[Bau06] M. Bauer *et al.*: "Simulation of shielding designs for future large-scale dark matter search experiments", Proceedings of the Sixth International Workshop on the Identification of Dark Matter, Rhodes, Greece, 11–16 September 2006, published by World Scientific, Singapore 2007, p. 526

[Beg91] K. G. Begeman, A. H. Broeils and R. H. Sanders: "Extended rotation curves of spiral galaxies: dark haloes and modified dynamics", MNRAS 249 (1991) 523

[Ber89] Ch. Berger *et al.*: "Experimental study of muon bundles observed in the Fréjus detector", Phys Rev D 40 (1989) 2163

[Ber99] Lars Bergström and Ariel Goobar: Cosmology and Particle Astrophysics, Wiley/Praxis, Chichester 1999

[Ber05] Gianfranco Bertone, Dan Hooper, Joseph Silk: "Particle dark matter: evidence, candidates and constraints", Physics Reports 405 (2005) 279, arXiv:hep-ph/0404175

[Ber08] R. Bernabei *et al.*: "First results from DAMA/LIBRA and the combined results with DAMA/NaI", Eur. Phys. J. C 56 (2008) 333, arXiv:0804.2741 [astro-ph]

[Ber10] R. Bernabei *et al.*: "New results from DAMA/LIBRA", Eur. Phys. J. C 67 (2010) 39, arXiv:1002.1028v1 [astro-ph.GA]

[Bet30] H. Bethe: "Zur Theorie des Durchgangs schneller Korpuskularstrahlen durch Materie", Annalen der Physik 397 (1930) 325

[Bet34] Hans Bethe and Walter Heitler: "On the Stopping of Fast Particles and on the Creation of Positive Electrons", Proceedings of the Royal Society of London, Series A Volume 146, Issue 856 (1934) 83

[Bol99] A. I. Bolozdynya: "Two-phase emission detectors and their applications", NIM A 422 (1999) 314

[Bor75] V. V. Borog and A. A. Petrushkin, Proc. 14th Int. Conf. on Cosmic Rays, Munich 1975, vol. 6, p. 1949

[Bör03] G. Börner: "The Early Universe", Fourth Edition, Springer Verlag Berlin Heidelberg 2003

[Bra08] M. Bradač *et al.*: "Revealing the properties of dark matter in the merging cluster MACS J0025.4-1222", ApJ 687 (2008) 959, arXiv:0806.2320 [astro-ph]; Chandra image: http://chandra.harvard.edu/photo/2008/macs/ ; STScI-2008-32 press release: http://hubblesite.org/newscenter/archive/releases/2008/32/

[Bri97] J. F. Briesmeister, Ed., "MCNP—A General Monte Carlo N-Particle Code, Version 4B", LA-12625-M, Los Alamos National Laboratory (March 1997)

[Bro72] S. J. Brodsky, F. E. Close, J. F. Gunion: "Phenomenology of Photon Processes, Vector Dominance, and Crucial Tests for Parton Models", Phys. Rev. D6 (1972) 177

[Bro07] J. R. Brownstein and J. W. Moffat: "The Bullet Cluster 1E0657-558 evidence shows Modified Gravity in the absence of Dark Matter", MNRAS 382 (2007) 29, arXiv:astro-ph/0702146

[Buc01] C. Bucci *et al.*: "Update of the Proposal to the LNGS for a Second Phase of the CRESST Dark Matter Search", MPI-PhE/2001-02, http://www.cresst.de/files/200102.pdf

[Cal79] D. O. Caldwell *et al.*.: "Measurement of Shadowing in Photon-Nucleus Total Cross Sections from 20 to 185 GeV", Phys. Rev. Lett. 42 (1979) 553

[Cat86] P. G. Catalano *et al.*: "Analisi strutturale nei laboratori dell'I.N.F.N. del Gran Sasso d'Italia", Mem. Soc. Geol. It. 35 (1986) 647

[Cha04] L. Chabert: “Étude du bruit de fond neutron induit par les muons dans l’expérience EDELWEISS-II”, PhD thesis, Université Claude Bernard – Lyon 1, 2004

[CHA06] CHANDRA X-Ray Observatory: “NASA finds direct proof of Dark Matter”, http://chandra.harvard.edu/photo/2006/1e0657/, image credits: X-ray: NASA/CXC/CfA/M.Markevitch *et al.*.; Optical: NASA/STScI; Magellan/U.Arizona/D.Clowe *et al.*.; Lensing Map: NASA/STScI; ESO WFI; Magellan/U.Arizona/D.Clowe *et al.*.

[Cha08] Yuen-Dat Chan *et al.*: “MaGe—A Geant4-based Monte Carlo framework for low-background experiments”, arXiv:0802.0860 [nucl-ex]

[Cha09] Astrid Chantelauze: “Investigation of the muon-induced background of the EDELWEISS-II experiment”, PhD thesis, Université Blaise Pascal Clermont-Ferrand, 2009

[Chw24] Orest Chwolson: “Über eine mögliche Form fiktiver Doppelsterne”, Astron. Nachrichten 221 (1924) 329

[Clo06] D. Clowe *et al.*: “A Direct Empirical Proof of the Existence of Dark Matter”, ApJ 648 (2006) L109, arXiv:astro-ph/0608407

[Dem99] A. Dementyev *et al.*: “Production and transport of hadrons generated in nuclear cascades initiated by muons in the rock (exclusive approach)”, Nucl. Phys. B (Proc. Suppl.) 70 (1999) 486

[Ein36] Albert Einstein: “Lens-like action of a star by the deviation of light in the gravitational field”, Science 84 (1936) 506

[EUR12] The EURECA collaboration: “EURECA Conceptual Design Report”, to be published

[Fas00] A. Fasso, A. Ferrari and P. R. Sala, in Proceedings of the Monte Carlo 2000 Conference, (Lisbon, October 23–26, 2000), eds. A. King, F. Barao, M. Nakagawa, L. Tavora, P. Vaz, Springer Verlag, Berlin 2001

[Fer05] A. Ferrari *et al.*: “FLUKA: a multi-particle transport code”, SLAC-R-773 / CERN-2005-010 / INFN TC_05/11, October 2005, http://www.slac.stanford.edu/pubs/slacreports/slac-r-773.html

[Fes85] H. Fesefeldt: “The Simulation of Hadronic Showers—Physics and Applications”, Technical Report RWTH Aachen PITHA 85/02; http://cdsweb.cern.ch/record/162911/files/CM-P00055931.pdf

[Fix96] D. J. Fixsen *et al.*: “The cosmic microwave background spectrum from the full COBE FIRAS data set”, ApJ 473 (1996) 576, arXiv:astro-ph/9605054

[For94] B. Fort and Y. Mellier: “Arc(let)s in clusters of galaxies”, Astron Astrophys Rev 5 (1994) 239

[Fri08] Joshua A. Frieman, Michael S. Turner and Dragan Huterer: "Dark Energy and the Accelerating Universe", Ann. Rev. Astron. Astrophys. 46 (2008) 385, arXiv:0803.0982 [astro-ph]

[Gai90] Thomas K. Gaisser: "Cosmic Rays and Particle Physics", Cambridge University Press 1990

[Gai10] R. Gaitskell and J. Filippini: "SUSY Dark Matter/Interactive Direct Detection Limit Plotter", http://dmtools.berkeley.edu/limitplots/

[Gai12] R. Gaitskell, V. Mandic, J. Filippini, D. Speller: "Direct Detection of WIMP Dark Matter, Sensitivity Plots", http://cedar.berkeley.edu/plotter/ Plots generated on 2012-06-16.

[Geant3] GEANT Detector Description and Simulation Tool, CERN Program Library Long Writeup W5013, http://wwwinfo.cern.ch/asdoc/pdfdir/geant.pdf

[Geant4] S. Agostinelli *et al.*: "Geant4—a simulation toolkit", NIM A 506 (2003) 250; J. Allison *et al.*: "Geant4 developments and applications", IEEE Transactions on Nuclear Science 53 No. 1 (2006) 270; Homepage: http://geant4.web.cern.ch/geant4/

[Ger11] G. Gerbier: "EURECA: Dark Matter search with 1t of cryogenic detectors", talk at TAUP 2011, Munich, http://taup2011.mpp.mpg.de/php/downloadPresentationFile.php?type=presentation&sessionid=28&presentationid=188, proceedings to be published in JPCS

[G4PRM] Geant4 Physics Reference Manual, version: Geant4 9.1 (14 December, 2007), http://geant4.web.cern.ch/geant4/UserDocumentation/UsersGuides/PhysicsReferenceManual/fo/PhysicsReferenceManual.pdf (04.11.2008)

[G4UAD] Geant4 User's Guide for Application Developers, version: Geant4 9.1 (14 December, 2007), http://geant4.web.cern.ch/geant4/UserDocumentation/UsersGuides/ForApplicationDeveloper/fo/BookForAppliDev.pdf (04.11.2008)

[G482] Geant4 8.2 Release Notes, December 15th, 2006, http://geant4.web.cern.ch/geant4/support/ReleaseNotes4.8.2.html

[Gon05] P. Gondolo: "How can we make sure we detect dark matter?", arXiv:hep-ph/0501134

[Gra96] David S. Graff and Katherine Freese: "Analysis of a Hubble Space Telescope search for red dwarfs: Limits on baryonic matter in the galactic halo", ApJ 456 (1996) L49, arXiv:astro-ph/9507097

[Gre66] Kenneth Greisen: "End to the Cosmic Ray Spectrum?", Phys. Rev. Lett. 16 (1966) 748

[Gro01] Donald E. Groom *et al.*: "Muon Stopping Power and Range Tables 10 MeV–100 TeV", Atomic Data and Nuclear Data Tables 78 (2001) 183

[Gud83] K. K. Gudima *et al.*: "Cascade-Exciton Model of Nuclear Reactions", Nucl. Phys. A 401 (1983) 329

[Han63] L. N. Hand: "Experimental Investigation of Pion Electroproduction", Phys. Rev. 129 (1963) 1834

[Hes12] Viktor F. Hess: "Über Beobachtungen der durchdringenden Strahlung bei sieben Freiballonfahrten", Physik. Zeitschr. 13 (1912) 1084; "Über den Ursprung der durchdringenden Strahlung", Physik. Zeitschr. 14 (1913) 610

[Hin09] G. Hinshaw *et al.*: "Five-Year Wilkinson Microwave Anisotropy Probe Observations: Data Processing, Sky Maps, and Basic Results", ApJ Suppl 180 (2009) 225

[Hoo10] D. Hooper *et al.*: "A Consistent Dark Matter Interpretation For CoGeNT and DAMA/LIBRA", Phys. Rev. D 82 (2010) 123509, arXiv:1007.1005v3 [hep-ph]

[Hor07] M. Horn: "Simulations of the muon-induced neutron background of the EDELWEISS-II experiment for Dark Matter search", PhD thesis, Universität Karlsruhe (TH) 2007

[HST95] Hubble Space Telescope News Release STSci-1995-14: "Hubble Views Distant Galaxies through a Cosmic Lens", http://hubblesite.org/newscenter/archive/releases/1995/14/
Image credit: W. Couch (University of New South Wales), R. Ellis (Cambridge University), and NASA

[Hub29] Edwin Hubble: "A relation between distance and radial velocity among extra-galactic nebulae", Proc. N. A. S. 15 (1929) 168

[ICRU49] ICRU Report No. 49: "Stopping Power and Ranges for Protons and Alpha Particles", 1993

[Irw05] K. D. Irwin and G. C. Hilton: "Transition Edge Sensors", Topics Appl. Phys. 99 (2005) 63 (C. Enss (Ed.): Cryogenic Particle Detection), http://qdev.boulder.nist.gov/817.03/pubs/downloads/qsensors/TESIrwinHilton.pdf

[Jar11] N. Jarosik *et al.*: "Seven-Year Wilkinson Microwave Anisotropy Probe (WMAP) Observations: Sky Maps, Systematic Errors, and Basic Results", ApJ Suppl 192 (2011) 14, arXiv:1001.4744 [astro-ph.CO]

[JAS3] JAS3, a general purpose, open-source, data analysis tool, http://jas.freehep.org/jas3/

[Kel95] S. R. Kelner, R. P. Kokoulin, A. A. Petrukhin: "About cross section for high-energy muon bremsstrahlung", Preprint MEPhI 024-95, Moscow 1995, CERN SCAN-9510048

[Kla95] H. V. Klapdor-Kleingrothaus, A. Staudt: "Teilchenphysik ohne Beschleuniger", B. G. Teubner Stuttgart 1995

[Kla97] H. V. Klapdor-Kleingrothaus, K. Zuber: "Teilchenastrophysik", B. G. Teubner Stuttgart 1997

[Kno03] R. A. Knop *et al.* (The Supernova Cosmology Project): "New Constraints on Ω_M, Ω_Λ and w from an Independent Set of 11 High-Redshift Supernovae Observed With The Hubble Space Telescope", ApJ 598 (2003) 102, arXiv:astro-ph/0309368. The actual image is taken from http://supernova.lbl.gov/PDFs/SCP2003SNeCMBClust.pdf and modified to include the separation line between accelerating and delecerating Universes shown in http://supernova.lbl.gov/PDFs/SCP2003OmegaConfTrans.pdf

[Kom09] E. Komatsu *et al.*: "Five-Year Wilkinson Microwave Anisotropy Probe Observations: Cosmological Interpretation", ApJ Suppl 180 (2009) 330, arXiv:0803.0547 [astro-ph]

[Kom11] E. Komatsu *et al.*: "Seven-Year Wilkinson Microwave Anisotropy Probe (WMAP) Observations: Cosmological Interpretation", ApJ Suppl 192 (2011) 18, arXiv:astro-ph/1001.4538 [astro-ph.CO]

[Kra03] Ch. Kraus: "Messungen und Gesamtanalyse zur Neutrinomasse am Mainzer Tritium-β-Experiment", Dissertation, Johannes Gutenberg Universität Mainz 2003

[Kra08] H. Kraus *et al.*: "EURECA—The Future of Cryogenic Dark Matter Detection in Europe", Proceedings of the IDM 2008, Stockholm, Sweden, August 18–22, PoS(idm2008)013, http://pos.sissa.it/archive/conferences/064/013/idm2008_013.pdf

[Krö05] Kevin Kröninger, Xiang Liu, Luciano Pandola, Claudia Tomei: "Using MaGe for the Simulation of the GERDA Experiment", GERDA Scientific / Technical Report GSTR-05-002

[LAM08] Legacy Archive for Microwave Background Data Analysis (LAMBDA) (NASA / WMAP Science Team), http://lambda.gsfc.nasa.gov/ We acknowledge the use of the Legacy Archive for Microwave Background Data Analysis (LAMBDA). Support for LAMBDA is provided by the NASA Office of Space Science.

[Lar11] D. Larson *et al.*: "Seven-Year Wilkinson Microwave Anisotropy Probe (WMAP) Observations: Power-spectra and WMAP-derived Parameters", ApJ Suppl 192 (2011) 16, arXiv:1001.4635 [astro-ph.CO]

[Lew03] Aaron D. Lewis, David A. Buote, and John T. Stocke: "*Chandra* observations of A2029: The dark matter profile down to below $0.01 r_{\text{vir}}$ in an unusually relaxed cluster", ApJ 586 (2003) 135

[Lip91] P. Lipari and T. Stanev: "Propagation of multi-TeV muons", Phys. Rev. D 44 (1991) 3543

[Lob02] V. M. Lobashev: "Study of the Tritium Beta-spectrum in Experiment "Troitsk ν-mass"", Prog. Part. Nucl. Phys. 48 (2002) 123

[Loh85] W. Lohmann, R. Kopp and R. Voss: "Energy loss of muons in the energy range 1–10000 GeV", CERN Yellow Report 85-03 (21 March 1985), http://doc.cern.ch/yellowrep/1985/1985-003/p1.pdf

[Lom07] Lombardi SA: "New Halls for Underground Laboratory—Preliminary Study for Laboratory Enlargement", Technical Report 6145.1-R-01-A, Minusio, http://www-extension-lsm.in2p3.fr/images/6145.1-R-01A%20English%20version.pdf (English version, March 2007), http://www-extension-lsm.in2p3.fr/images/6145.1-R-01A.pdf (French version, January 2007)

[LSMHP] LSM Homepage: http://www-lsm.in2p3.fr/index.html

[Mar93] Humphrey J. Maris and Shin-ichiro Tamura: "Anharmonic decay and the propagation of phonons in an isotropically pure crystal at low temperatures: Application to dark-matter detection", Phys. Rev. B 47 (1993) 727

[Mar97] Stephen P. Martin: "A Supersymmetry Primer", arXiv:hep-ph/9709356

[Mar04] O. Martineau *et al.* (EDELWEISS Collaboration): "Calibration of the EDELWEISS Cryogenic Heat-and-ionisation Germanium Detectors for Dark Matter Search", NIM A 530 (2004) 426, arXiv:astro-ph/0310657

[Mei06] D.-M. Mei and A. Hime: "Muon-Induced Background Study for Underground Laboratories", Phys. Rev. D 73 (2006) 053004, arXiv:astro-ph/0512125

[Meu99] P. Meunier *et al.*: "Discrimination between nuclear recoils and electron recoils by simultaneous detection of phonons and scintillation light", Appl. Phys. Lett. 75 (1999) 1335

[Mil83] M. Milgrom: "A modification of the Newtonian dynamics as a possible alternative to the hidden mass hypothesis", ApJ 270 (1983) 365

[Oli03] K. A. Olive: "TASI Lectures on Dark Matter", arXiv:astro-ph/0301505

[OPS] OpenScientist, http://openscientist.lal.in2p3.fr/

[PDG08] C. Amsler *et al.*: "Review of Particle Physics", Physics Letters B 667, 1 (2008)

[PDG10] K. Nakamura *et al.* (Particle Data Group): "Review of Particle Physics", J. Phys. G 37, 075021 (2010) and 2011 partial update for the 2012 edition.

[Pea01] John A. Peacock: "Cosmological Physics", Cambridge University Press, Cambridge 2001

[Pen65] A. A. Penzias and R. W. Wilson: "A measurement of excess antenna temperature at 4080 Mc/s", ApJ 142 (1965) 419

[Per92] Massimo Persic and Paolo Salucci: "The baryon content of the Universe", Mon. Not. R. Astr. Soc. 258 (1992) 14P (Short Communications)

[Per99] S. Perlmutter *et al.* (The Supernova Cosmology Project): "Measurements of Ω and Λ from 42 high-redshift supernovae", ApJ 517 (1999) 565, arXiv:astro-ph/9812133

[Per03] Donald Perkins: “Particle Astrophysics”, Oxford University Press, Oxford 2003

[Pov99] Povh, Rith, Scholz, Zetsche: “Teilchen und Kerne”, 5. Auflage, Springer, Berlin Heidelberg 1999

[Rho93] W. Rhode: “Study of Ultra High Energy Muons with the Frejus Detector” (in German), PhD thesis, Bergische Universität Wuppertal 1993

[Rie98] Adam G. Riess *et al.*: “Observational Evidence from Supernovae for an Accelerating Universe and a Cosmological Constant”, Astr. J. 116 (1998) 1009, arXiv:astro-ph/9805201

[ROOT] ROOT: An Object-Oriented Data Analysis Framework, http://root.cern.ch/

[RPL08] Reference Physics Lists, http://geant4.web.cern.ch/geant4/support/proc_mod_catalog/physics_lists/referencePL.shtml, 4.11.2008

[Rub80] Vera C. Rubin, W. Kent Ford, Jr., and Norbert Thonnard: “Rotational properties of 21 Sc galaxies with a large range of luminosities and radii, from NGC 4605 ($R = 4\,\mathrm{kpc}$) to UGC 2885 ($R = 122\,\mathrm{kpc}$)”, ApJ 238 (1980) 471

[Sah04] Varun Sahni: “Dark Matter and Dark Energy”, Lect. Notes Phys. 653 (2004) 141, arXiv:astro-ph/0403324v3

[San05] V. Sanglard *et al.* (EDELWEISS Collaboration): “Final results of the EDELWEISS-I dark matter search with cryogenic heat-and-ionization Ge detectors”, Phys. Rev. D 71 (2005) 122002, arXiv:astro-ph/0503265

[Sch95] Sabine Schindler: “The Accuracy of Mass Determination in Galaxy Clusters by X-Ray Observations”, MPE Preprint 311, arXiv:astro-ph/9503040

[Sch11] Stephan Scholl: “Neutron background simulation for the CRESST-II experiment”, PhD thesis, Eberhard Karls Universität Tübingen 2011

[Ser47] R. Serber: “Nuclear Reactions at High Energies”, Phys. Rev. 72 (1947) 1114

[SK03] The Super-Kamiokande Collaboration: “The Super-Kamiokande Detector”, NIM A 501 (2003) 418, http://www-sk.icrr.u-tokyo.ac.jp/sk/pub/sknimpaper.pdf

[Smo09] Smoot Cosmology Group: “Geometry of the Universe / Curvature of Space-Time”, http://aether.lbl.gov/universe_shape.html

[Sok10] P. Sokolsky for the HiRes Collaboration: “Final Results from the High Resolution Fly’s Eye (HiRes) Experiment”, XVI International Symposium on Very High Energy Cosmic Ray Interactions, Batavia, IL, USA, 28 June - 2 July 2010, arXiv:1010.2690 [astro-ph.HE]

[Ste71] R. M. Sternheimer and R. F. Peierls: “General Expression for the Density Effect for the Ionization Loss of Charged Particles”, Phys. Rev. B 3 (1971) 3681

[Ste09] Frank Daniel Steffen: “Dark Matter Candidates: Axions, Neutralinos, Gravitons, and Axinos”, Eur. Phys. J. C 59 (2009) 557, arXiv:0811.3347 [hep-ph]

[Str97] Bjarne Stroustrup: “The C++ Programming Language”, Third Edition, Addison Wesley Longman, Reading MA (USA) 1997

[Tak03] M. Takeda *et al.*: “Energy determination in the Akeno Giant Air Shower Array Experiment”, Astropart. Phys. 19 (2003) 447, arXiv:astro-ph/0209422

[Tis07] P. Tisserand *et al.* (The EROS-2 collaboration): “Limits on the Macho content of the Galactic Halo from the EROS-2 Survey of the Magellanic Clouds”, Astronomy&Astrophysics 469 (2007) 387, arXiv:astro-ph/0607207

[Tit99] Yu. E. Titarenko *et al.*: “Experimental and Computer Simulation Study of Radionuclide Production in Heavy Materials Irradiated by Intermediate Energy Protons”, LANL Report LA-UR-99-4489 (1999), arXiv:nucl-ex/9908012

[Tom09] V. Tomasello: “Background Simulations for a Large-scale Cryogenic Dark Matter Experiment”, PhD thesis, University of Sheffield 2009

[T2NIS] T-2 Nuclear Information Service (Los Alamos), http://t2.lanl.gov/

[Vul98] B. Vulpescu *et al.*: “A compact detector for the measurement of the cosmic ray muon charge ratio”, Forschungszentrum Karlsruhe Bericht FZKA 6071 (1998), NIM A 414 (1998) 205

[Wal79] D. Walsh, R. F. Carswell, R. J. Weymann: “0957+561 A, B: twin quasistellar objects or gravitational lens?”, Nature 279 (1979) 381

[Wei93] Y. Wei: “The neutrino induced muon flux at the Frejus underground experiment”, PhD thesis, Bergische Universität Wuppertal, 1993

[Wei08] Steven Weinberg: “Cosmology”, Oxford University Press, Oxford 2008

[Wel01] H.-P. Wellisch, comment to Geant4 problem report #268 “Problem with energy conservation in the HP capture model”, http://bugzilla-geant4.kek.jp/show_bug.cgi?id=268#c1 (downloaded on 2012-07-07)

[Wel04a] H.-P. Wellisch: “Educated Guess Physics Lists for use cases involving hadronic Physics”, http://geant4.web.cern.ch/geant4/physics_lists/

[Wel04b] H.-P. Wellisch, private communication

[Whi93] Simon D. M. White *et al.*: “The baryon content of galaxy clusters: a challenge to cosmological orthodoxy”, Nature 366 (1993) 429

[Whi97] Martin White and Wayne Hu: “The Sachs-Wolfe effect”, Astron. Astrophys. 321 (1997) 8, arXiv:astro-ph/9609105

[Wit04] J. W. Wittwer: “Monte Carlo Simulation Basics” from vertex42.com, June 1, 2004, http://www.vertex42.com/ExcelArticles/mc/MonteCarloSimulation.html

[WMAP10] WMAP Universe 101: “Is the Universe Infinite?”, http://map.gsfc.nasa.gov/universe/uni_shape.html; deep links: http://map.gsfc.nasa.gov/media/990006/index.html and http://map.gsfc.nasa.gov/media/990006/990006_2048.jpg

[Wol96] TA Joy Woller: "The Basics of Monte Carlo Simulations", University of Nebraska-Lincoln, Physical Chemistry Lab (Chem 484), Spring 1996, http://www.chem.unl.edu/zeng/joy/mclab/mcintro.html

[Wri07] D. Wright: "Cuts, Decay and Optical Physics", SLAC Geant4 Tutorial, 16 May 2007, http://geant4.slac.stanford.edu/SLACTutorial07/CutsDecayOptical.pdf

[Wul03] Hesti R. T. Wulandari: "Study On Neutron-Induced Background in the Dark Matter Experiment CRESST", PhD thesis, Technische Universität München 2003

[Wul04a] H. Wulandari *et al.*: "Neutron flux at the Gran Sasso underground laboratory revisited", Astropart. Phys. 22 (2004) 313, arXiv:hep-ex/0312050

[Wul04b] H. Wulandari *et al.*: "Neutron Background Studies for the CRESST Dark Matter Experiment", arXiv:hep-ex/0401032

[Wul04c] H. Wulandari, private communication

[Yam03] M. Yamashita *et al.*: "Double phase (liquid/gas) xenon scintillation detector for WIMPs direct search", Astropart. Phys. 20 (2003) 79

[Yük09] Hasan Yüksel, Matthew D. Kistler, and Todor Stanev: "TeV Gamma Rays from Geminga and the Origin of the GeV Positron Excess", Phys. Rev. Lett. 103 (2009) 051101, arXiv:0810.2784 [astro-ph]

[Zat66] G. T. Zatsepin and V. A. Kuz'min, "Upper limit of the spectrum of cosmic rays", JETPL 4 (1966) 78

[Zwi33] F. Zwicky: "Die Rotverschiebung von extragalaktischen Nebeln", Helv. Phys. Act. 6 (1933) 110

[Zwi37] F. Zwicky: "On the masses of nebulae and of clusters of nebulae", ApJ 86 (1937) 217

Acknowledgements

First of all I would like to thank my thesis supervisor, Prof. Dr. Josef Jochum, for giving me the opportunity to work on such an interesting topic, for many physics discussions and for his excellent mentoring of this thesis. I also thank the other professors of our research group, my second reviewer Prof. Dr. Heinz Clement, Prof. Dr. Peter Grabmayr and Prof. Dr. Tobias Lachenmaier, for many interesting discussions.

This work has profited greatly from discussions with a number of people from different collaborations and institutions. I would like to thank Dr. Hesti Wulandari for her FLUKA results and our comparison between GEANT4 and FLUKA; Dr. Markus Horn for his Frejus muon generator and many discussions on GEANT4 in general and physics lists in particular; Dr. Luciano Pandola for the Gran Sasso muon generator; and Dr. Vitaly Kudryavtsev for interesting discussions on background simulations.

I would like to thank my office mates: Dr. Stephan Scholl—we had many interesting discussions on physics as well as on politics; Dr. Markus Knapp—we worked together on the GERDA experiment in the beginning of my thesis; Daniel Greiner—for his expertise in ROOT and programming in general; and Markus Röhling—for keeping me up to date on the progress of DoubleChooz.

The computers and network are in good shape due to the excellent work of our system administrators, Dr. Arthur Erhardt, Dr. Marcel Kimmerle and PD Dr. Roland Speith—many thanks for that!

I thank Sabine Schulze, Sonja Hierlemann, Gaby Behring, Brunhilde Eiskant, Anja Walz and Dr. Günter Lang for taking care of the administration.

I would like to thank all members of our astroparticle physics group for the pleasant and inspiring working atmosphere: Gerhard Deuter, Sebastian Diebold, Dennis Dietrich, Raphael Falkenstein, Kai Freund, Andrea Hagen, Alexander Hegai, Dr. Thomas Jagemann, Dr. Georg Meierhofer, Dr. Ludwig Niedermeier, Claudia Osswald, Marc Pfeifer, Dr. Florian Ritter, Klemens Rottler, Christof Sailer, Christopher Schmitt, Christian Strandhagen, Katharina von Sturm, Dr. Vito Tomasello, Igor Usherov-Marshak, all the people I may have forgotten as well as all the people new to the group who keep up the good work on science.

My special thanks go to Petra Vergien for our long-time good friendship—and for proofreading this thesis.

Finally I would like to thank my parents for supporting me during my physics studies which formed the basis of all of this work.